Mapping global land-cover dynamics using time-series Landsat stacks

Prof. Liangyun Liu

Aerospace Information Research Institute, Chinese Academy of Sciences

liuly@radi.ac.cn

Contents

1. Introduction

Land-cover data are important and necessary for supporting **sustainable development goals**, maintaining biodiversity, and monitoring natural resources.

Fine-resolution land-cover monitoring at the regional or global scale is regarded as an important scientific goal, while it is usually time-consuming and involves a lot of manual participation.

1. Introduction

Over past decades, the quickly development of remote sensing techniques as well as storage and computation capabilities, the **global land-cover mapping makes great progresses**, a series of global land-cover products have been continuously released ranging from 1km~10m. The **overall development trend** is from **low resolution to high resolution** and from **single-epoch land-cover mapping to time-series land-cover change monitoring**.

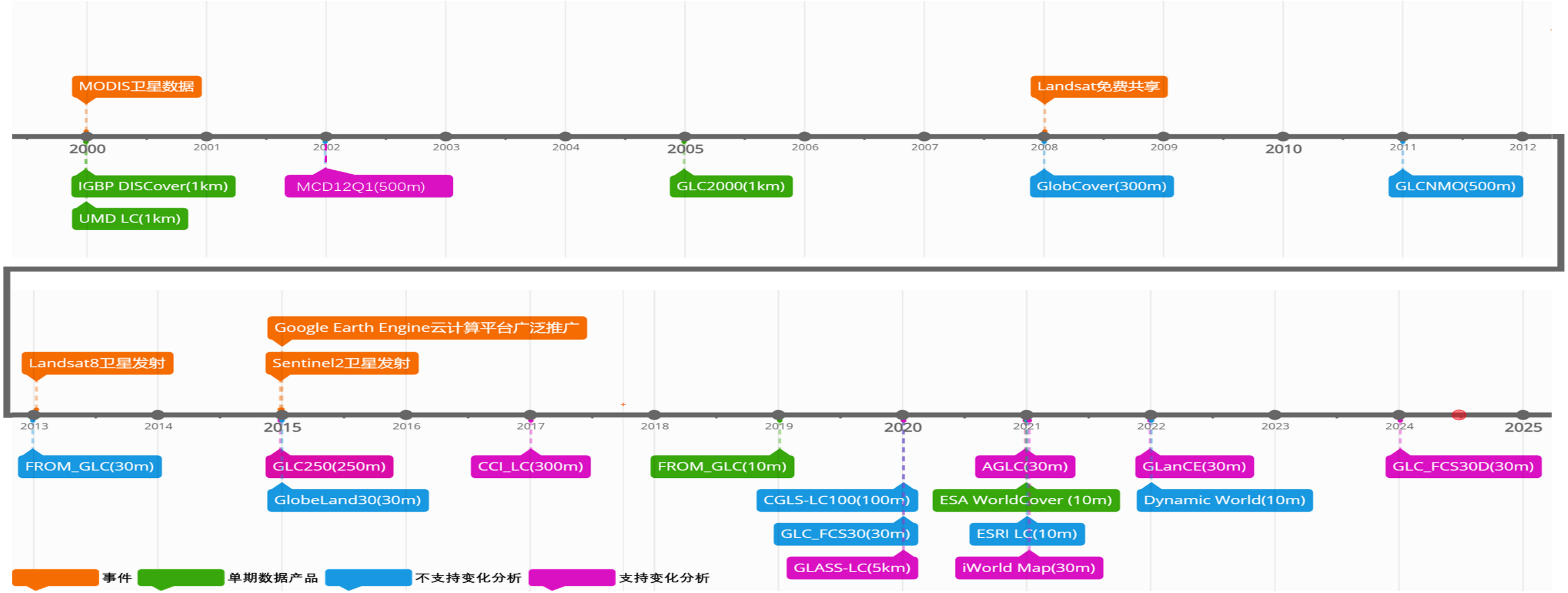

1. Introduction

There is huge uncertainty in the understanding of global land cover changes.

There are great differences between different monitoring datasets. Winkler et al. quantitatively calculated the global annual total land use change area ranging from 0.249×10^6 km^2 (ESA CCI product) to 1.123×10^6 km^2 (NASA MCD12Q1 product).

Table 1 Comparison of land use/cover datasets.

Dataset	LUC categories included	Compared time period	Annual gross land use change (mean ± standard deviation in 103 km^2 a^{-1})	
				HILDA +
LUH2[14]	All	1960-2015	302 ± 125	721 ± 88
HYDE3.2[13] cropland	Cropland (2)	1960-2015	187 ± 82	246 ± 41
HYDE3.2[13] pasture	Pasture/rangelands (3)	1960-2015	57 ± 25	420 ± 71
SAGE cropland[15]	Cropland (2)	1960-2011	203 ± 74	253 ± 37
Hansen GFC forest[66]	Forest (4)	2000-2012[a]	265 ± 27	270 ± 21
ESA CCI[67]	All with combined grassland (3 + 5)	1992-2015	249 ± 165	578 ± 40
MODIS[68]	All with combined grassland (3 + 5)	2001-2015	1123 ± 44	574 ± 43

Comparison of annual gross land use/cover (LUC) change (all transitions between included LUC categories or sum of gains and losses for individual LUC categories) of different LUC change datasets with HILDA + for corresponding periods.
[a]Hansen GFC covers forest gain only between 2000 and 2012 (no annual dynamics).

Winkler, K., et al. (2021). **Global land use changes are four times greater than previously estimated**. ***Nature Communications***, *12*, 2501

1. Introduction

There is great uncertainty in the total amount and change of global forest cover.

Chen et al. (2020 RS) quantitatively analyzed the total global forest change area of six products from 2001 to 2012, ranging from a decrease of 1.6×10^6 km^2 (UMD GLAD Forest product) to an increase of 1.7×10^6 km^2 (Vegetation Continuous Fields product).

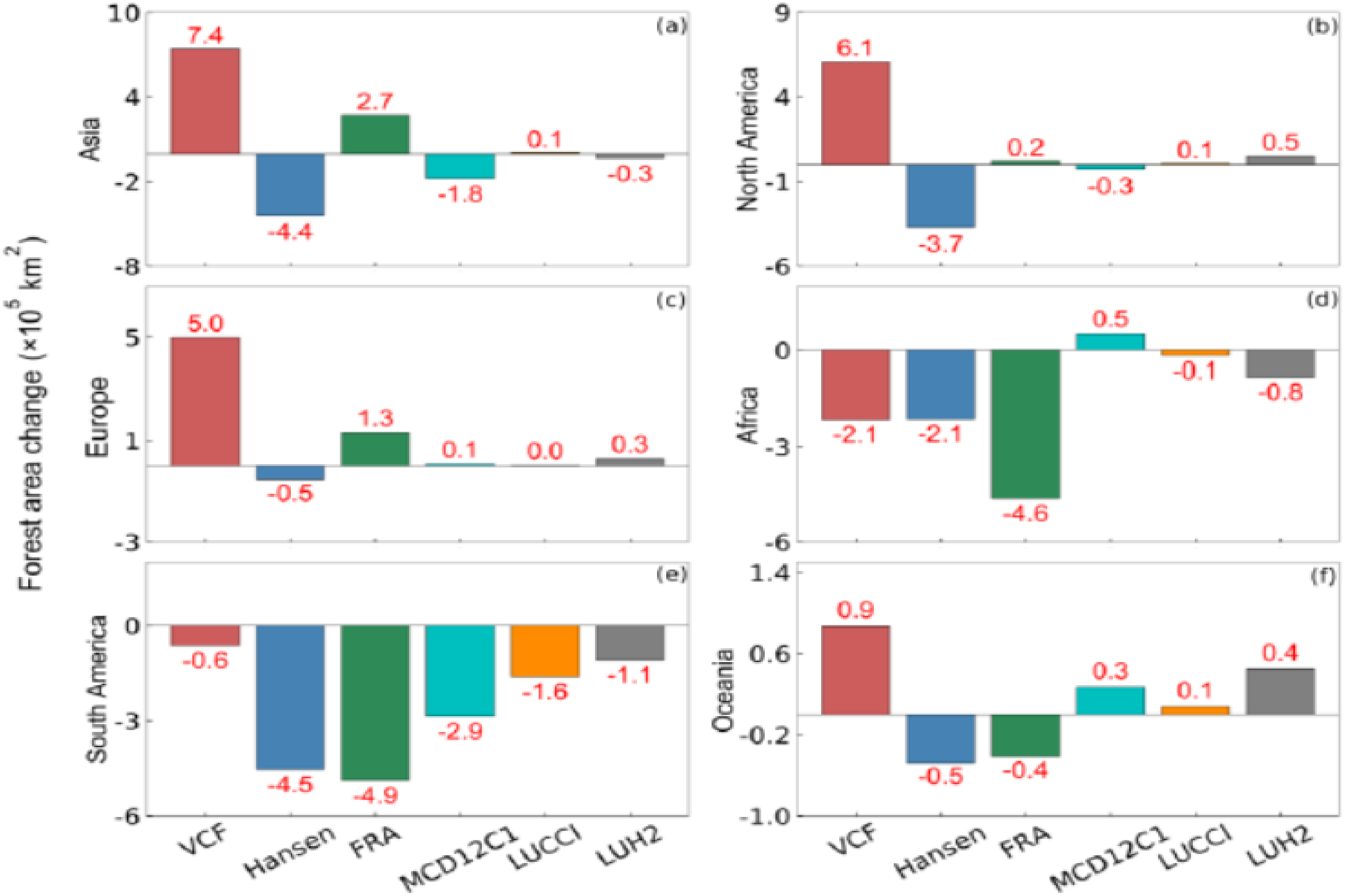

Chen, H., Zeng, Z., Wu, J., et al. (2020). Large uncertainty on forest area change in the early 21st century among widely used global land cover datasets. *Remote Sensing*, *12*(21), 3502.

1. Introduction

- The Landsat series: long-term data record(50years), higher spatial resolution (30-60m), free approach(USGS, CEODE). NASA funded some Landsat reflectance production project: LEDAPS and WELD.
- **Cloud computing platform**, represented by Google Earth Engine, liberates issues such as data collection and pre-processing, and also provides a computing and storage platform.

Challenge: can we reconstruct the history of global land cover from long time-series Landsat stacks?

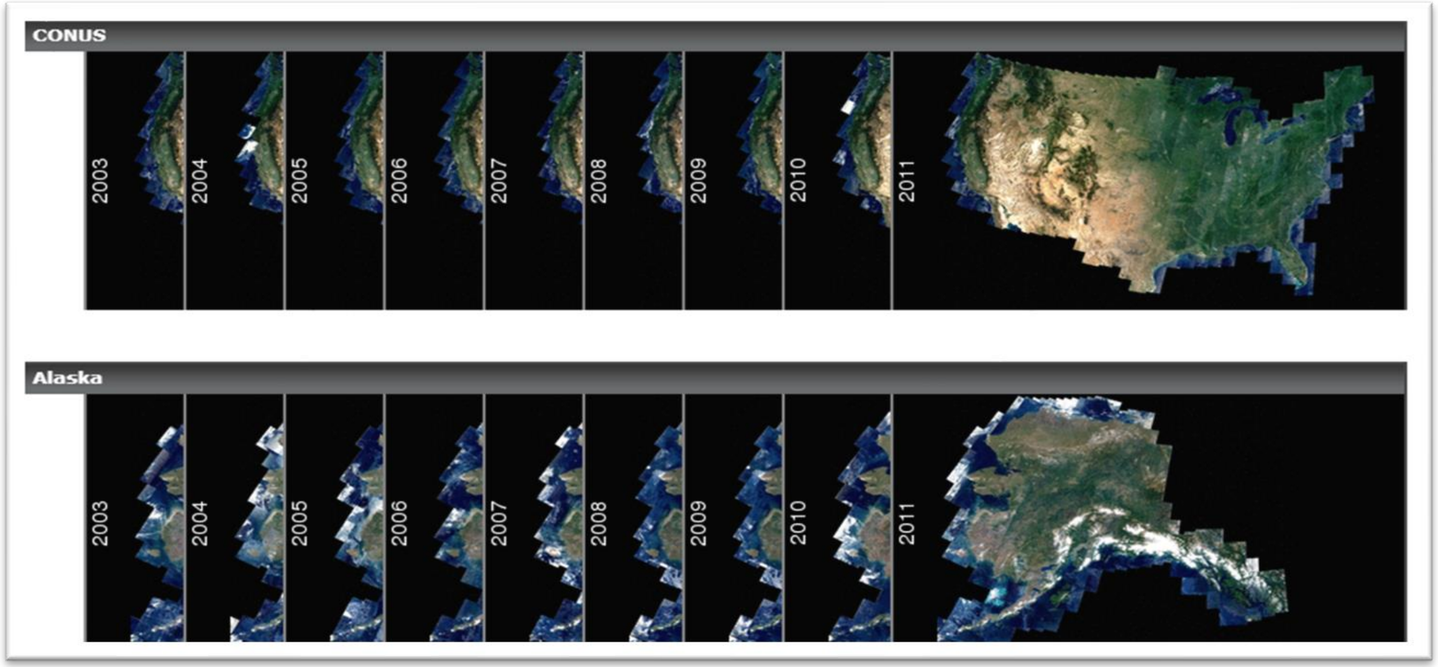

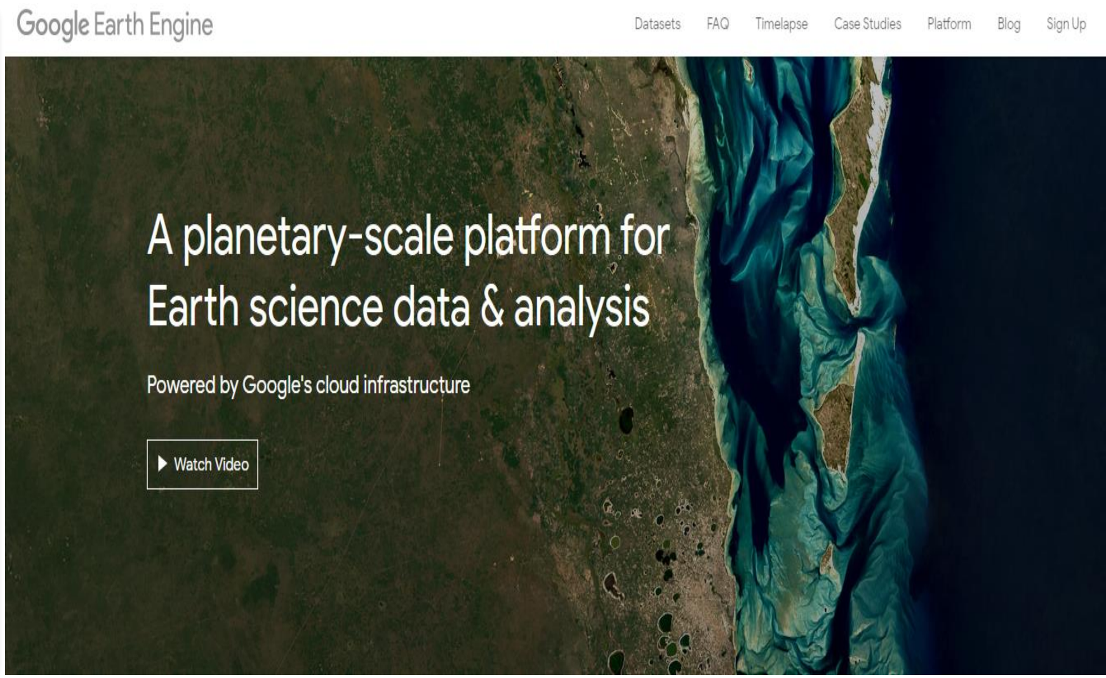

Contents

2. Quantitative pre-processing for Landsat imagery

Background

Surface reflectance is a necessary product for quantitative remote sensing, especially in the long-term or large-area land cover monitoring with multiple remote sensors

Surface reflectance is the basis for developing remote sensing model:
Forest change monitoring,
Water quality monitoring,
Crop growth monitoring…….

Surface reflectance is the basis of surface parameters inversion:
VIS、BRDF/Albedo、
FAPR、GPP/NPP……

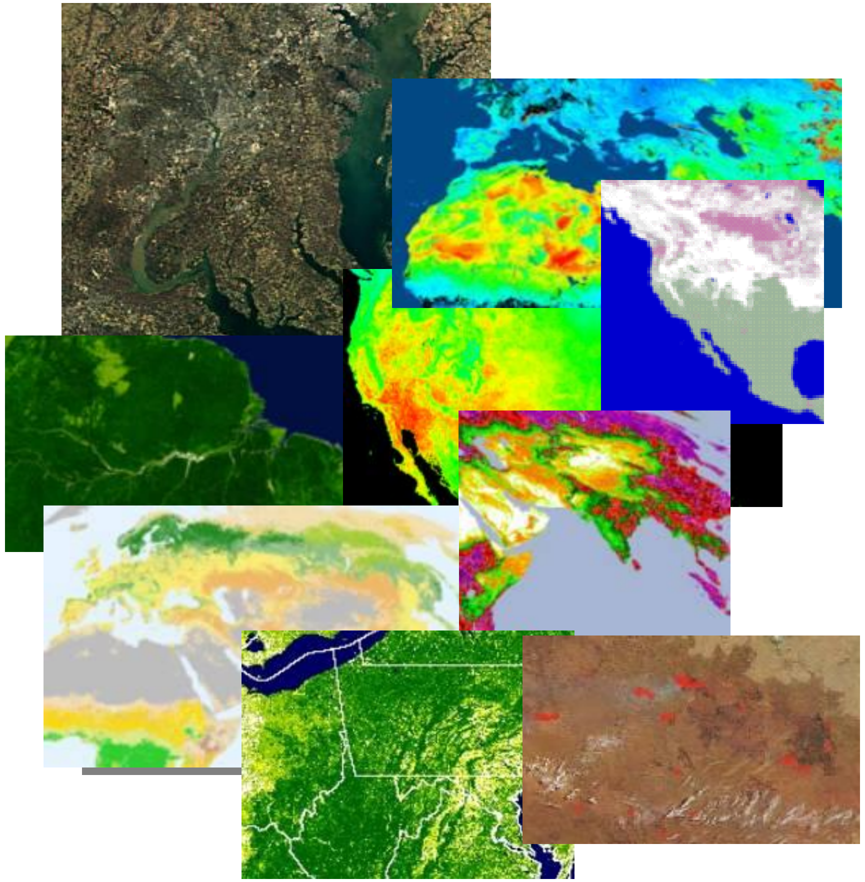

2. Quantitative pre-processing for Landsat imagery

Background

The Landsat series: long-term data record(40years), higher spatial resolution (30-60m), free approach(USGS, CEODE)

NASA funded some Landsat reflectance production project: LEDAPS and WELD

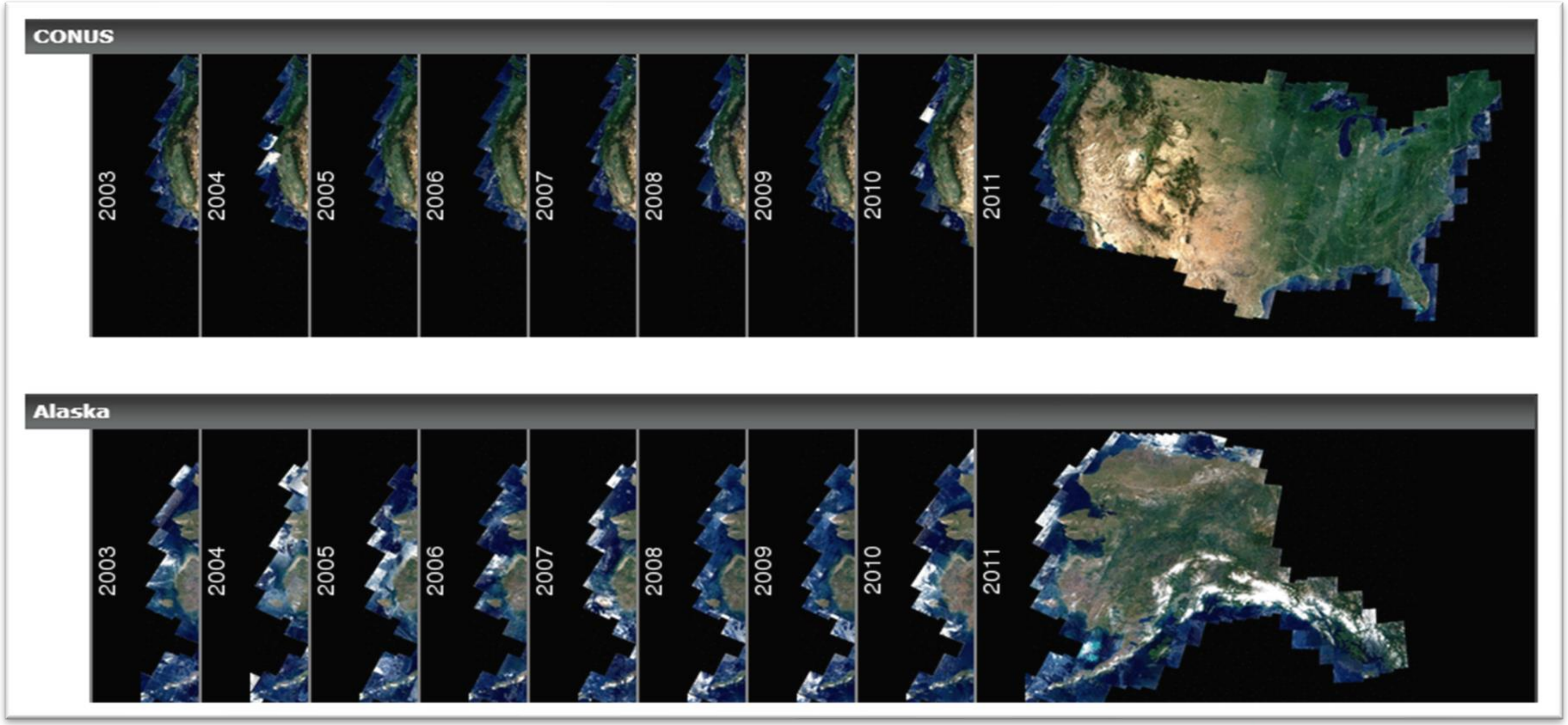

2. Quantitative pre-processing for Landsat imagery

Flowchart of quantitative pre-processing — Flowchart

- Due to the scattering and absorption of atmosphere, the reflectance sensed by the sensors (TOA SR) cannot be equated with the surface reflectance (BOA SR);
- As variances of slope and aspect cause the variation in observed reflectance for similar targets, the SR imagery in terrain areas need to be topographically corrected.

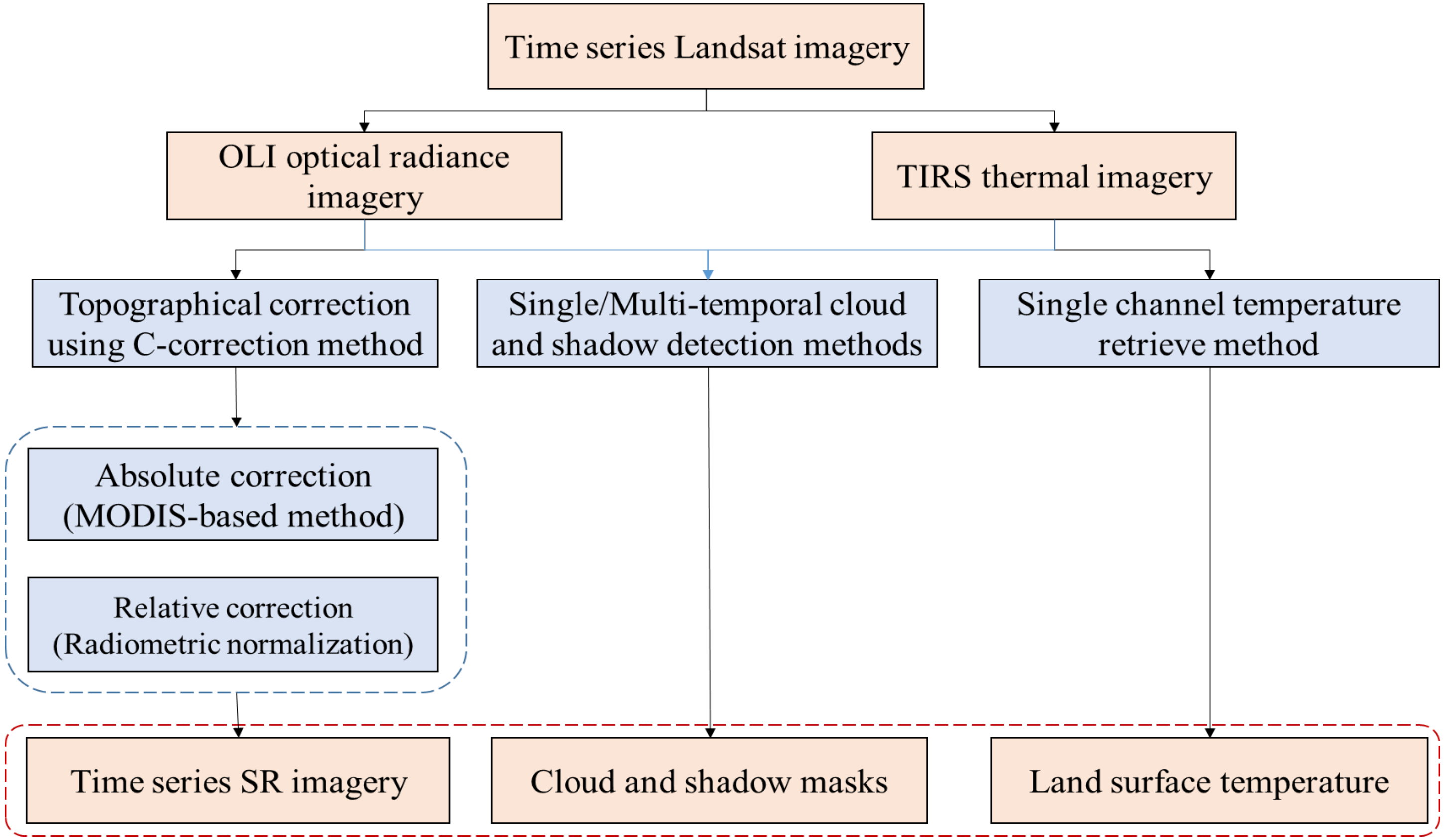

2. Quantitative pre-processing for Landsat imagery

Topographical correction — Theoretical basis

Topographic correction is an important step in the pre-processing of fine-resolution remote sensing images. It includes compensation for differences in solar irradiance and minimizes the variation in observed reflectance for similar targets with different slope and aspect.

$$\rho_H(\lambda) = \rho_T(\lambda) \times \frac{\cos\theta_s + c(\lambda)}{\cos i + c(\lambda)}$$

ρ_H is the corrected reflectance observed for a horizontal surface, ρ_T is the reflectance observed over sloping terrain, θ_s is the solar zenith angle, i is the relative solar incidence angle and c is the correction coefficient:

$$\cos i = \cos\theta_T \times \cos\theta_s + \sin\theta_T \times \sin\theta_s \times \cos(\varphi_T - \varphi_s)$$

where θ_T is the slope angle, φ_T is the aspect angle and φ_s is the azimuth angle. θ_T and θ_s are derivations of the Digital Elevation Model (DEM). The correction coefficient, c, is a wavelength-dependent variable and is derived from a semi-empirical function:

$$\rho(\lambda) = a \times \cos i + b$$

where $c = b/a$, a is the slope and b is the intercept of the linear relationship between the SR and the relative solar incidence angle

2. Quantitative pre-processing for Landsat imagery

Topographical correction — Results

The comparison indicated that the topographical correction could efficiently remove the radiometric difference caused by the terrain slope.

After correction

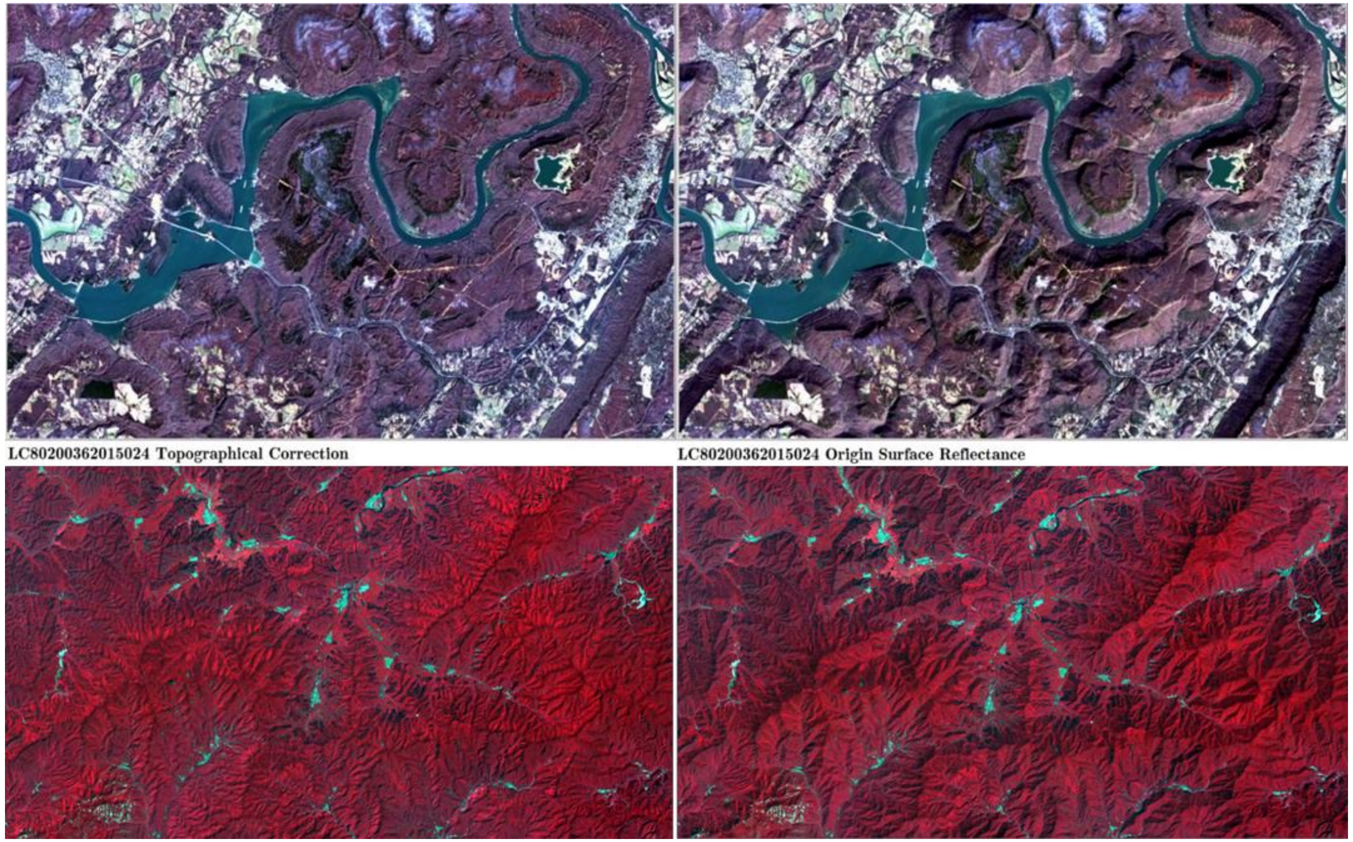

Before correction

2. Quantitative pre-processing for Landsat imagery

Atmospheric correction — Theoretic basis

Atmospheric effects:
Scattering and absorption

Radiative transfer process between surface reflectance ρ_{TOC} and as-sensor reflectance ρ_{TOA}

$$\rho_{TOA} = \boxed{\rho_{path}} + \frac{\boxed{T(\theta_s)T(\theta_v)} \times \rho_{TOC}}{1 - \boxed{S} \times \rho_{TOC}}$$

These unknown parameters are decided by the atmospheric components (aerosol, water vapor and ozone).

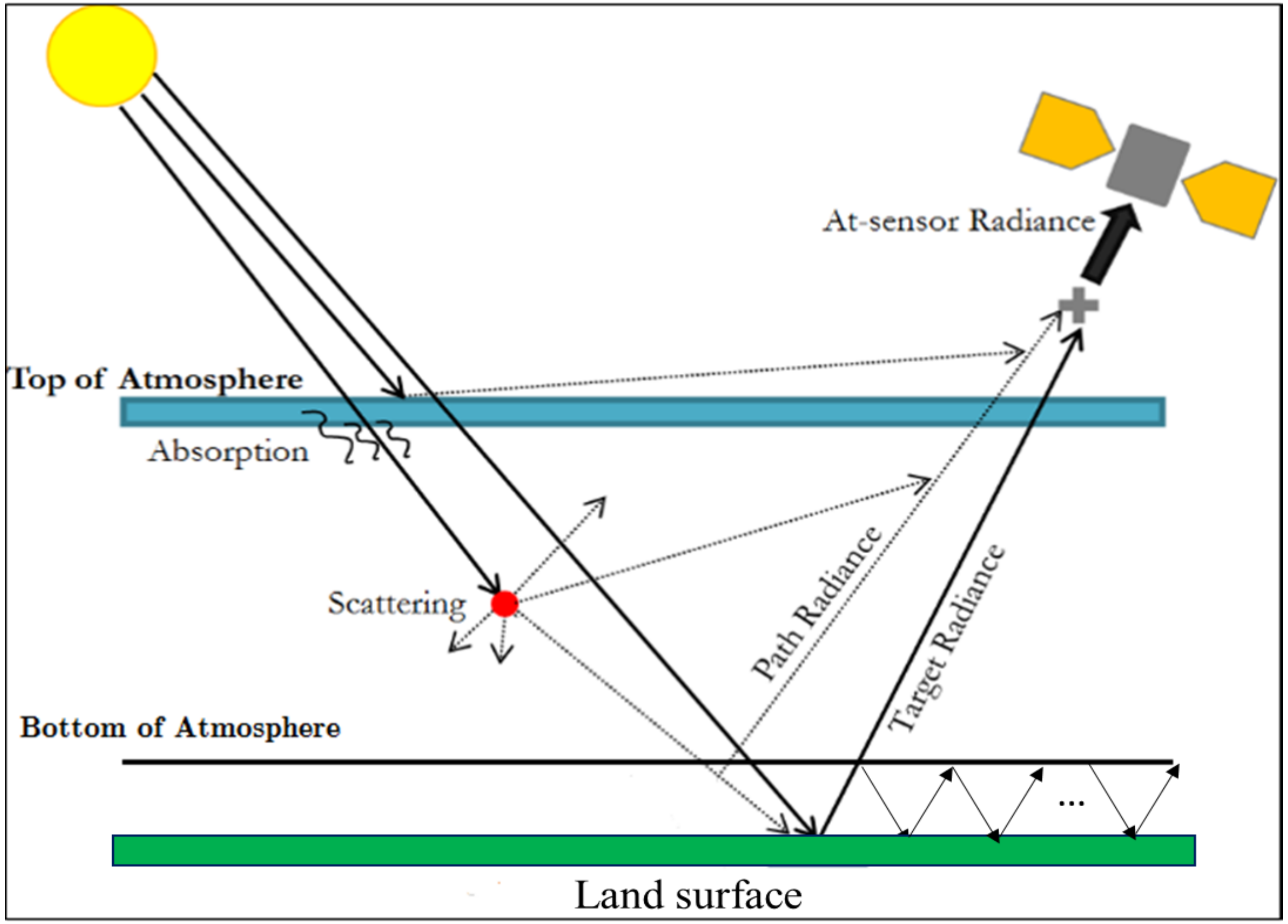

2. Quantitative pre-processing for Landsat imagery

Atmospheric correction using MODIS products and 6S model

Synchronization:

Landsat TM/ETM+/OLI and MODIS Terra sensors share the same polar orbit, with Landsat observations occurring approximately 0.5h before MODIS observations;

Atmospheric products:

MODIS could provide high resolution(0.05 degree) and accurate atmospheric products including AOT、WV and OZONE.

Product ID	Product description	Data field
MOD04_L2	L2 Aerosol, 5-Min Swath 10km	Optical_Depth_Land_And_Ocean
MOD05_L2	L2 Total Precipitable Water Vapor, 5-Min Swath 1km and 5km	Water_Vapor_Near_Infrared
MOD07_L2	L2 Temperature and Water Vapor Profiles, 5-Min Swath 5km	Total_Ozone

2. Quantitative pre-processing for Landsat imagery

Atmospheric correction using MODIS products and 6S model

Step1: interpolation of MODIS products;

Step2: building look-up table between atmospheric products between correction coefficients using 6S model;

Step3: per-pixel atmospheric correction using look-up tables and the aerosol optical depth product.

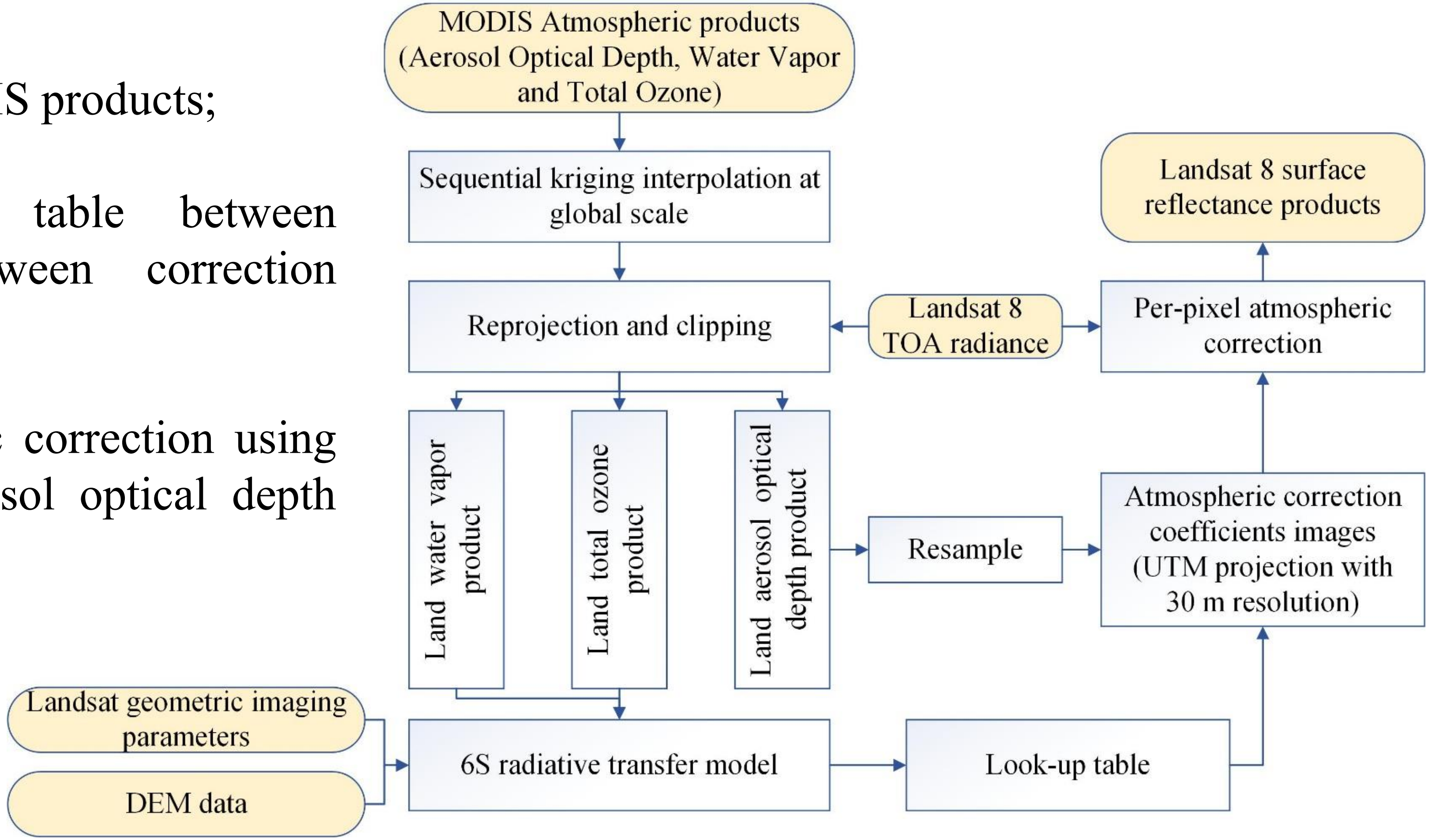

Hu, Y., Liu, L., Liu, L., Peng, D., Jiao, Q., & Zhang, H. (2014). A Landsat-5 atmospheric correction based on MODIS atmosphere products and 6S model. *IEEE Journal of Selected Topics in Applied Earth Observations and Remote Sensing*, *7*(5), 1609-1615.

2. Quantitative pre-processing for Landsat imagery

Kriging interpolation for MODIS atmospheric products

MODIS atmospheric products suffer the problem of missing data especially for aerosol optical depth product, so we firstly needed to interpolate these missing data using the kriging method.

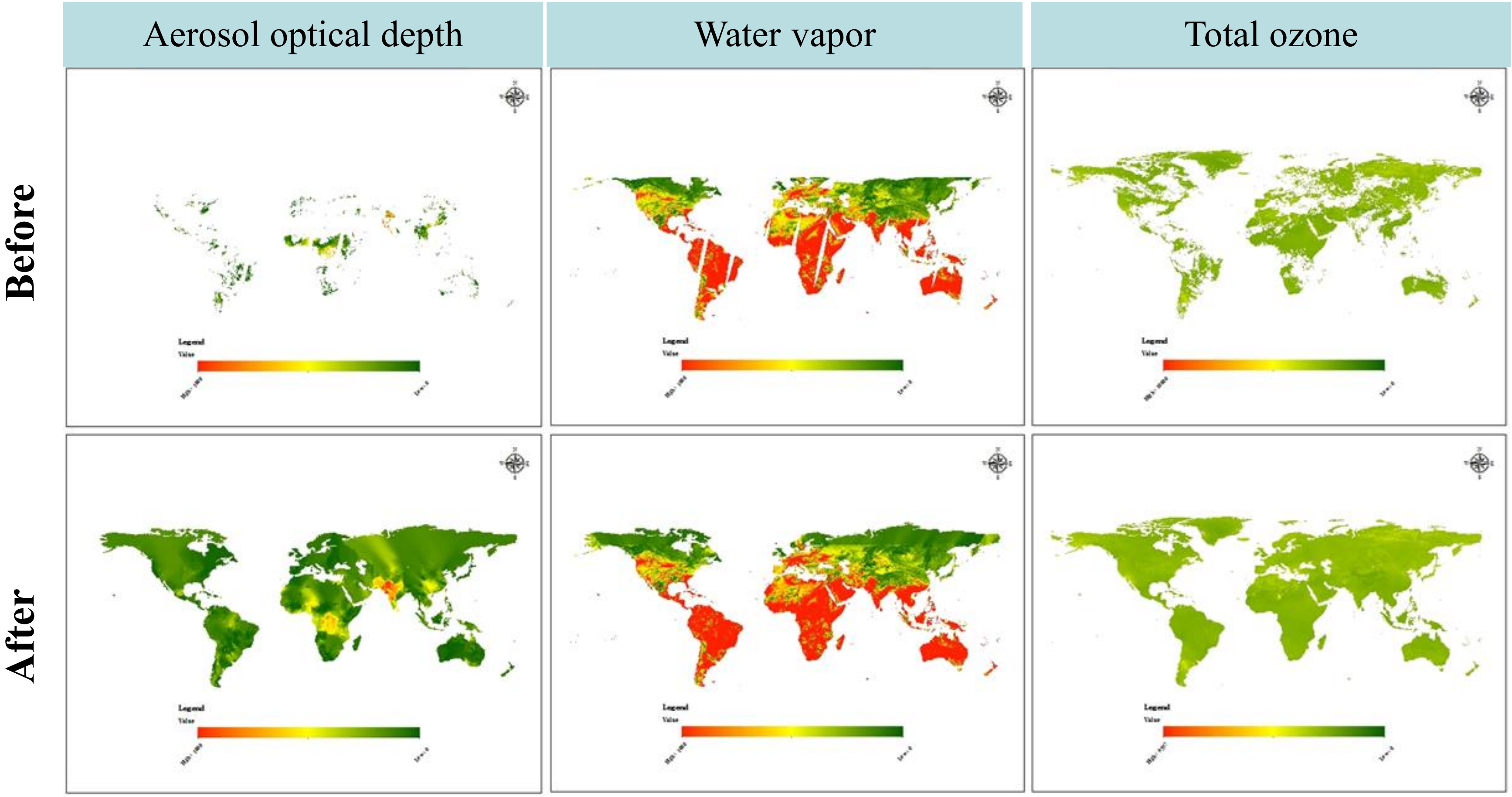

2. Quantitative pre-processing for Landsat imagery

Visual comparison of the effects of atmospheric correction

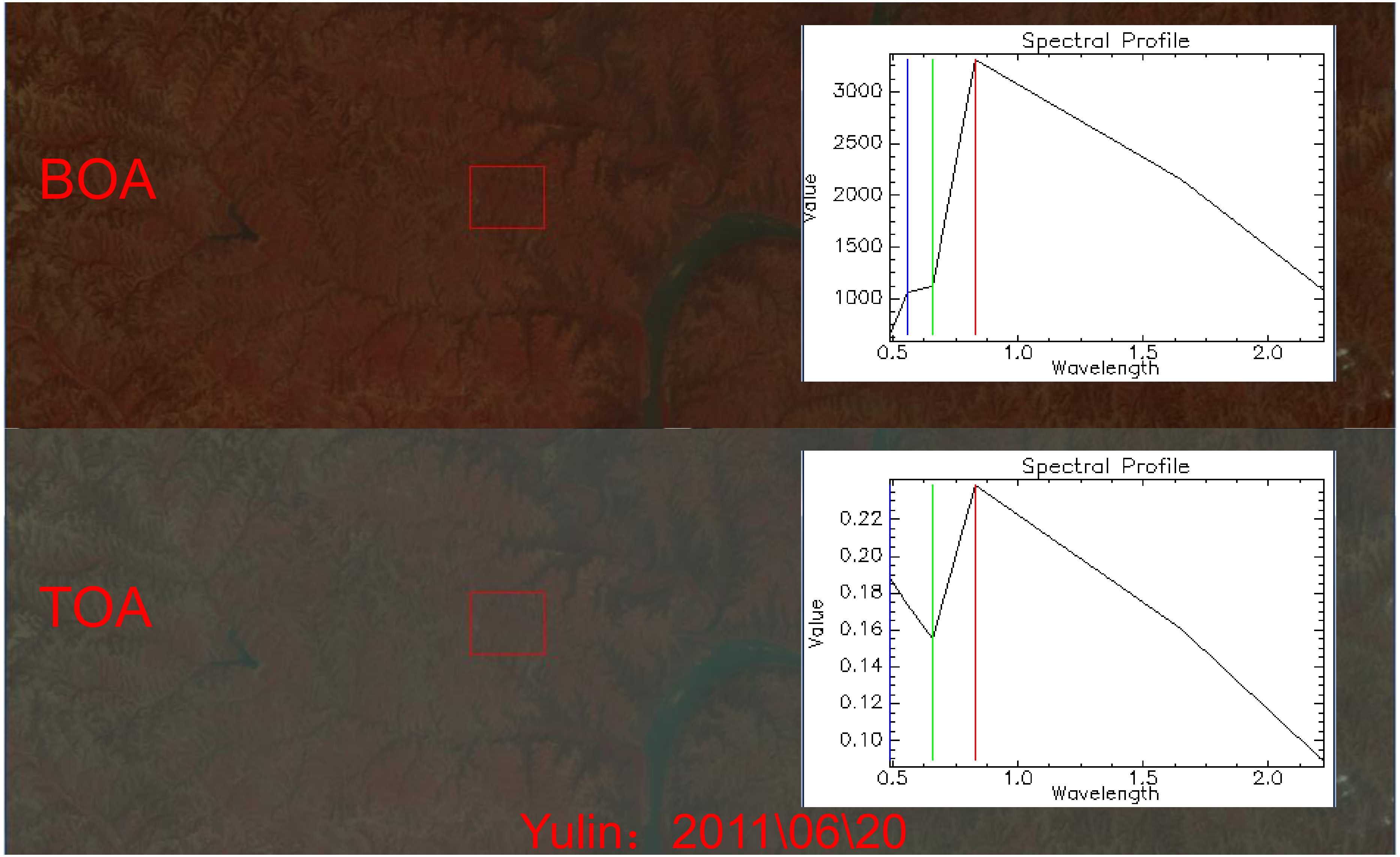

2. Quantitative pre-processing for Landsat imagery

Atmospheric correction — Results

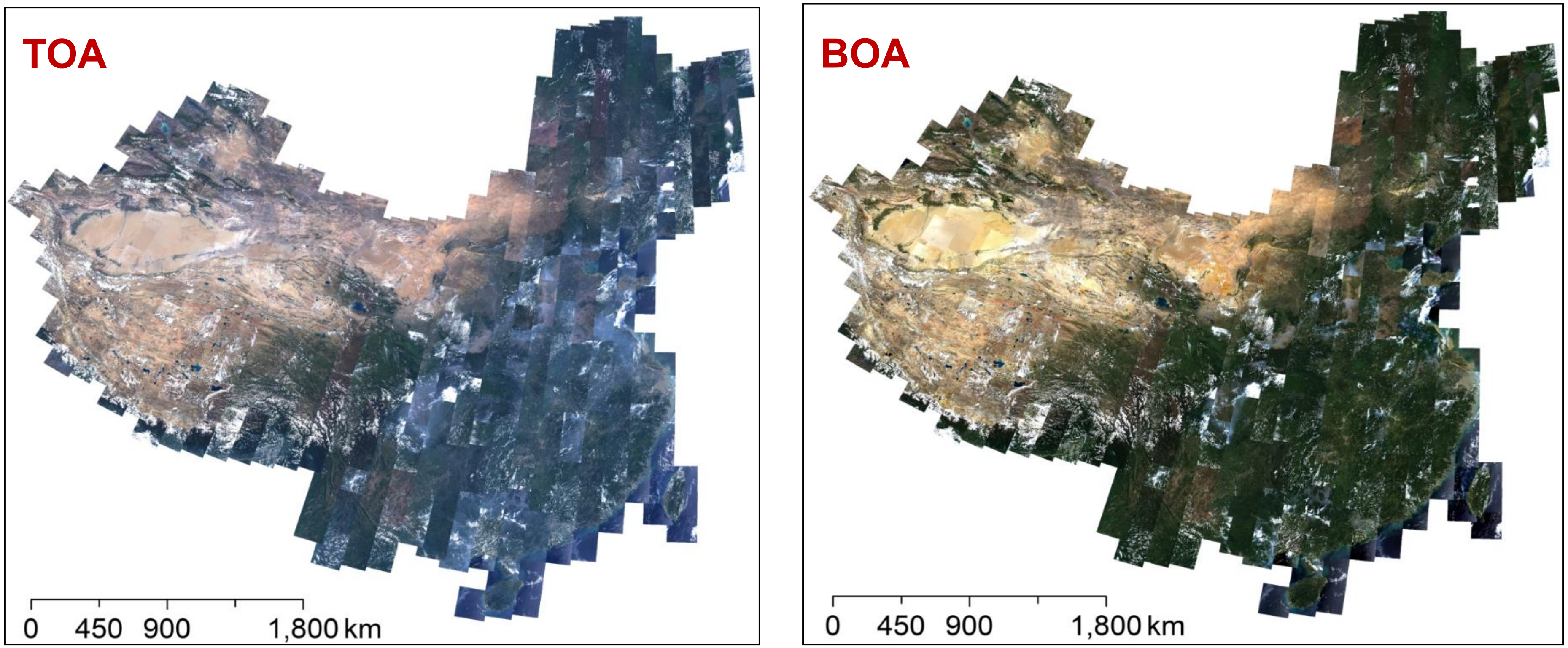

Figure (a). TOA reflectance displayed with true-color composite of China in 2013.
(b). Surface reflectance displayed with true-color using the same contrast stretch as (a)

Wang Y, Liu L, Hu Y, et al. Development and validation of the Landsat-8 surface reflectance products using a MODIS-based per-pixel atmospheric correction method[J]. IJRS, 2016, 37(6): 1291-1314.

2. Quantitative pre-processing for Landsat imagery

Cross-validation using MODIS daily products (MOD09A1)

The RADI SR (produced by the proposed method) is greatly consistent with MODIS daily SR product (MOD09A1) with a mean R2 of 0.93 and an RMSE of 0.023.

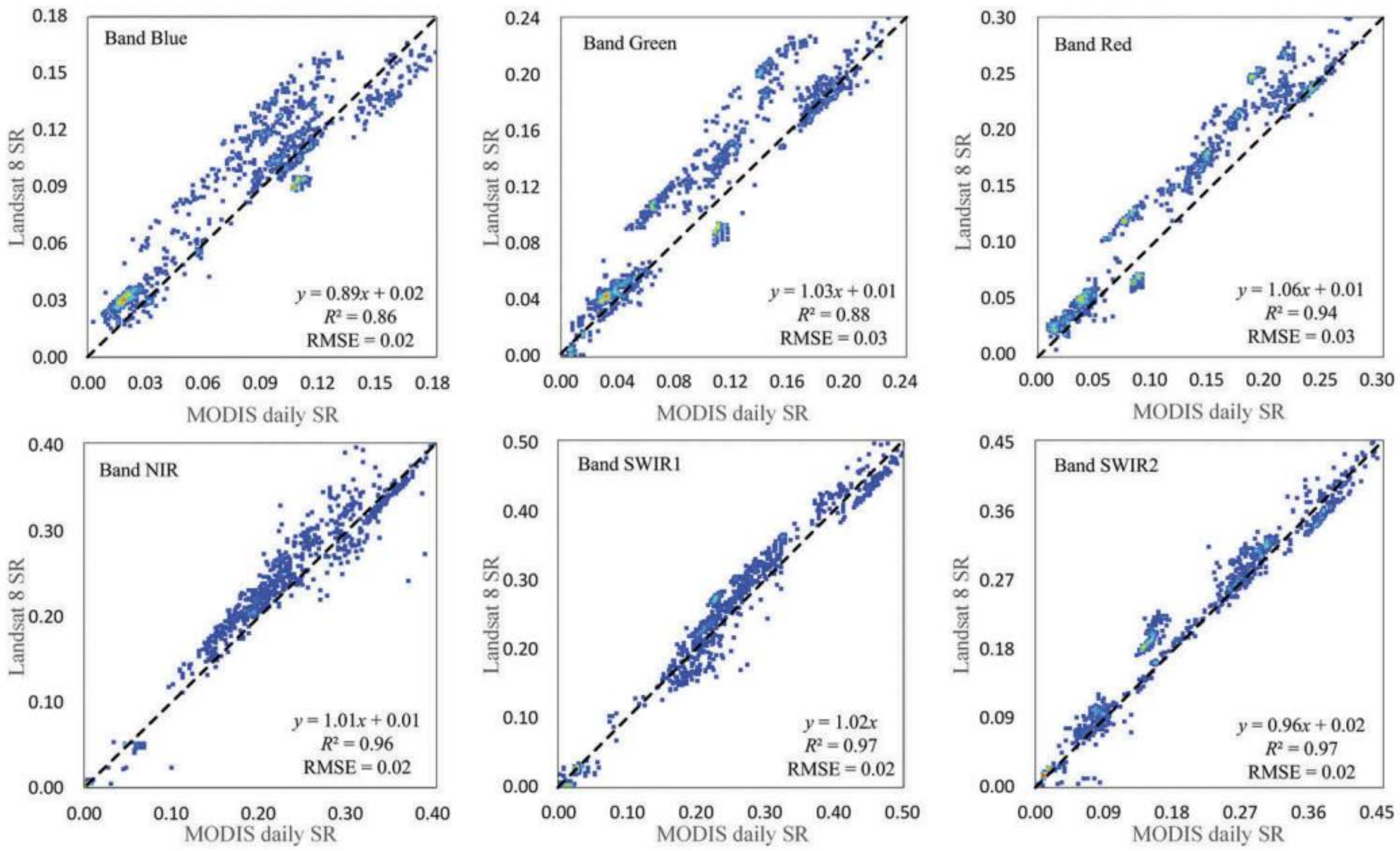

2. Quantitative pre-processing for Landsat imagery

Cross-validation using Landsat SR provided by USGS

The RADI SR (produced by the proposed method) is greatly consistent with USGS SR product with a mean R2 of 0.97 and an RMSE of 0.01.

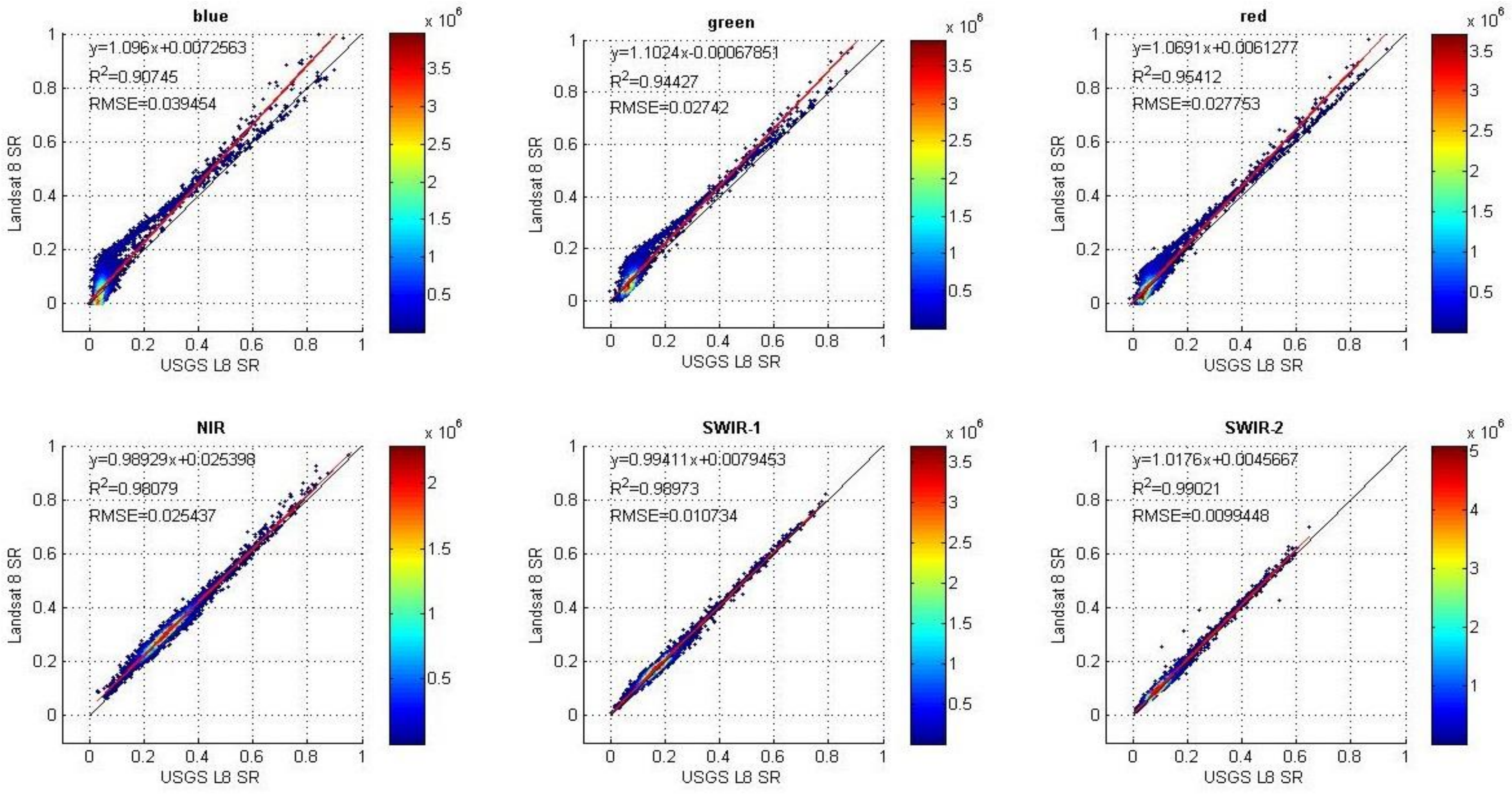

2. Quantitative pre-processing for Landsat imagery

Relative correction — Radiometric normalization

Question

- Landsat long time-series imagery (1972-now);
- The MODIS-based atmospheric correction method is only suitable for Landsat imagery after 2000 because of the lack of MODIS atmosphere products before 2000;
- How to guarantee the radiometric accuracy for long time series Landsat imagery?

Solve method

Atmospheric correction (After 2000) + Radiometric normalization (Before 2000) = Long time-series surface reflectance

2. Quantitative pre-processing for Landsat imagery

Radiometric normalization — Flowchart

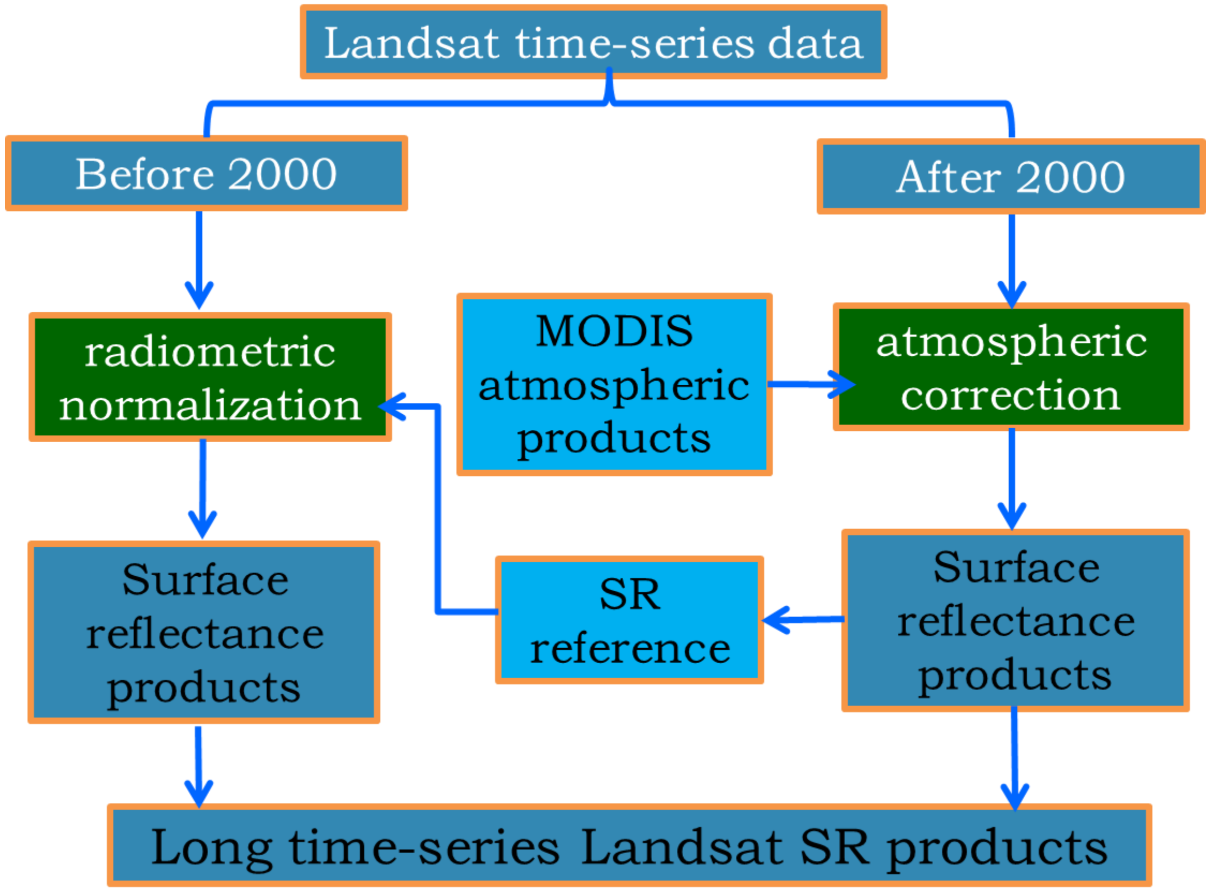

The key of radiometric normalization method is to use the corrected SR imagery after 2000 as reference to normalize the Landsat image before 2000 according to the imaging date.

Liu, L., et al. (2013). Mapping afforestation and deforestation from 1974 to 2012 using Landsat time-series stacks in Yulin District, a key region of the Three-North Shelter region, China. *Environmental monitoring and assessment*, *185*(12), 9949-9965.

2. Quantitative pre-processing for Landsat imagery

Radiometric normalization — Method

1. A multivariate alteration detection transformation was used to select the “no-change” pixels between reference image and target image,

2. using the “no-change” pixels, the relative radiometric normalization coefficients was determined based on orthogonal linear regression ,

3. the coefficients were applied to normalize the target image

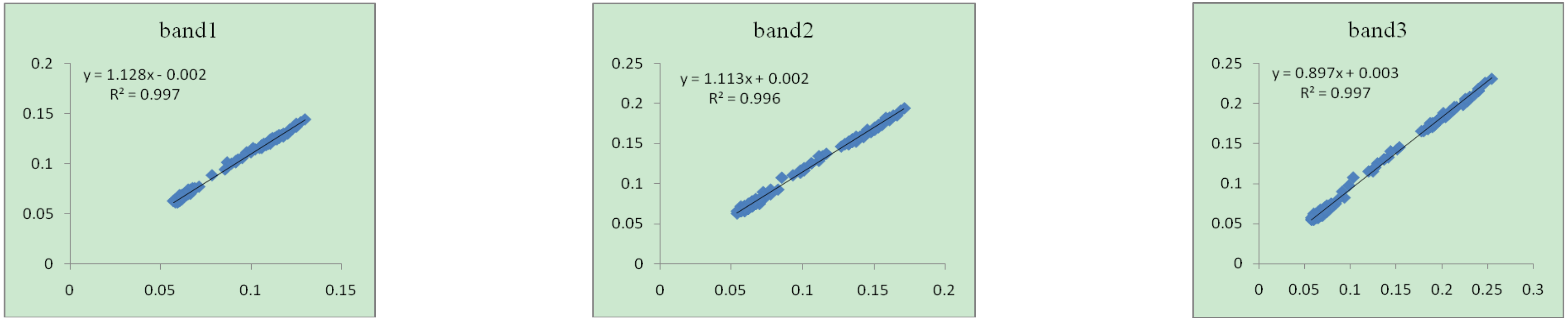

scatter plots of “no-change” pixels, X-axis is target image, Y-axis is reference image

2. Quantitative pre-processing for Landsat imagery

Radiometric normalization — Results

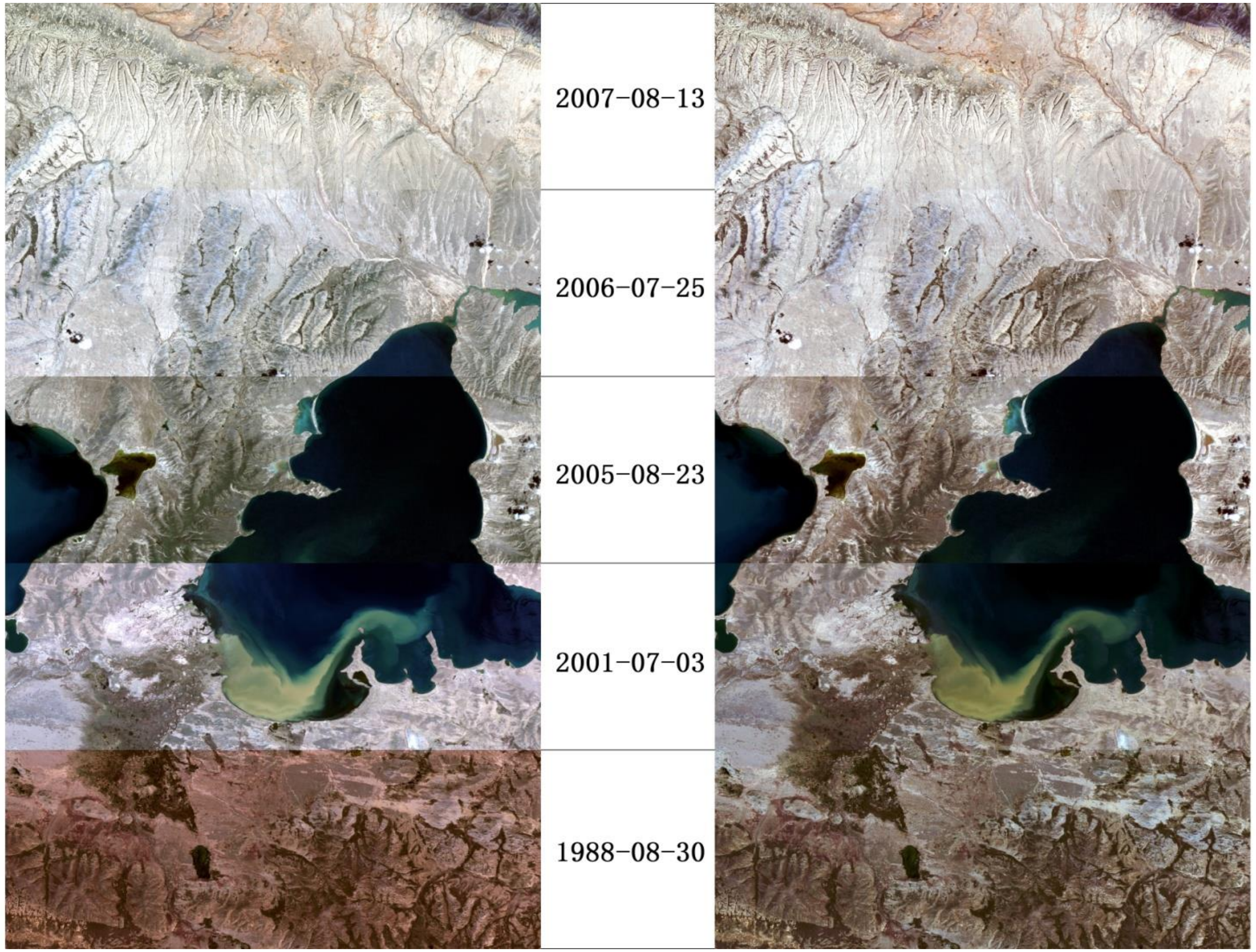

Mosaic of reference and subject images. The left is a mosaic of original TOA reflectance images, and the right is a mosaic of reference reflectance image and normalized images which displayed with same stretch parameters as left. RGB composite: R (band 3), G (band 2), B (band 1).

HU, Y., LIU, L., CACCETTA, P., & JIAO, Q. (2015). Landsat time-series land cover mapping with spectral signature extension method. *Journal of Remote sensing*, 19 (4), 639-656.

2. Quantitative pre-processing for Landsat imagery

Landsat datacube (Global 3-level land grid)

1) The across-track scene overlap distance increase as the latitude increases;
2) The global grid was defined in an equal area projection to ensure that the surface area sensed by each Landsat acquisition was sampled with the same spatial grid density.

Therefore, in order to improve the Landsat use efficiency, we should abandon traditional storage pattern with the scene as the management unit.

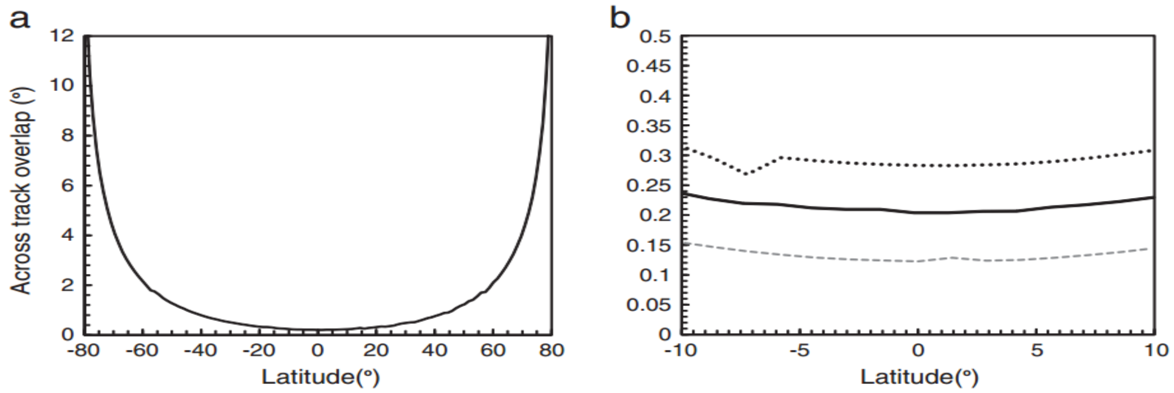

The sinusoidal equal area projection was used as it provides a global uninterrupted projection. The grid spacing was set sufficiently small to capture the variable geographic location and extent of Landsat acquisitions and scene overlap imposed by the Landsat sensor and orbit geometry (Kovalskyy and Roy, 2013).

Kovalskyy, V. and D. P. Roy (2013). "The global availability of Landsat 5 TM and Landsat 7 ETM+ land surface observations and implications for global 30m Landsat data product generation." Remote Sensing of Environment **130**: 280-293.

2. Quantitative pre-processing for Landsat imagery

Landsat datacube (Global 3-level land grid)

The grid is defined in the sinusoidal equal area projection and is composed of 6,138,864 land grid grids spaced every 5.559752 km in the X and Y axes of the sinusoidal coordinate system

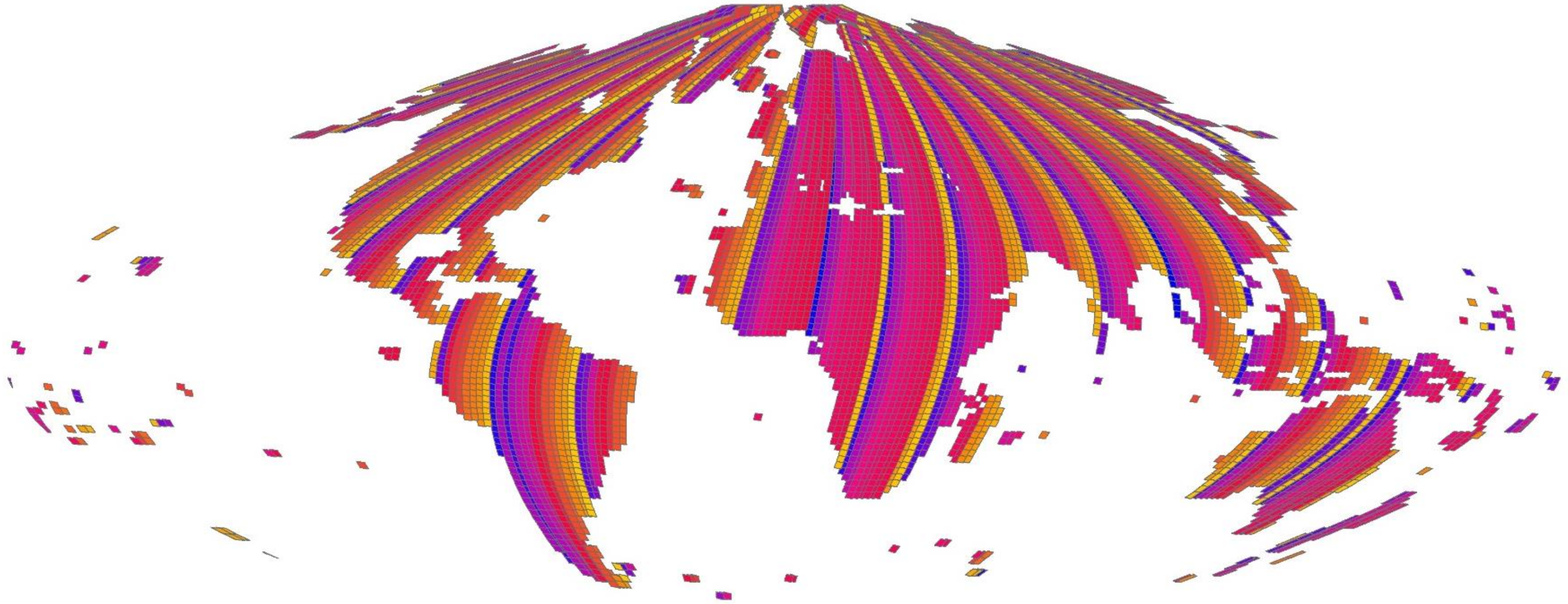

Minimum land grid naming rule: LTS_Ref_hh26vv05h3v4_p17r23_2015243.dat

2. Quantitative pre-processing for Landsat imagery

Landsat datacube (Global 3-level land grid)

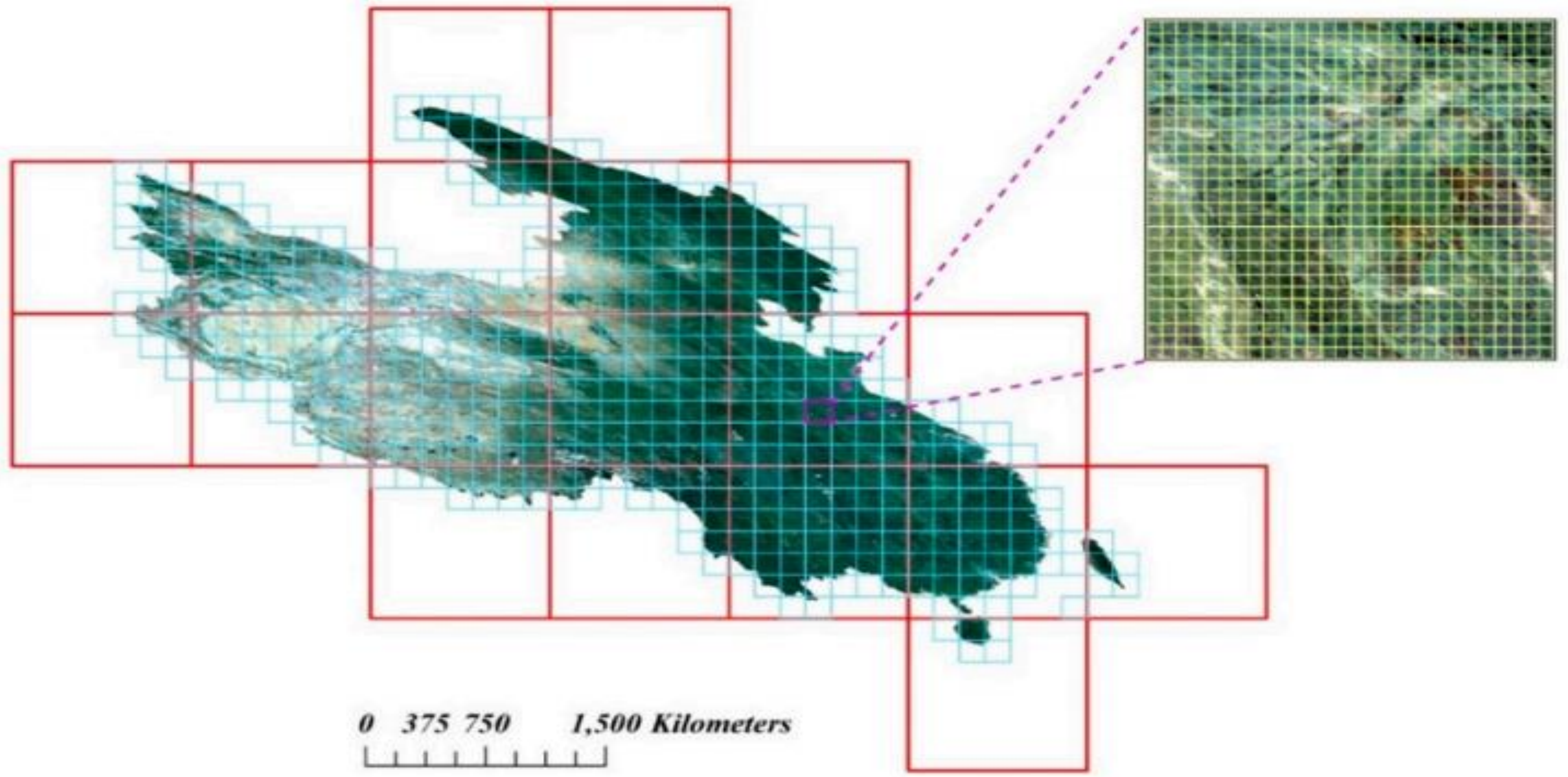

2. Quantitative pre-processing for Landsat imagery

Landsat datacube (Global 3-level land grid)

A total of 6500 Landsat imagery over China has been tiled into Landsat datacube, and the temporal frequency of Landsat imagery in each geographical location was calculated. The results indicated that the tiling process could improve the Landsat use efficiency, especially over the overlapping areas.

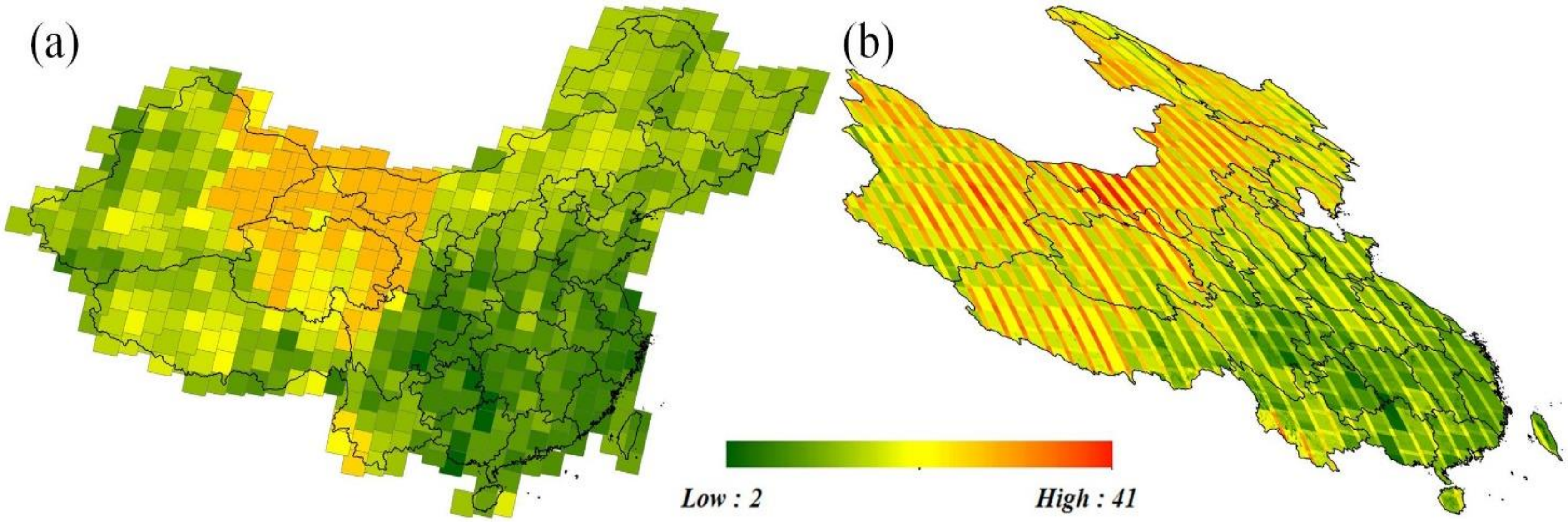

Zhang, X., Liu, L., Chen, X., Xie, S., & Gao, Y. (2019). Fine Land-Cover Mapping in China Using Landsat Datacube and an Operational SPECLib-Based Approach. *Remote Sensing*, *11*(9), 1056.

2. Quantitative pre-processing for Landsat imagery

Landsat datacube — Restoration of unclear pixels (cloud, shadow pixels)

Cloud and shadow contamination is inevitable especially for low latitude areas. For multi-temporal classification, the cloud and shadow should be restored beforehand using spatio-temporal methods.

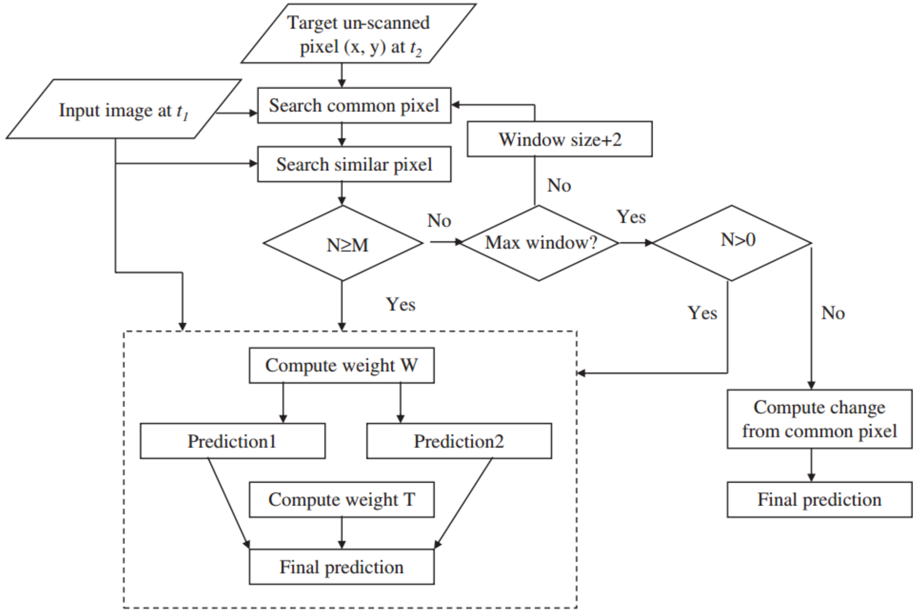

+

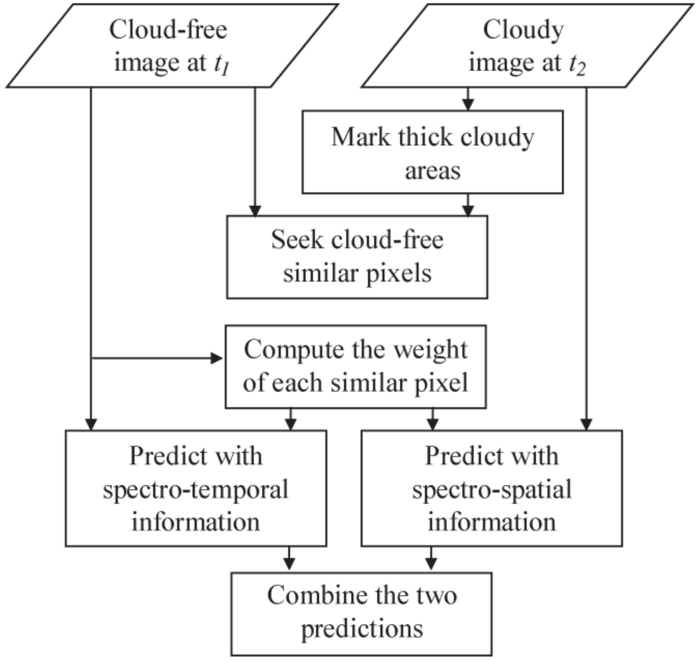

Zhu, X., et al. (2012). "A Modified Neighborhood Similar Pixel Interpolator Approach for Removing Thick Clouds in Landsat Images." IEEE Geoscience and Remote Sensing Letters **9**(3): 521-525.
Chen, J., et al. (2011). "A simple and effective method for filling gaps in Landsat ETM+ SLC-off images." Remote Sensing of Environment **115**(4): 1053-1064.

2. Quantitative pre-processing for Landsat imagery

Landsat datacube — Restoration results

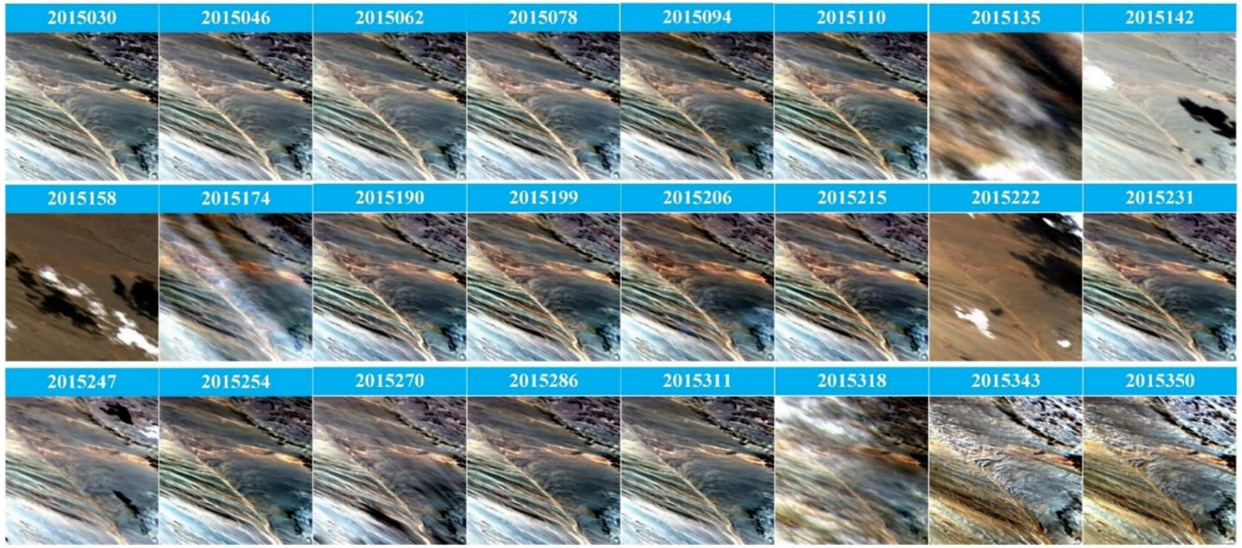

Original time series Landsat SR

Time series Landsat SR after filling

Contents

3. Forest disturbance monitoring and biomass mapping

Background

Within the framework of the North American Carbon Program (NACP), the North American Forest Dynamics (NAFD) project has evaluated forest disturbance and regrowth history for the conterminous U.S. by combining Landsat observations and field measurements (Goward et al. 2008).

The NAFD project uses the Vegetation Change Tracker (VCT), an automated forest change analysis algorithm, on temporally dense (annual or biennial) Landsat Time Series Stack (LTSS) of images and produces forest disturbance data products (Huang et al. 2010). The algorithm consists of two major steps: 1) individual image analysis and 2) time series analysis.

VCT produces a disturbance product where each pixel is labeled as either a static land class (persistent non-forest, persistent forest, or persistent water) or with the year of change for disturbed forest pixels.

This data set provides the results of time-series analyses of Landsat imagery for 55 selected forested sites across the conterminous U.S.A. The output is a pair of disturbance data products for each site, one showing the first year of disturbance in the time series, the other showing the last year of disturbance. The time period analyzed is approximately 1984-2009.

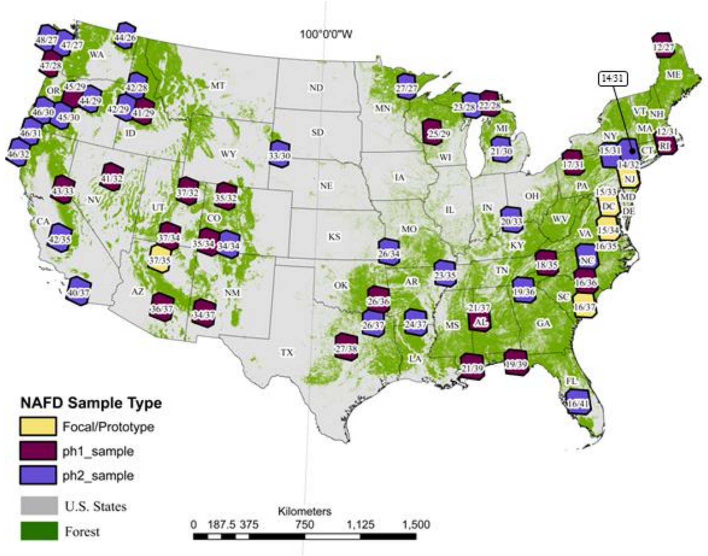

3. Forest disturbance monitoring and biomass mapping

Background

http://daac.ornl.gov/NACP/guides/NAFD_Disturbance_guide.html

The first year of forest disturbance map for an area in Mississippi (p21r37) where industrial forestry is prevalent. The legend details the map classification system. The first three map categories are static classes which are consistent throughout the time series: persistent non-forest, persistent forest, and water. Forest change pixels are classified according to the year in which change occurred. Actual disturbance year classes vary according to the image dates present in each individual LTSS.

3. Forest disturbance monitoring and biomass mapping

Study Area and experiments

Three North forest program began in 1978 and will be finished in 2050.The project will take place in three stages (1978–2000, 2001–2020, and 2021–2050) following eight engineering schedules.

The key goal of this program in the following decades was to improve forest coverage in arid and semiarid China from 5% to 15% by using this program as the primary method to combat desertification and to control dust storms. Wang et al (2010)

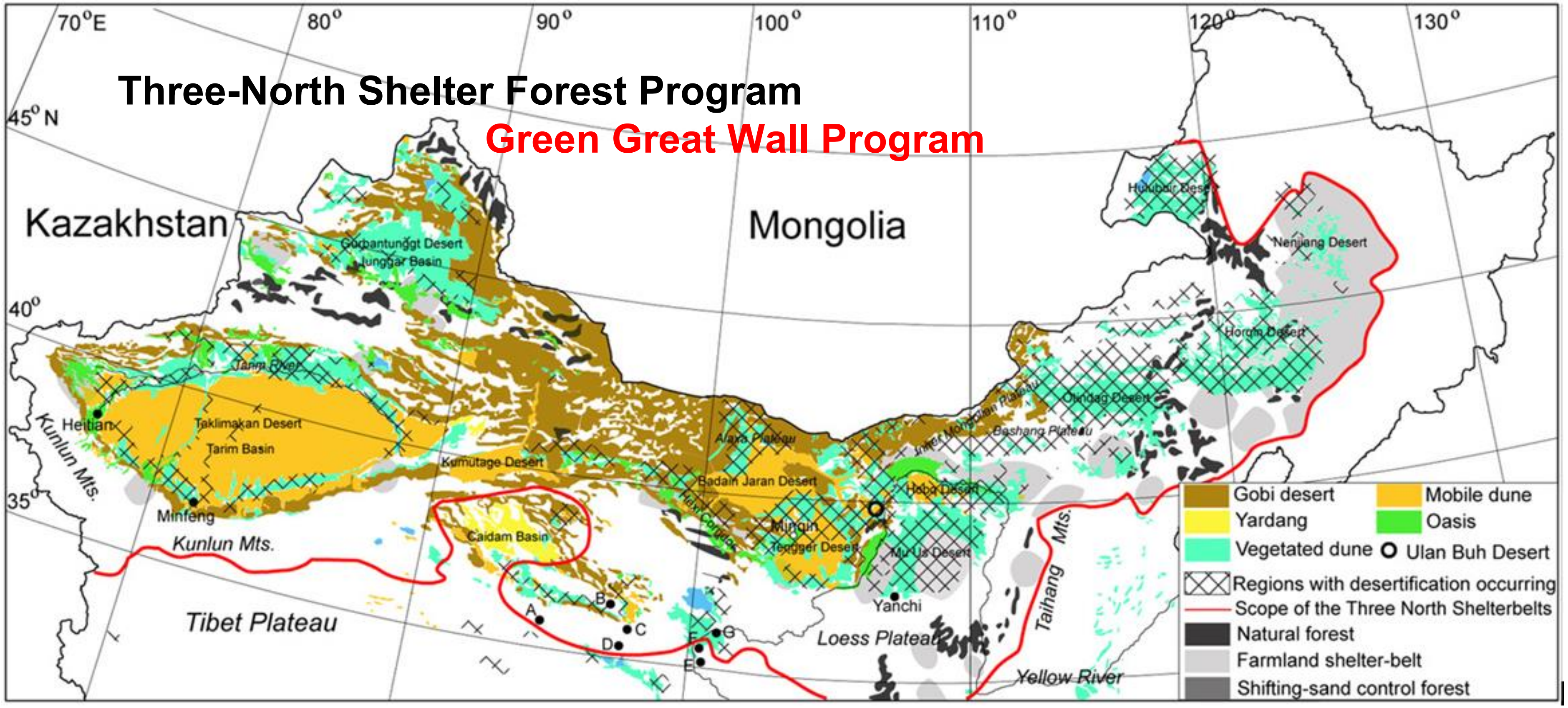

3. Forest disturbance monitoring and biomass mapping

Study Area and experiments

GPS	Longitude	Latitude	Age
52	38° 47'23.79"N	110° 15'6.32"E	5-10
55	38° 03'30.11" N	110° 28'4.52" E	10
56	38° 04'5.12" N	110° 27'43.93" E	10
57	38° 05'23.13" N	110° 27'9.58" E	10
60	38° 07'32.83" N	110° 23'50.79" E	40
63	38° 18'1.86" N	110° 11'51.32" E	43
64	38° 18'0.97" N	110° 11'55.92" E	45
65	38° 17'48.37" N	110° 12'7.67" E	8
861	38° 17'50.40" N	110° 12'9.99" E	30
66	38° 18'32.21" N	110° 11'52.79" E	30
67	38° 15'26.22" N	110° 15'8.57" E	13
72	38° 15'36.94" N	110° 14'46.20" E	28
69	38° 15'49.87" N	110° 15'16.59" E	26
70	38° 15'48.32" N	110° 15'22.23" E	30
71	38° 15'54.28" N	110° 15'44.55" E	30
36	38° 17'25.99" N	110° 00'35.01" E	5-10
98	38° 12'39.24" N	109° 45'38.38" E	40
74	38° 04'14.37" N	109° 49'56.10" E	10
75	38° 04'27.08" N	109° 49'58.32" E	12
76	38° 01'48.77" N	109° 50'18.88" E	40
77	38° 01'54.07" N	109° 50'29.76" E	40
78	37° 59'26.16" N	109° 50'28.65" E	40
S1	38° 05'5.84" N	109° 31'44.38" E	30
79	38° 06'14.97" N	109° 29'59.97" E	40
S	38° 06'29.57" N	109° 26'29.01" E	40
80	38° 16'36.94" N	110° 07'37.95" E	6-12

27 sites investigated for validation of forest changes forest types, Age Density, Height in 2012 and 2013

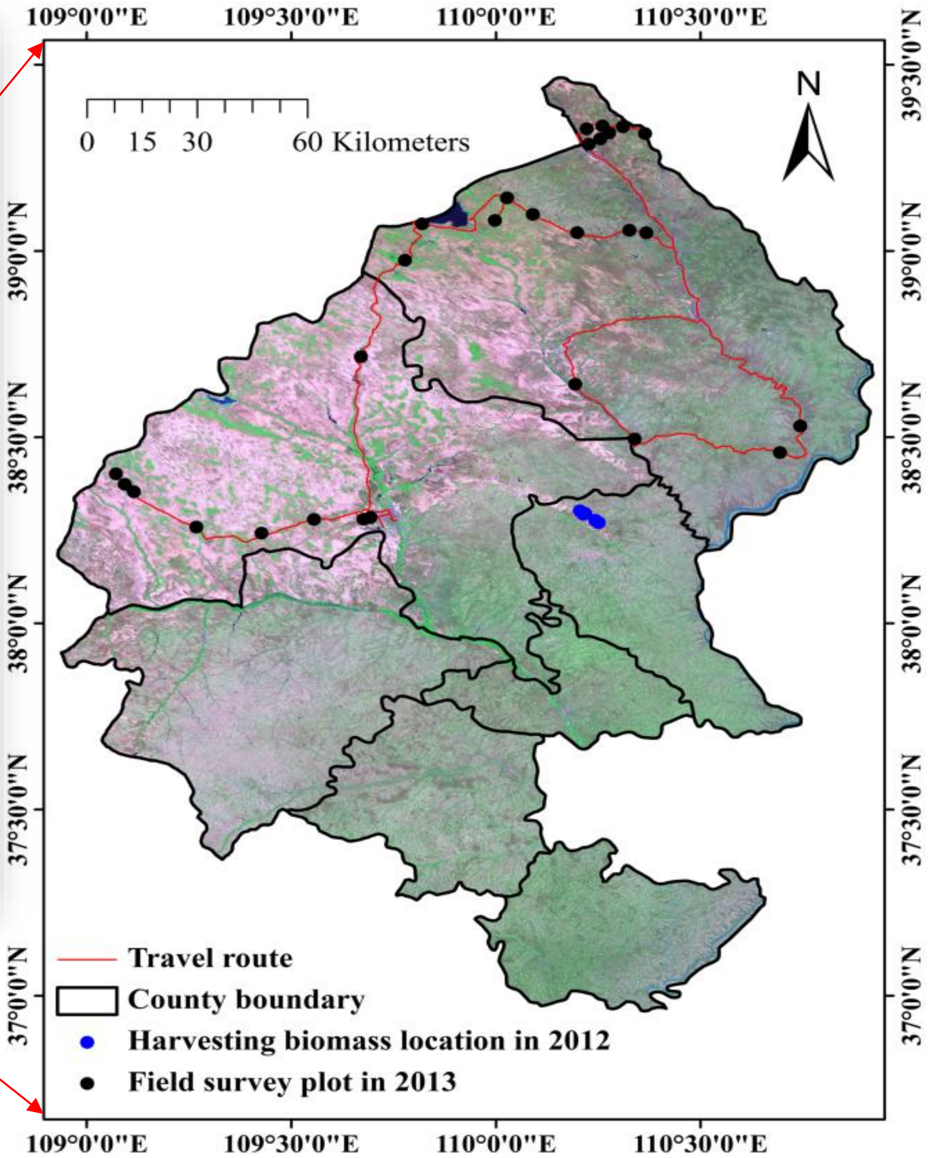

3. Forest disturbance monitoring and biomass mapping

Study Area and experiments

Before

After

3. Forest disturbance monitoring and biomass mapping

➢ Study Area and experiments

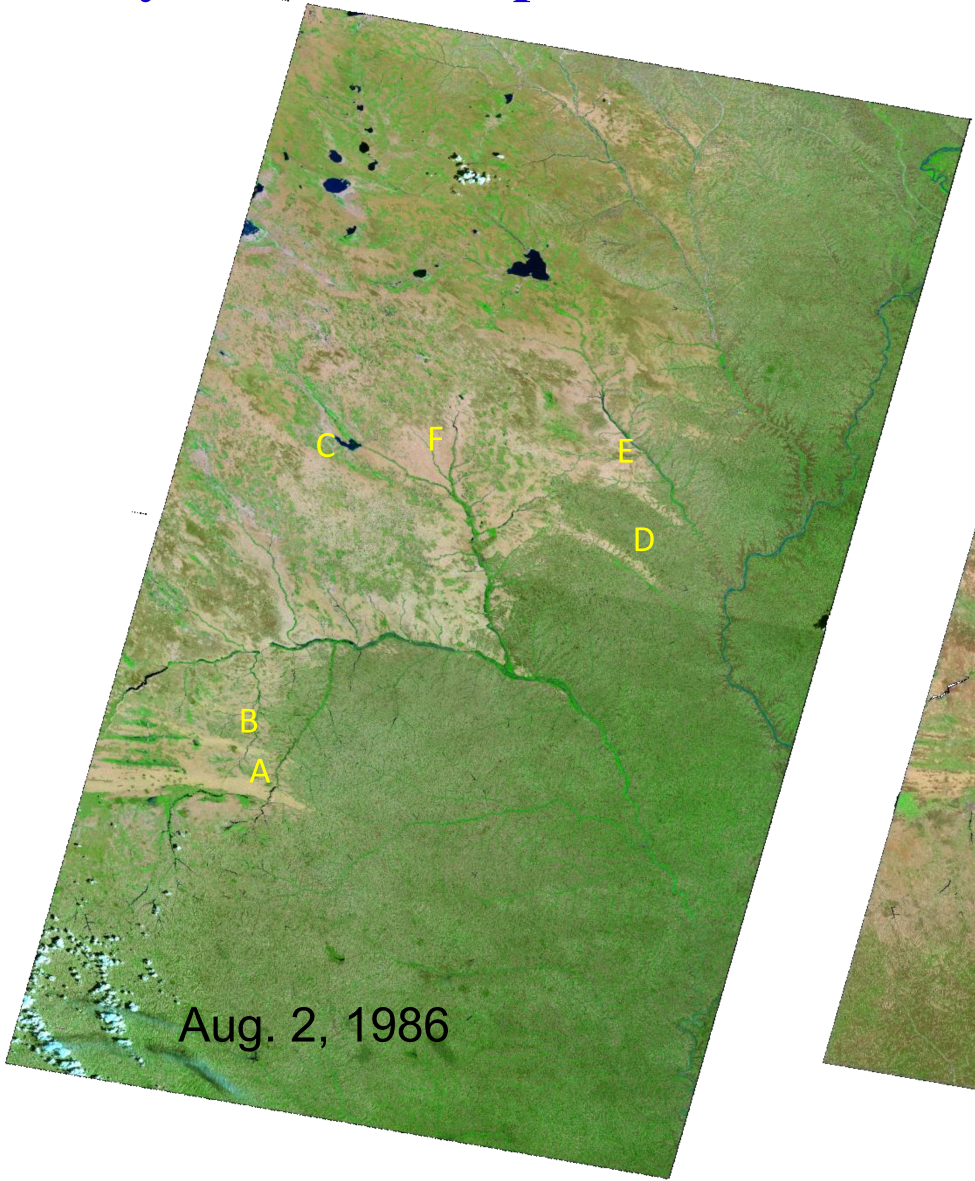

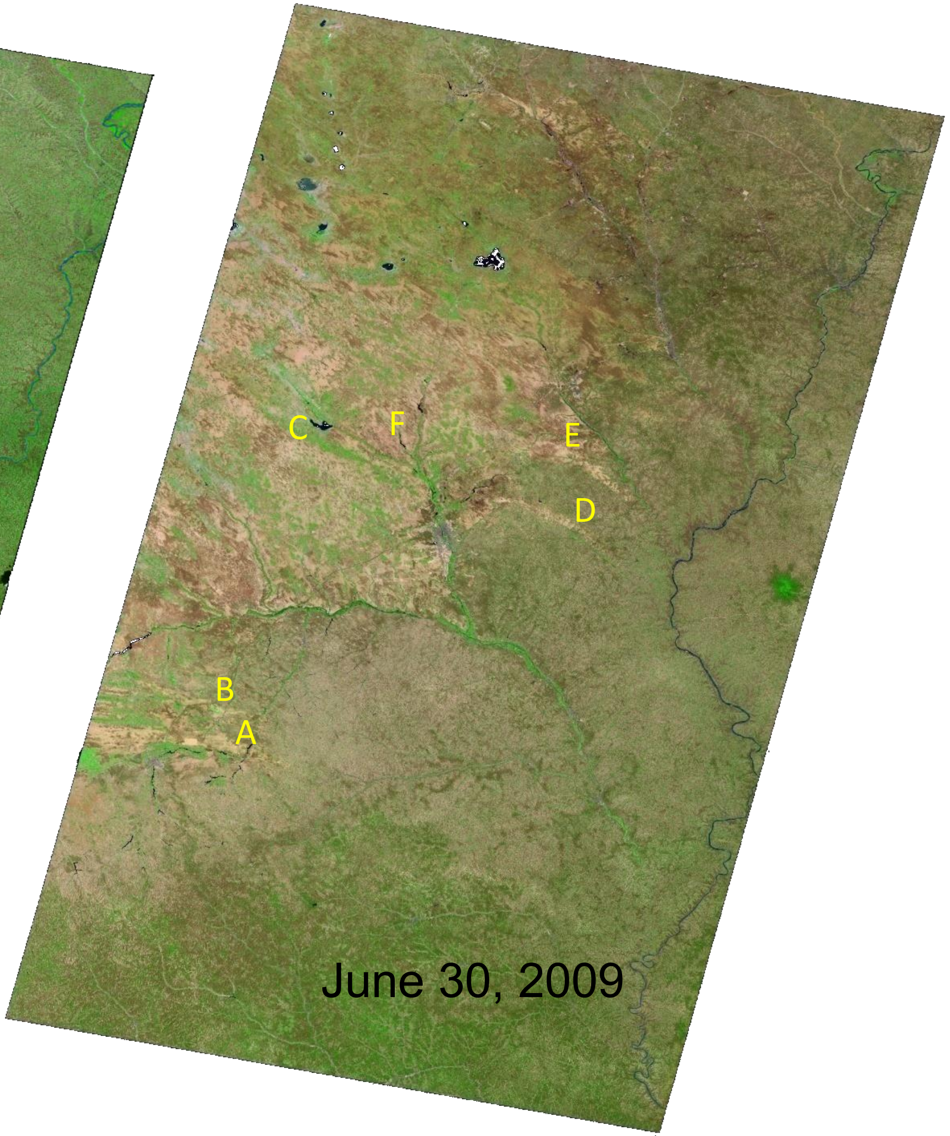

3. Forest disturbance monitoring and biomass mapping

Study Area and experiments

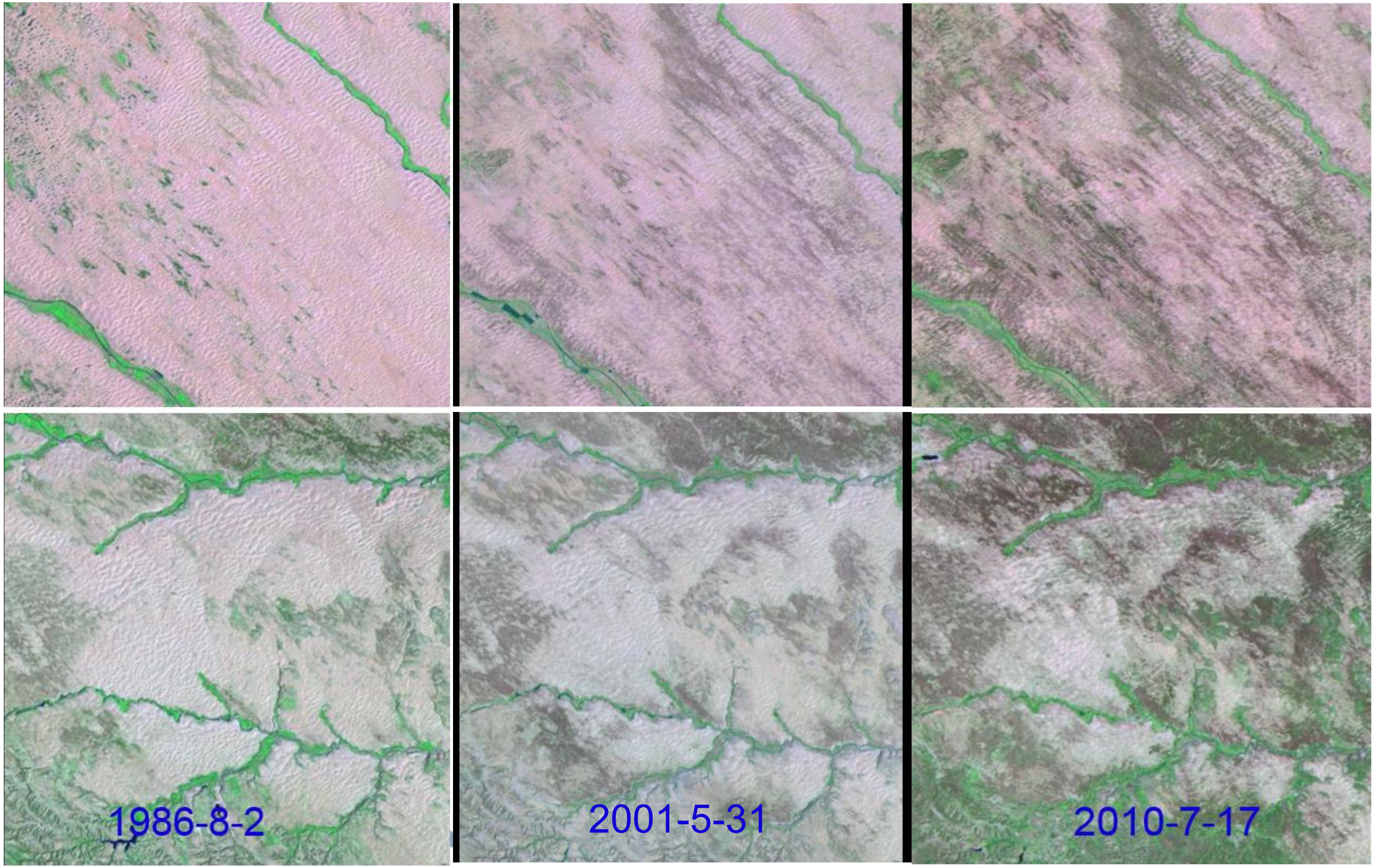

3. Forest disturbance monitoring and biomass mapping

The flowchart of disturbance monitoring and biomass mapping

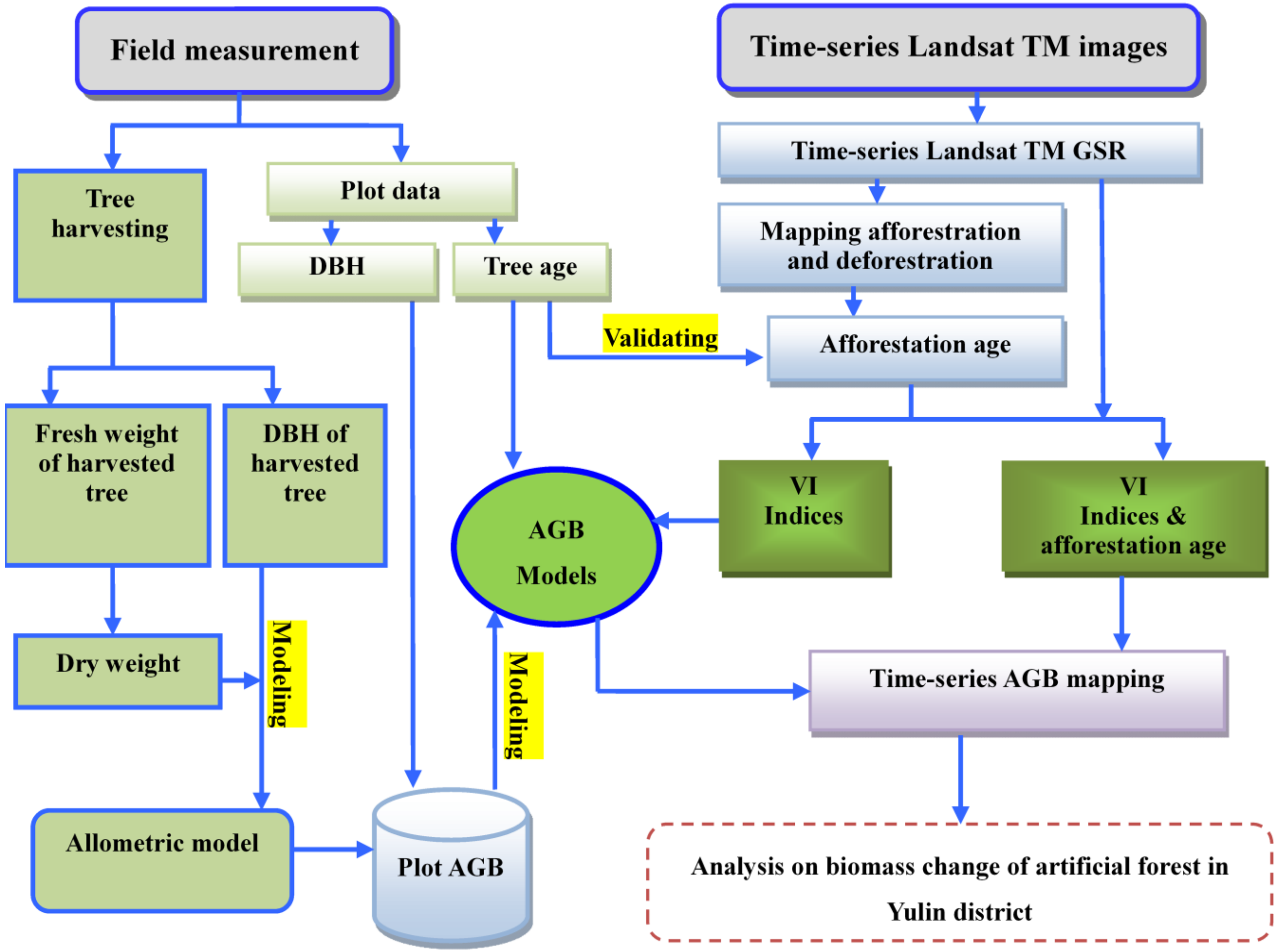

Step 1: Time-series images radiometric correction;

Step 2: Afforestation and deforestation mapping;

Step 3: Forest biomass mapping using empirical model.

3. Forest disturbance monitoring and biomass mapping

Time-series images radiometric correction

Acquisition dates (yyyy-mm-dd) of collected Landsat images

Path/Row	Acquisition date
L5-8 127/33&34	2013-08-22, 2012-06-30, 2011-07-22, 2010-07-17, 2009-06-30, 2008-09-15, 2007-08-12, 2007-05-24, 2006-09-10, 2005-07-29, 2004-09-12, 2003-08-17, 2002-08-06, 2001-05-31, 2000-05-20, 1998-07-02, 1996-06-10, 1995-06-08, 1994-08-24, 1993-06-18, 1992-07-17, 1990-08-29, 1989-09-11, 1988-09-24, 1987-05-17, 1986-08-02
MSS 137/33&34	1978-08-01, 1977-08-15, 1976-09-25, 1975-04-22, 1974-05-24
MSS 136/33&34	1978-09-23, 1977-07-07, 1976-06-26, 1975-06-14, 1973-11-24

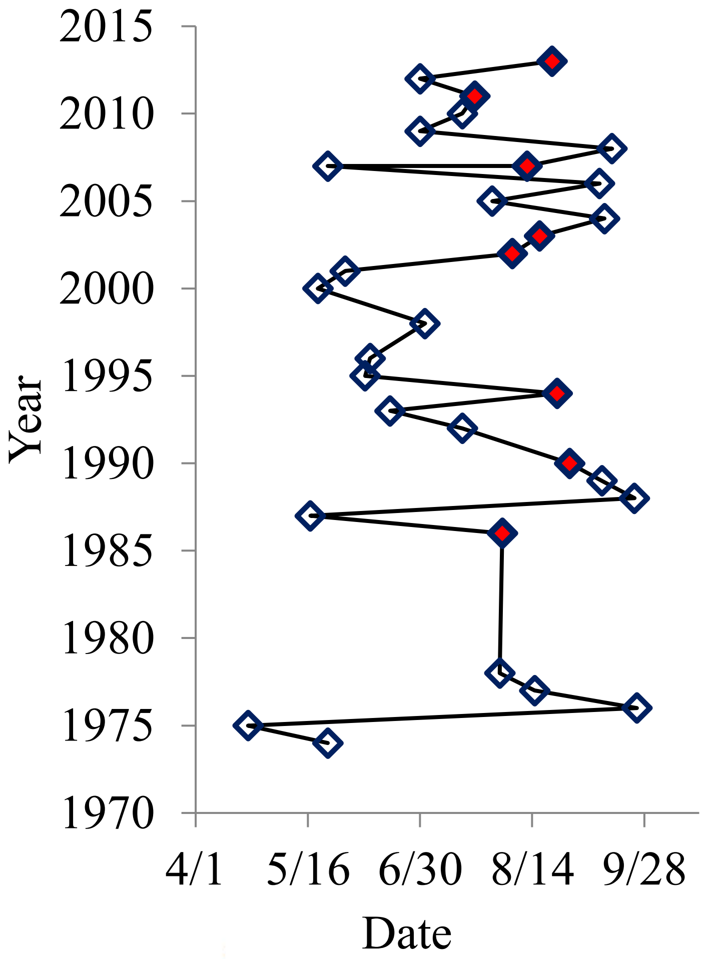

3. Forest disturbance monitoring and biomass mapping

Time-series images radiometric correction

•**Terrain illumination correction.** All the Landsat images were corrected using a C-correction method (Teillet *et al*. 1982) and ASTER DEM (30m) data, using a software developed by CSIRO (Wu *et al*. 2004).

•**Image atmospheric correction for the base image.** The base image (acquired on June 3, 2009) was corrected using an atmospheric correction algorithm adapted from the MODIS 6S radiative transfer approach.

•**Production of ground surface reflectance (GSR) images based on a relative normalization method.**
•We developed a procedure to derive GSR products based on the relative radiance normalization algorithm (Cohen *et al*. 2003). An iterative re-weighted Multivariate Alteration Detection (MAD) algorithm by Cohen *et al*. (2003) was used to detect the invariant target pixels. The Landsat DN images from Step 2 were then matched to the GSR base image from Step 3 by least-square fitting for these invariant pixels, and the time-series Landsat GSR images were produced

3. Forest disturbance monitoring and biomass mapping

Multi-phenological forest z-score for forest mapping

An integrated forest z-score was designed to discriminate forest and non-forest pixels in multi-spectral images (Huang *et al.* 2009). With training forest pixels determined according to ground surveys or visual interpretation, the mean $\bar{b}_i$ and standard deviation (SD_i) of band i for the raining forest samples can be calculated from the GSR image. The forest z-score (FZ_i) value for that band is defined:

$$FZ_i = \frac{(b_i - \overline{bi})}{SD_i} \qquad IFZ = \sqrt{\frac{1}{NB}\sum_{i=1}^{NB}(FZ_i)^2}$$

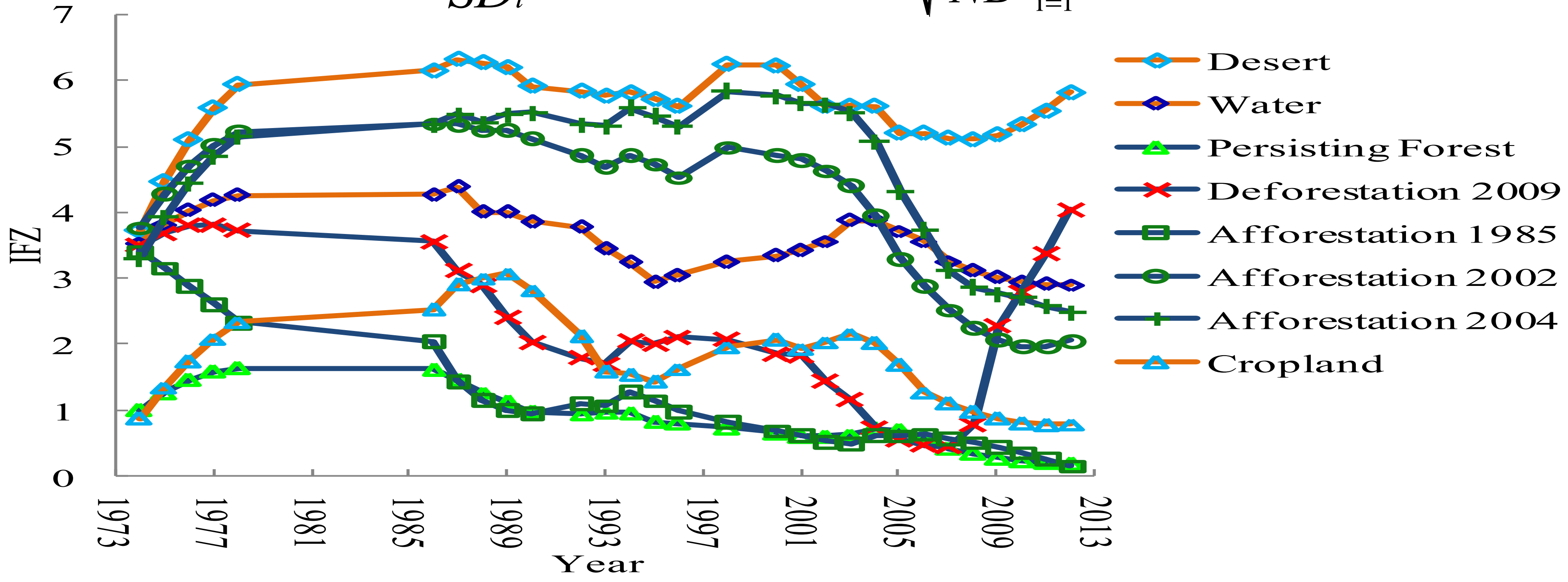

3. Forest disturbance monitoring and biomass mapping

Vegetation Change Tracker (VCT) method based on IFZ

Flowchart to map land covers and forest changes using the dense time series of IFZ and reflectance data.

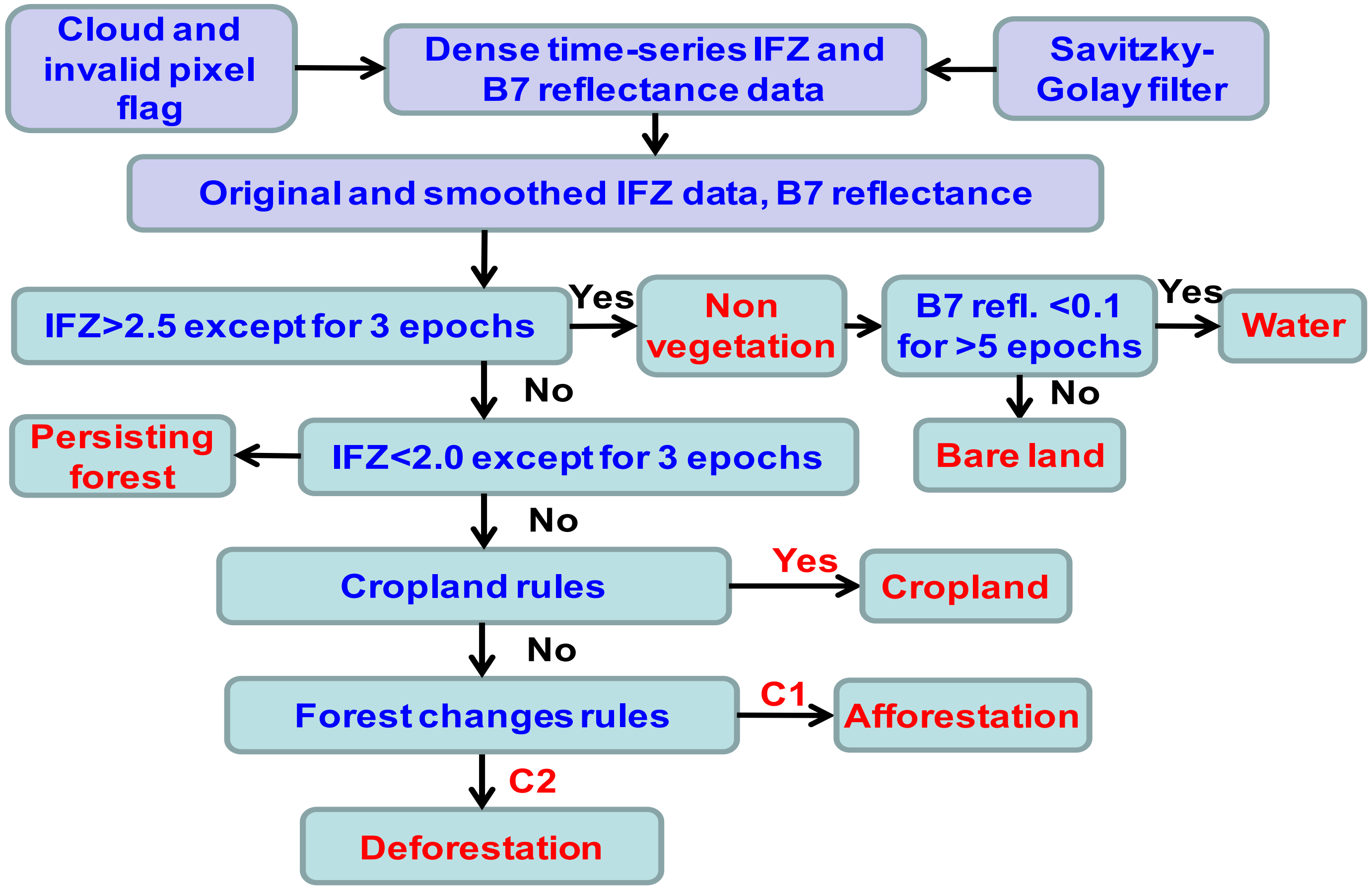

3. Forest disturbance monitoring and biomass mapping

Forest disturbance results

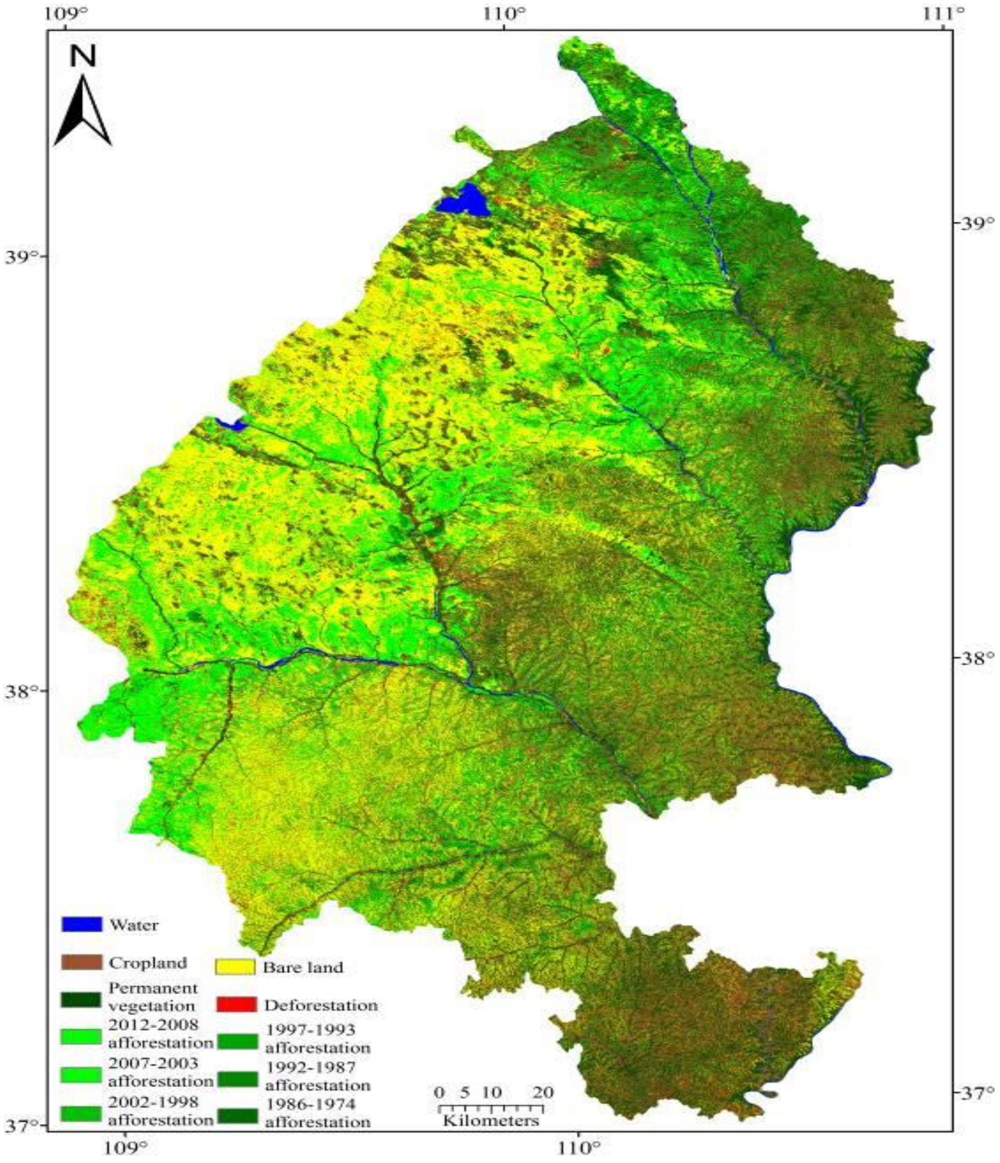

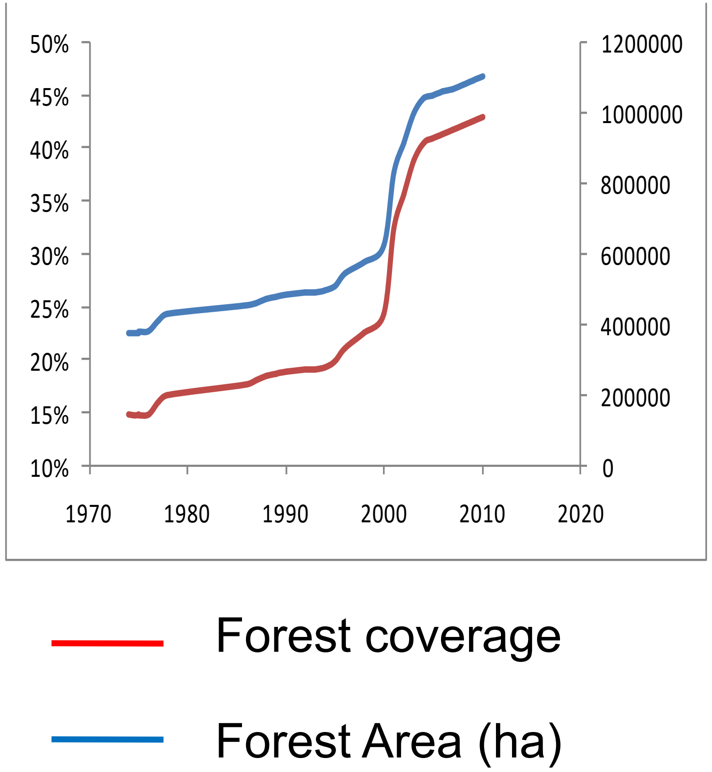

3. Forest disturbance monitoring and biomass mapping

Forest disturbance results

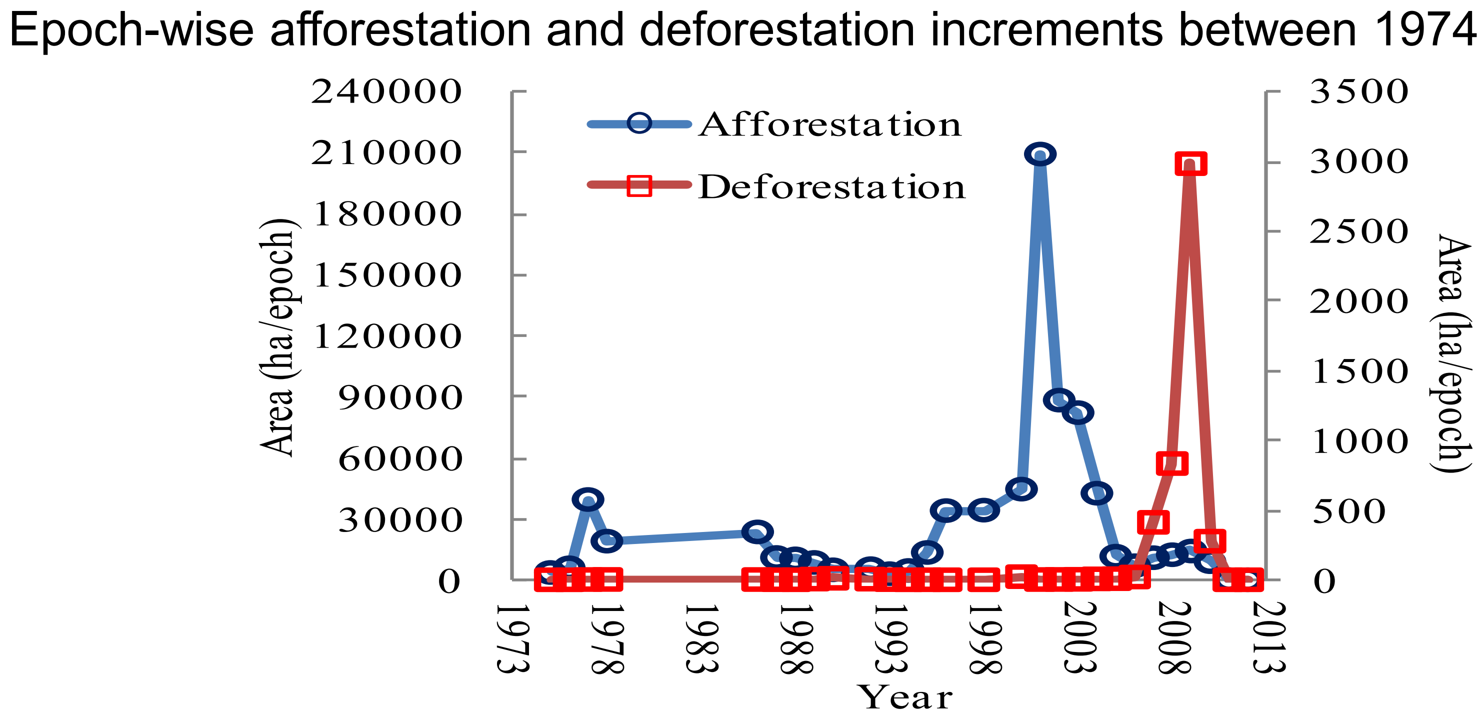

These two afforestation peaks agree with the start of TNSFP in 1978, and another strong political promotion of afforestation after 2000, through an initiative proposed by Premier Zhu Rongji in 1999 called "Returning cultivated land to forest and mountain greening". There was also a small peak of deforestation in 2009, clearly visible in the plots, which was caused by basic infrastructure construction projects (such as road construction, city and airport development, mining industry, etc.) promoted by the government after the global economic crisis in 2008.

3. Forest disturbance monitoring and biomass mapping

Collection of validation data

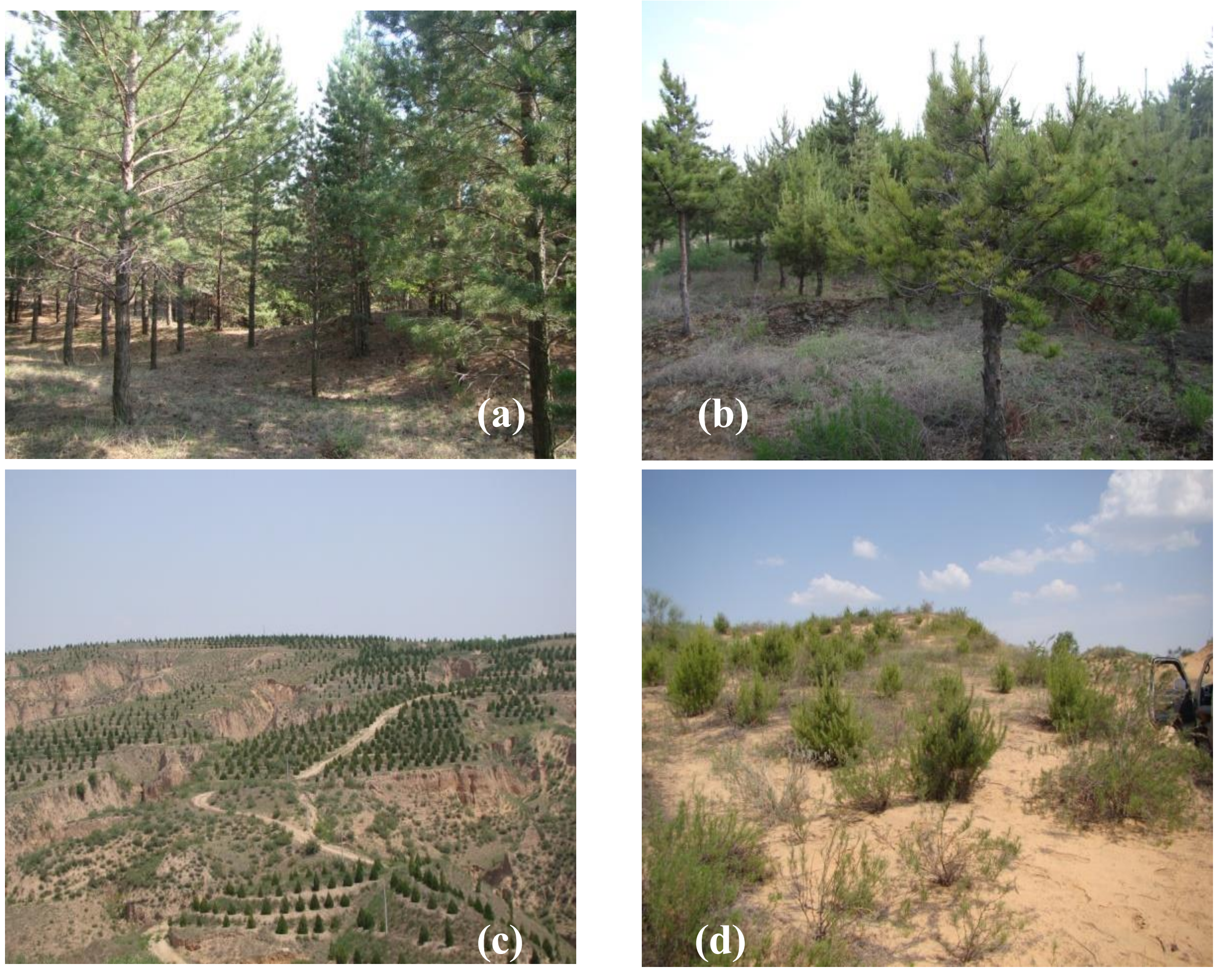

27 sites investigated for validation of forest changes forest types, Age Density, Height in 2012 and 2013

Photos of different afforestation sites in the Yulin district: (a) afforestation of Scots pine in 1980; (b) afforestation of Chinese pine in 1980; (c) afforestation of Sabina vulgaris in 2003; (d) afforestation of Chinese pine in 2004

3. Forest disturbance monitoring and biomass mapping

Accuracy validation

Confusion matrix for the six class land cover and forest change mapping.

	Bare land	Cropland	Water	Afforestation	Persisting forest	Deforestation	Total
Bare land	1302			76			**1378**
Cropland		500		64	19	31	**614**
Water			306				**306**
Afforestation	35	55		877	31		**998**
Persisting forest		35		101	585	6	**727**
Deforestation						116	**116**
Total	1337	590	306	1118	635	153	**4139**

Overall accuracy 89.1%, Kappa coefficient= 0.858.

3. Forest disturbance monitoring and biomass mapping

Accuracy validation

Table 5. Validation results for the land cover and forest change mapping (pixel counts).

Class	Bare land	Crop land	Water	2004 S1	2003 S2	2003 S3	2002 S1	1985 S1	1982 S1	1980 S2	1981 S1	1980 S4	1980 S1	1975 S2	1965 S1	Persisting Forest	D2009 S1	Total
Bare land	1302			15	5	2	54											1378
Cropland		500				48	10				1		5		4	15	31	614
Water			306															306
2010	9																	9
2009	16																	16
2008	4						2											6
2007	1						4											5
2006	2	1		1			9											13
2005				16			25											41
2004	3	8		5		4	115											135
2003		3		1	4	41	64											113
2002		1			1	46	26	1										75
2001						71	20	3	1	1								96
2000		3				3	1	1								1		9
1998						2	1											3
1996						1	1		1					1		4		8
1995							1	1								1		3
1994		7																7
1993		1																1
1992										1								1
1990		2							2	1								5
1989		6					1	5	1	4			1			4		22
1988		1					3	7	5	4	2	7				11		40
1987		1					2	7	1	5	2	8		1				27
1986		16					2	70	14	45	8	7	1	19		5		187
1978		3					1	37	5	30	11		8	16		2		113
1977		2						11	2	23	9		8	5		3		63
Persisting Forest		35				3		43	3	29	7		10	6	26	559	6	727
D2009																	116	116
Total	1337	590	306	38	10	221	342	186	35	143	40	22	33	48	30	605	153	4139

3. Forest disturbance monitoring and biomass mapping

Accuracy validation

The forest afforestation age information retrieved by the Landsat time series images was significantly related to measured plot tree age, with a determination coefficient (R^2) of 0.824, and a RMSE of 4.32 years.

Temporal detection accuracy of forest changes (epoch difference).

	0	<=1	<=2	<=3	<=5
Percent	22.2%	57.8%	73.6%	86.5%	97.4%

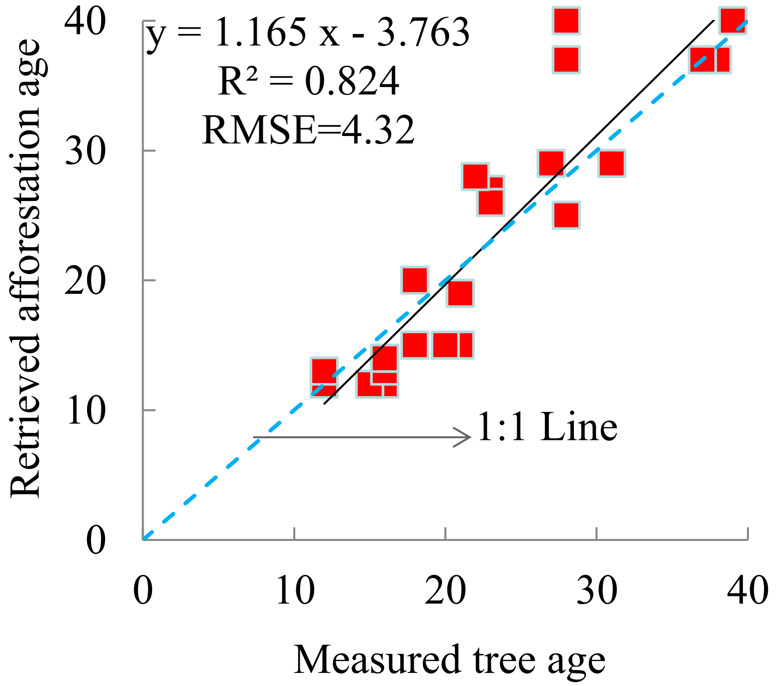

3. Forest disturbance monitoring and biomass mapping

Forest biomass modeling using field data

In 2012, We measured: **Diameter** (at 10, 30, 50, and 130 cm height),**Tree height**, **Tree age, Fresh weight and water content** (for stems, branches, leaves, coarse and fine roots) for Poplar tree, Chinese Scholar, Chinese pine.

3. Forest disturbance monitoring and biomass mapping

Forest biomass modeling using field data

Relationship between above ground biomass (AGB) and diameter, four species together (PopulussimoniiCarr, poplar tree, Chinese pine, and Pinus sylvestris)， and **the power function** curves was observed

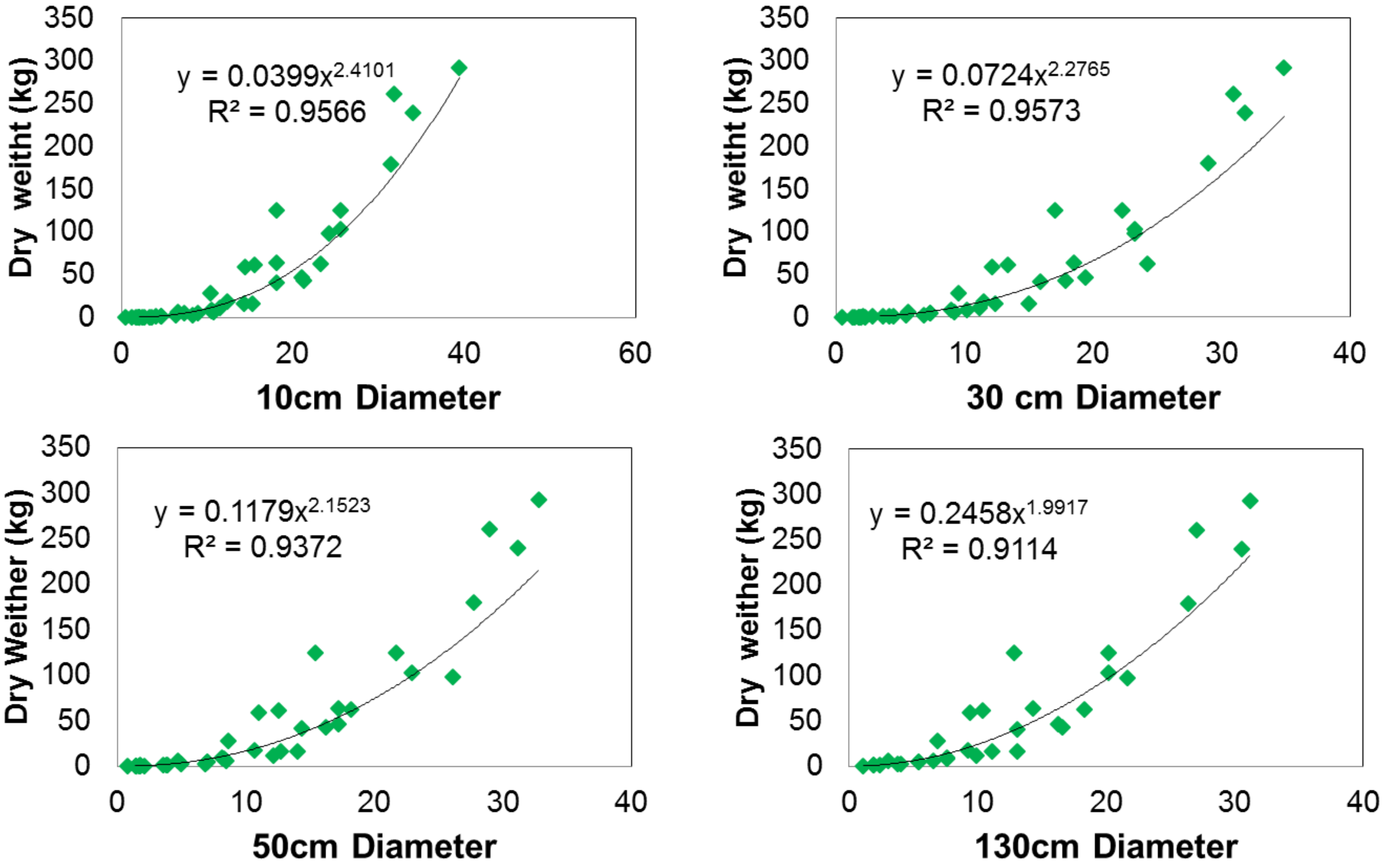

3. Forest disturbance monitoring and biomass mapping

Forest biomass modeling based on empirical model

A summary of regression analysis results in the western Brazilian Amazon

Variables	Models	R^2
Spectral signature	$AGB_{SF} = 667.72 - 13.92 \times f_{b4}$	0.75
	$AGB_{MF} = 1024.14 - 54.96 \times f_{b5}$	0.16
Texture	$AGB_{SF} = 164.62 - 2.27 \times f_{var}$	0.23
	$AGB_{MF} = 134.57 + 19.29 \times f_{con}$	0.39
Combination	$AGB_{SF} = 480.82 - 8.06 \times f_{b4} - 0.98 \times f_{var}$	0.76
	$AGB_{MF} = 753.31 - 43.21 \times f_{b5} + 17.89 \times f_{con}$	0.50

1) spectral signature led to much better estimation performance than textural images for secondary forest, but the result was inverse for mature forest;
2) Neither spectral signatures nor textural images could effectively estimate mature forest biomass;
3) A combination of spectral signature and textural images slightly improved secondary forest biomass estimation performance, but the improvement was considerable for mature forest biomass estimation.

Dengsheng Lu et al., “Aboveground Forest Biomass Estimation with Landsat and LiDAR Data and Uncertainty Analysis of the Estimates,” International Journal of Forestry Research, 2012. doi:10.1155/2012/436537

3. Forest disturbance monitoring and biomass mapping

The proposed model for biomass mapping

Biomass=f_1(species, soil, water available, climate variables, age)

NDVI=f_2(coverage)

Tree Biomass≈f_3(Tree age)

Plot Biomass ≈ *linear*(NDVI×exp(age))

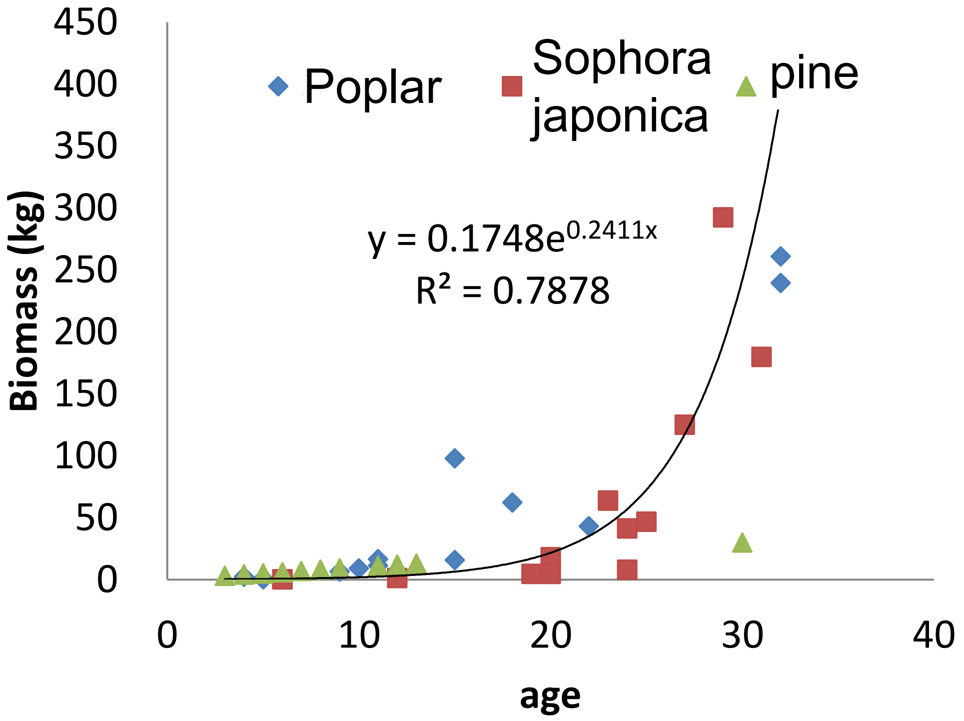

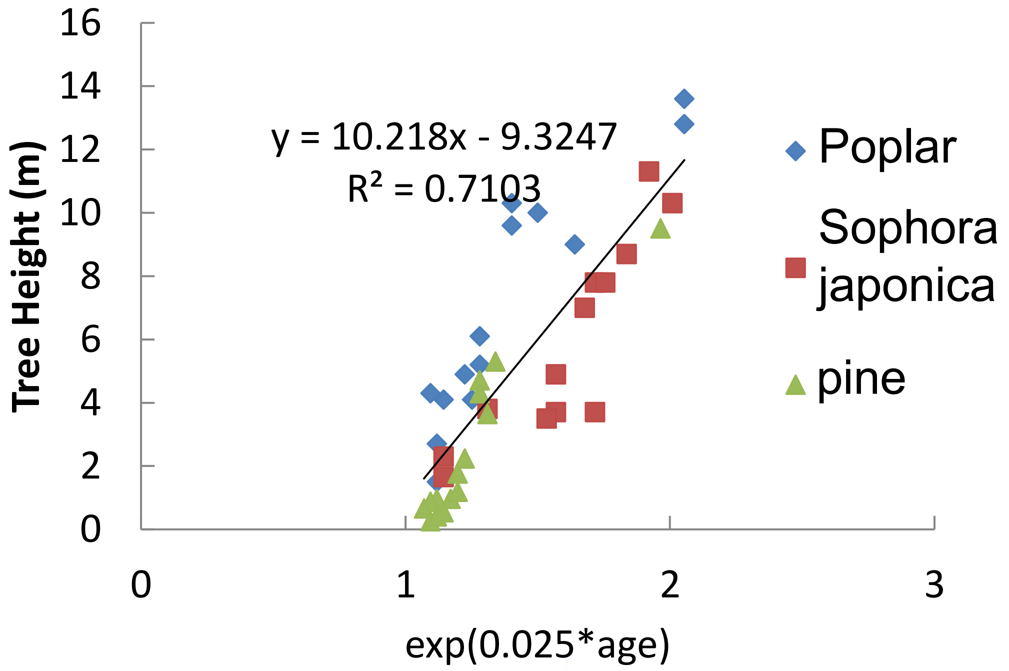

3. Forest disturbance monitoring and biomass mapping

The comparison between proposed model and VI-based model

$$AGB\ density = 9.4574 \times SR \times [\exp(treeage \times 0.0225)] - 17.021$$

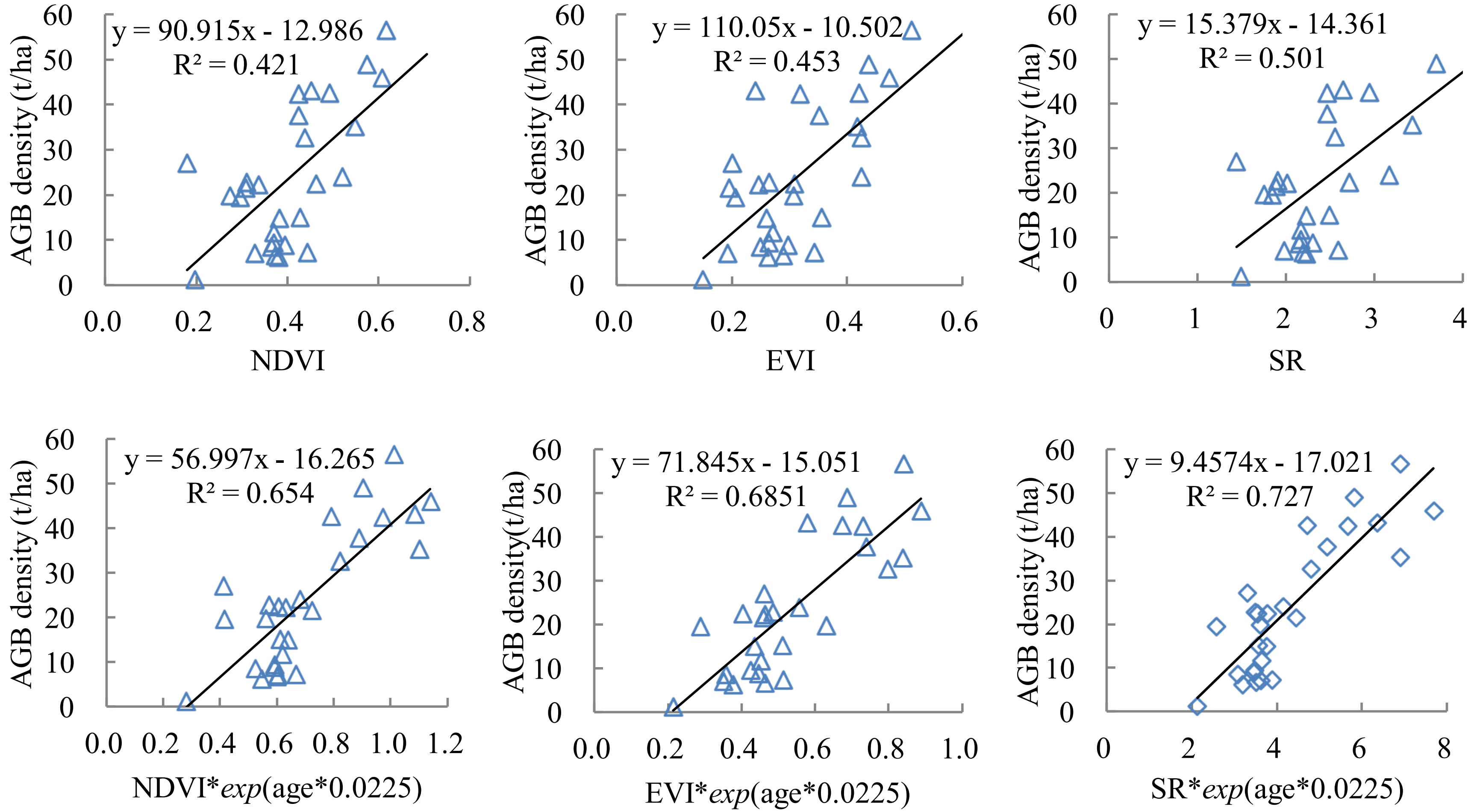

Figure 5. Regional AGB estimation models based on vegetation indices and measured tree age

3. Forest disturbance monitoring and biomass mapping

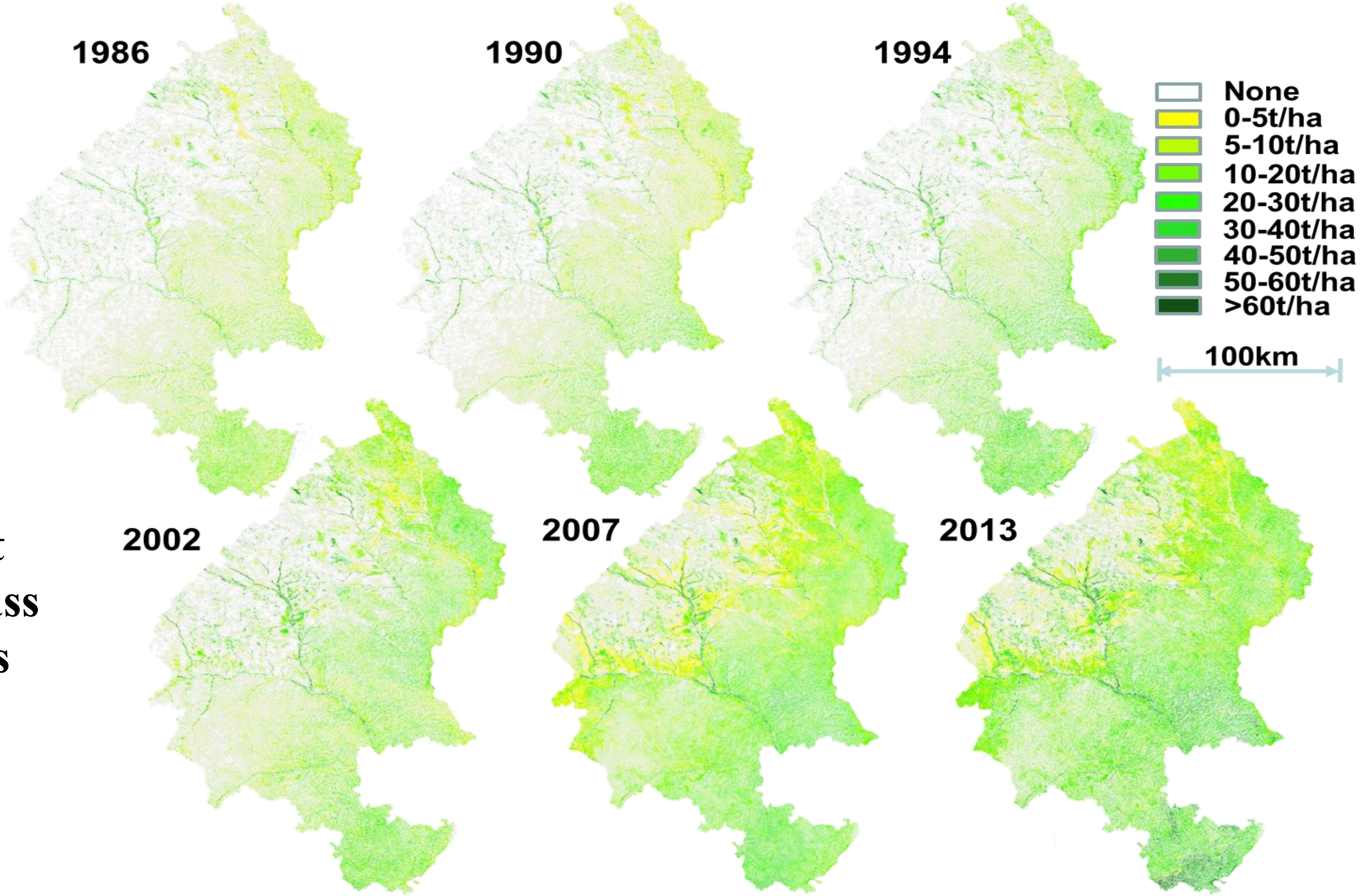

Forest biomass results

3. Forest disturbance monitoring and biomass mapping

Accuracy validation

Statistics of forest AGB and forest area in six counties of Yulin District at different years.

Year	Biomass[1] (t/ha)	Biomass[2] (t/ha)	Biomass[3] (G kg)	Area (km^2)
1986	14.35	15.72	5.8	4,048
1990	17.92	19.30	8.0	4,453
1994	22.95	24.84	10.6	4,617
2002	18.42	26.47	12.3	6,652
2003	17.84	25.30	14.1	7,897
2007	18.25	37.53	17.7	9,704
2011	20.22	39.46	21.9	10,831
2013	24.60	44.53	26.6	10,831

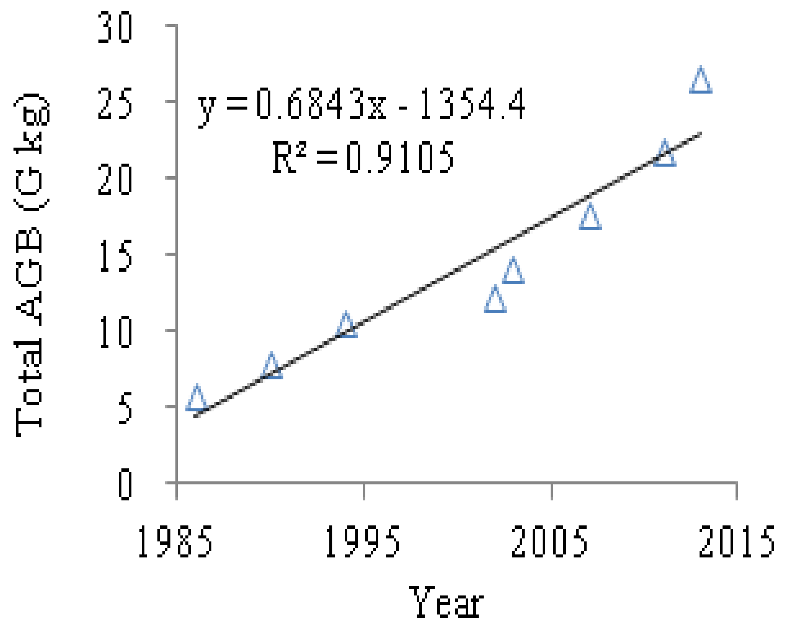

Biomass[1] and Biomass[2] are the mean AGB density for total forest area and persisting forest area, respectively; Biomass[3] is the total forest AGB ; Area stands for total forest area in six counties Yulin District.

3. Forest disturbance monitoring and biomass mapping

Accuracy validation

For the forest area, including persisting forest and subsequently planted forest, has experienced an annual AGB growth rate of about 1 t/ha over the last four decades.

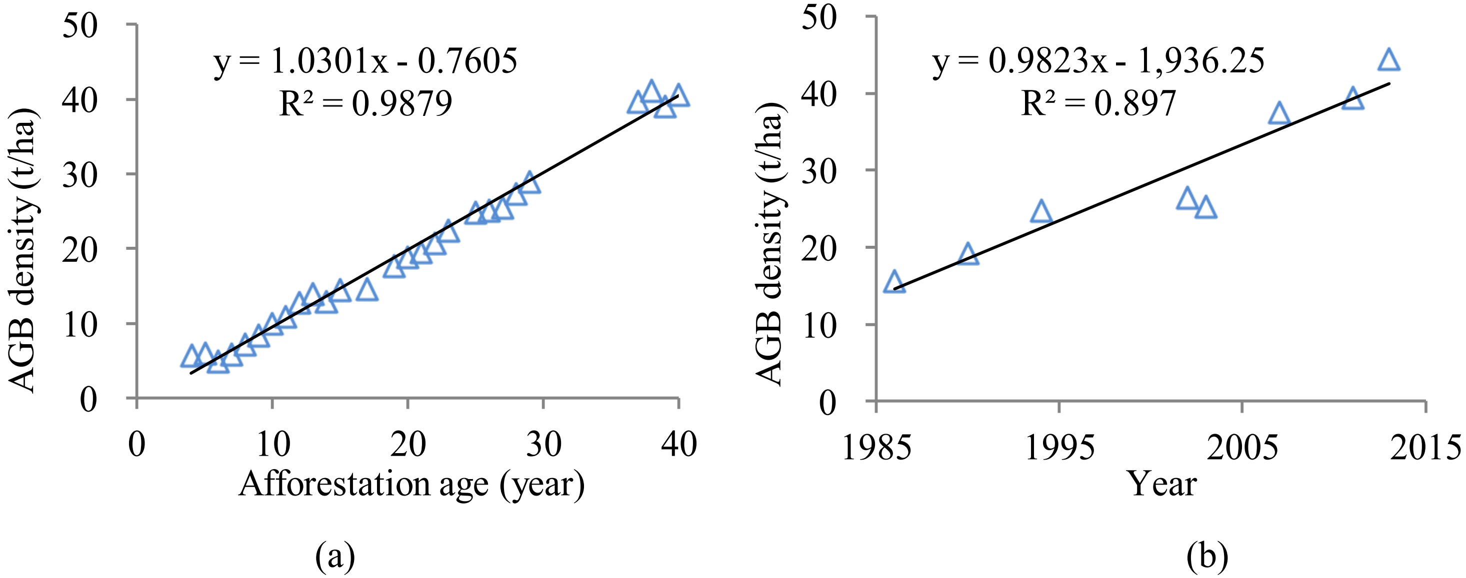

Figure 8. (a) Mean AGB density of forest at different ages in Yulin District in the last 40 years. (b) Increasing trend in mean AGB density for persistent forest in Yulin District from 1985 to 2013.

3. Forest disturbance monitoring and biomass mapping

Summary

- The afforestation age can be retrieved from the Landsat time-series stacks in last forty years (from 1974 to 2013), which was consistent with the surveyed tree ages, with a RMSE value of 4.32 years and a determination coefficient (R^2) of 0.824.

- The AGB models were successfully developed by integrating vegetation indices and tree age, which was significantly improved using the combination of SR and tree age, with a R^2 value from 0.50 to 0.727.

- We confirmed a great achievement of the ecological revegetation projects in Yulin district over the last 40 years. It clearly showed a big forest increase in Yulin district from 340,890 ha (13.2% of total district area) in 1974 to 1124,648 ha (43.8%) in 2012.The total forest AGB in Yulin district has increased by 20.8 G kg, from 5.8 G kg in 1986 to 26.6 G kg in 2013, with a total increase of 360%.

- The results also present a noticeable carbon increment for the planted artificial forest in Yulin district over the last four decades, with a AGB increase of 1t/ha/year.

Contents

The overview of land-cover mapping methodology

Generally, there are three classification strategies to land-cover mapping.

We proposed a novel and automatic approach, called the SPatial-tEmporal speCtral Library (SPECLib), which aims to produce a land cover map with a 30-m spatial resolution at global or regional scale.

	Manual	**Semi-automatic**	**Automatic**
Method	visual interpretation	supervised classification	Prior knowledge, Spectral library
Features	**Texture, color, brightness etc**	**Spectral signatures from training samples**	**Spectral signatures from prior library**
advantages	Accurately determine each parcel using expert knowledge	Determine each pixel using training samples Maybe accurate	Determine each pixel using reference spectra
examples	National Land Use/Cover Database of China (Zhang et al. 2014)	FROM-GLC (Gong et al., 2013)	**GLC_FCS30 (Zhang et al., 2021)**
	GloberLand30 (Chen et al., 2015)		

The fine classification system in GLC_FCS30 (containing 35 land-cover subcategories)

Globland30	LCCS Classification System	Fine Classification System
Cropland	Rain-fed cropland	Rain-fed cropland
		Herbaceous cover
		Tree or shrub cover (orchard)
	Irrigated cropland	Irrigated cropland
Forest	Evergreen broadleaved forest	Evergreen broadleaved forest
	Deciduous broadleaved forest	Deciduous broadleaved forest
		Closed deciduous broadleaved forest
		Open deciduous broadleaved forest
	Evergreen needleaved forest	Evergreen needleleaved forest
		Closed evergreen needleleaved forest
		Open evergreen needleleaved forest
	Deciduous needleaved forest	Deciduous needleleaved forest
		Closed deciduous needleleaved forest
		Open deciduous needleleaved forest
	Mixed forest	Mixed-leaf forest
Shrubland	Shrubland	Shrubland
		Evergreen shrubland
		Deciduous shrubland
Grassland	Grassland	Grassland

Globland30	LCCS Classification System	Fine Classification System
Wetland	Wetlands	Mangrove
		Salt marsh
		Tidal flat
		Swamp
		Marsh
		Flooded flat
		Saline
Impervious surfaces	Impervious surfaces	Impervious surfaces
Tunda	Lichens and mosses	Lichens and mosses
Bare land	Sparse vegetation	Sparse vegetation
		Sparse shrubland
		Sparse herbaceous cover
	Bare areas	Bare areas
		Consolidated bare areas
		Unconsolidated bare areas
Water body	Water body	Water body
Permanent snow/ice	Permanent snow/ice	Permanent ice and snow

The overview of GSPECLib (Global land-cover Spectral Library)

The GSPECLib has been developed using MCD43A4 and CCI_LC2015. The geographical cell of GSPECLib was set as 1.43° × 1.43° equaling the size of second-level land grid and with a temporal resolution of 8 days. The GSPECLib has exceeding 300 million spectral data.

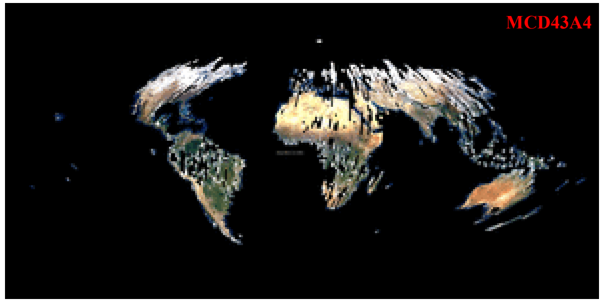

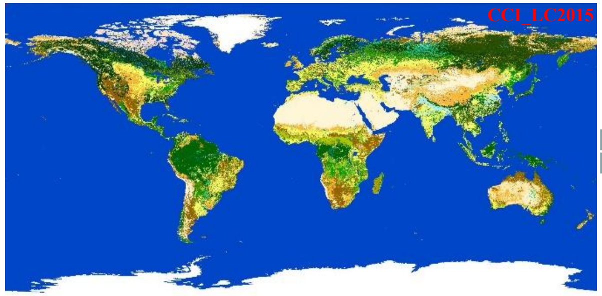

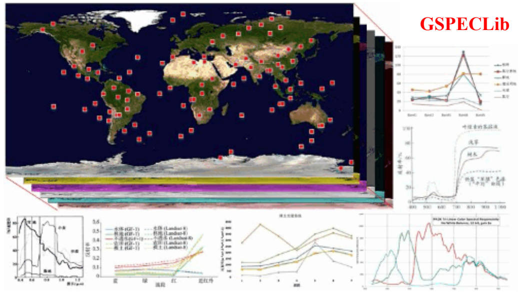

The number of reflectance spectra in each GSPECLib geographical cell

The number of land-cover types in each GSPECLib geographical cell

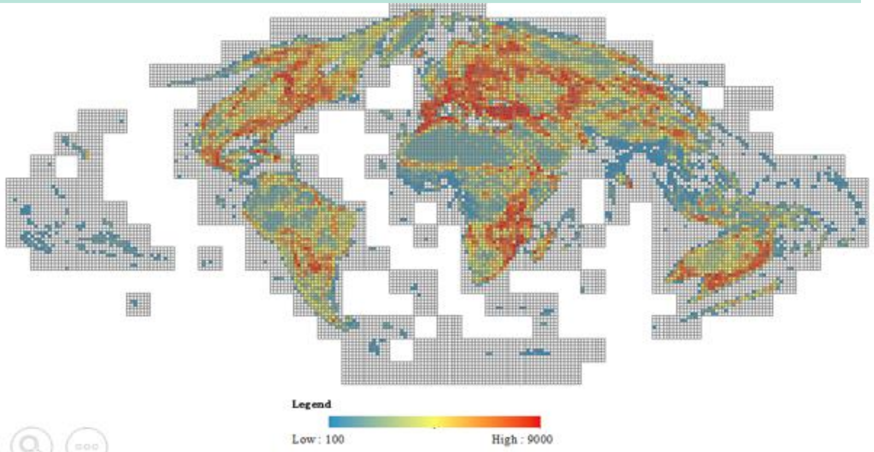

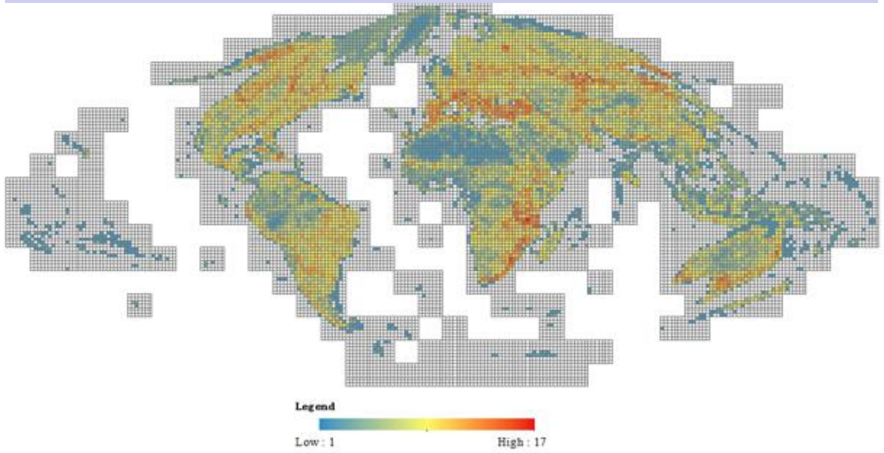

The overview of GSPECLib (Global land-cover Spectral Library)

Due to the cloud coverage, spectral similarity of vegetation-related types, **the single-date Landsat image** is usually not able to provide sufficient features to accurately classify all land-cover types (such as: deciduous forest and evergreen forest).

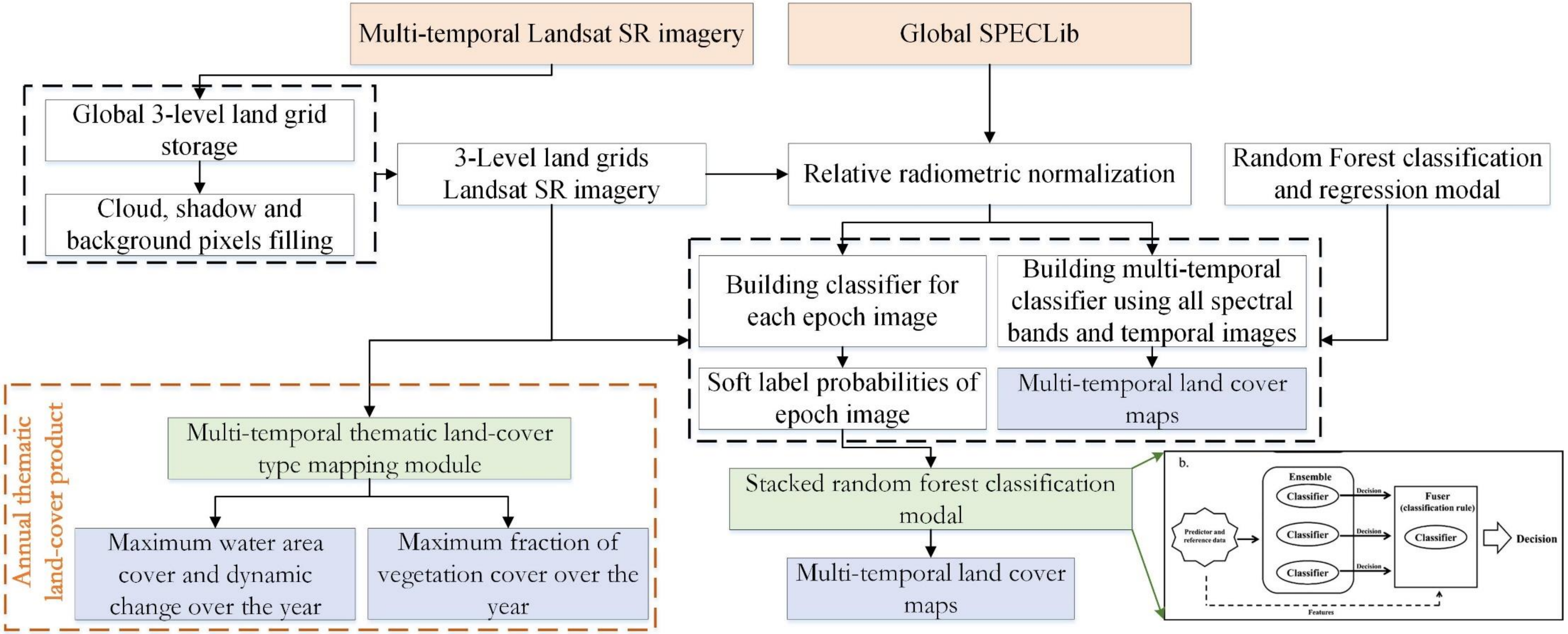

Global impervious surface mapping from multisourced remote sensing observations

- Although the independent optical imagery have been successfully employed for regional or global impervious mapping, accurate estimation of impervious surfaces remains challenging due to the diversity of urban land covers, leading to difficulties of separating different land covers with similar spectral signatures;
- As the optical imagery only capture the surface reflectance characteristics, while the synthetic aperture radar (SAR) data images could provide the structure and dielectric properties of the surface materials, the incorporation of multi-source and multi-temporal remote sensing imagery has been demonstrated to improve the impervious mapping accuracy

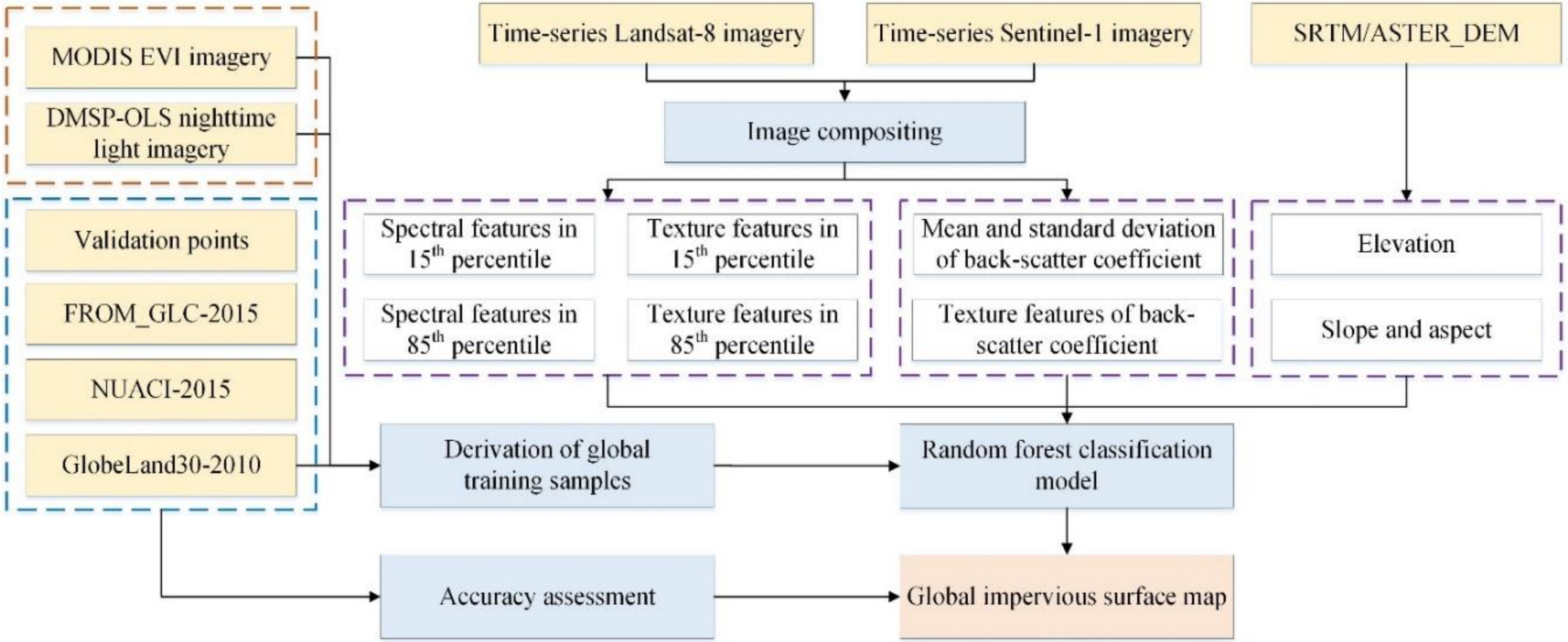

Global impervious surface mapping from multisourced remote sensing observations

SAR data and **multitemporal features** are important for accurate land cover mapping

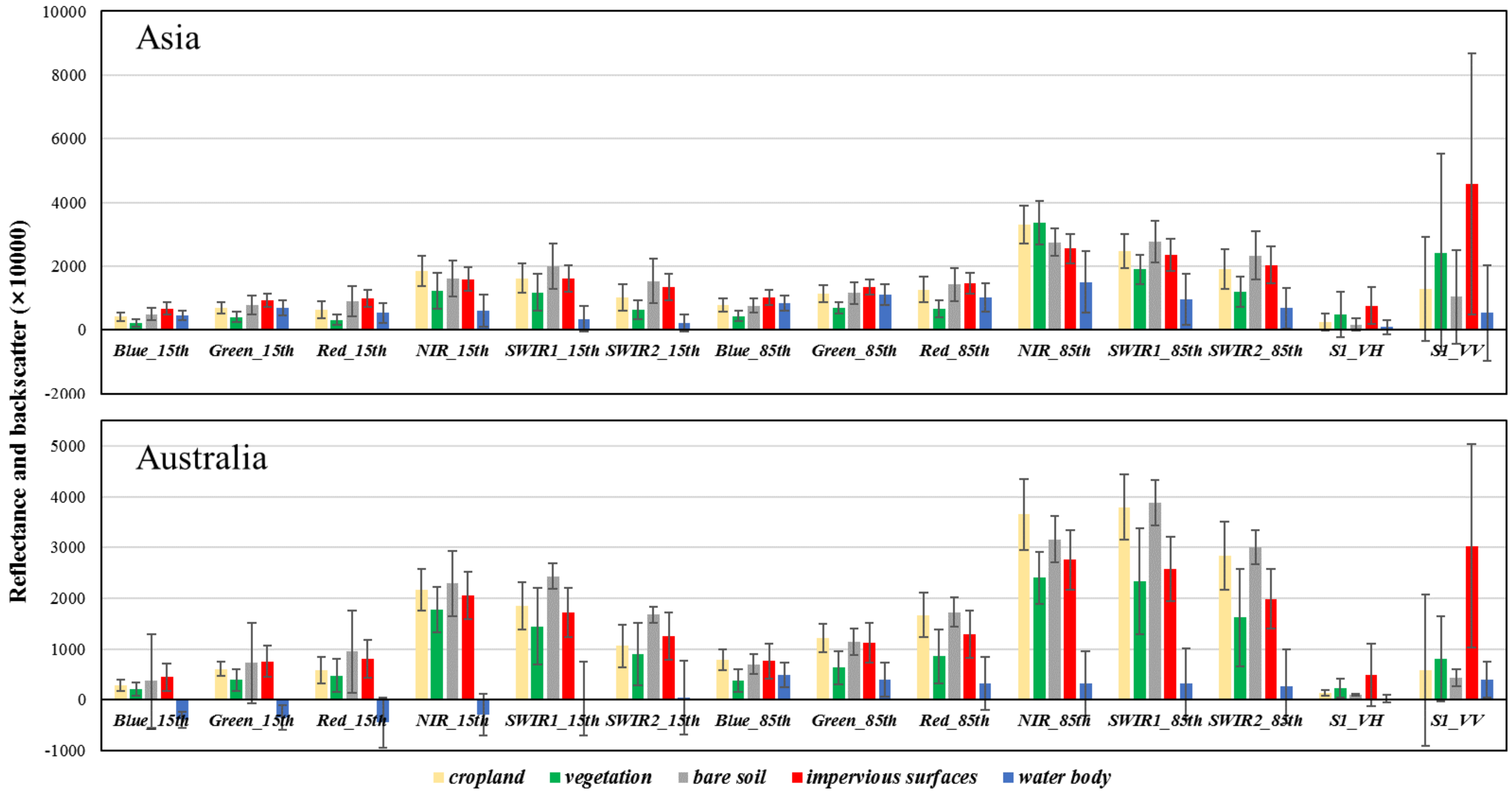

Global impervious surface mapping from multisourced remote sensing observations

Using multitemporal Landsat and Sentinel-1 imagery, our automated impervious surface mapping method was integrated on the Google Earth Engine platform and produced the accurate global 30 m impervious surface products. The results show that:

- impervious surfaces are mainly concentrated in three continents: Asia (34.43 %), North America (28.04 %) and Europe (24.98 %), followed by South America (5.89 %), Africa (5.63 %) and Australia (1.06 %). In addition, the zonal statistics indicate that 70 % of the impervious surfaces are distributed between 30 ◦ N ~60◦ N.

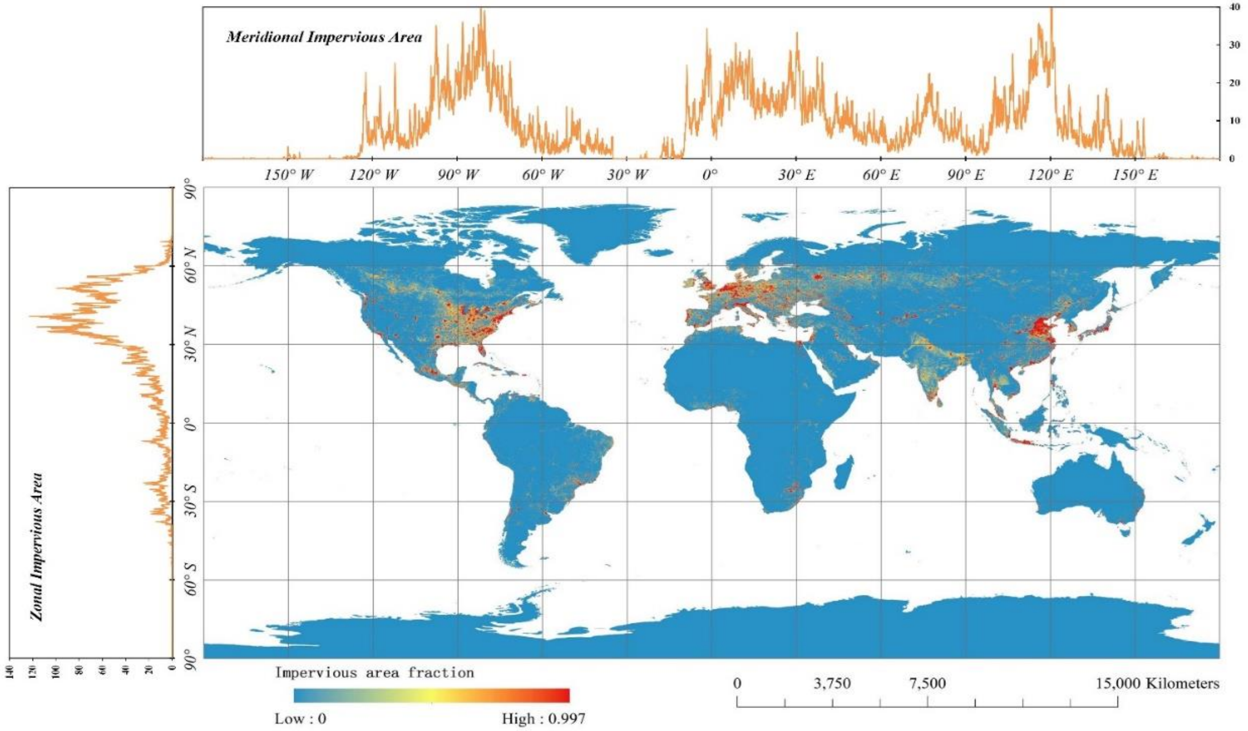

Global impervious surface mapping from multisourced remote sensing observations

The accuracy of 6 sets of 30-m impervious surface products was verified using 15 typical test areas randomly selected in the world (a total of 11942 verification points). The results show that the products generated in this study have the highest accuracy performance (OA=95.1%) , Kappa=0.898), followed by GHSL-2015, FROM_GLC-2015, GlobeLand30, HBASE-2010 and NUACI-2015.

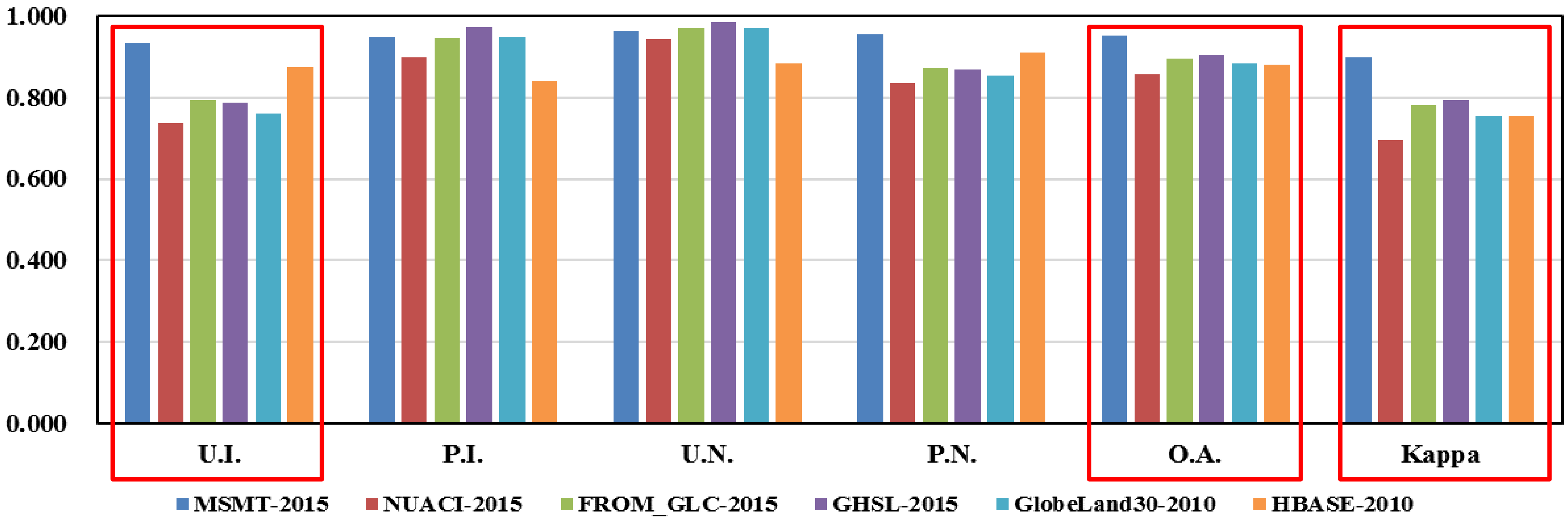

Zhang, X., Liu, L., et al. Development of a global 30-m impervious surface map using multi-source and multi-temporal remote sensing datasets with the Google Earth Engine platform, Earth Syst. Sci. Data, 12, 1625–1648, 2020

The overview of GLC_FCS30 land-cover dataset

Using time-series Landsat imagery during 2014-2016 and the **globally distributed training samples from GSPECLib**, we trained the **local adaptive classification model** at each 5°×5° geographical tile, and generate the first global land-cover products with fine classification system (**GLC_FCS30**) in 2015.

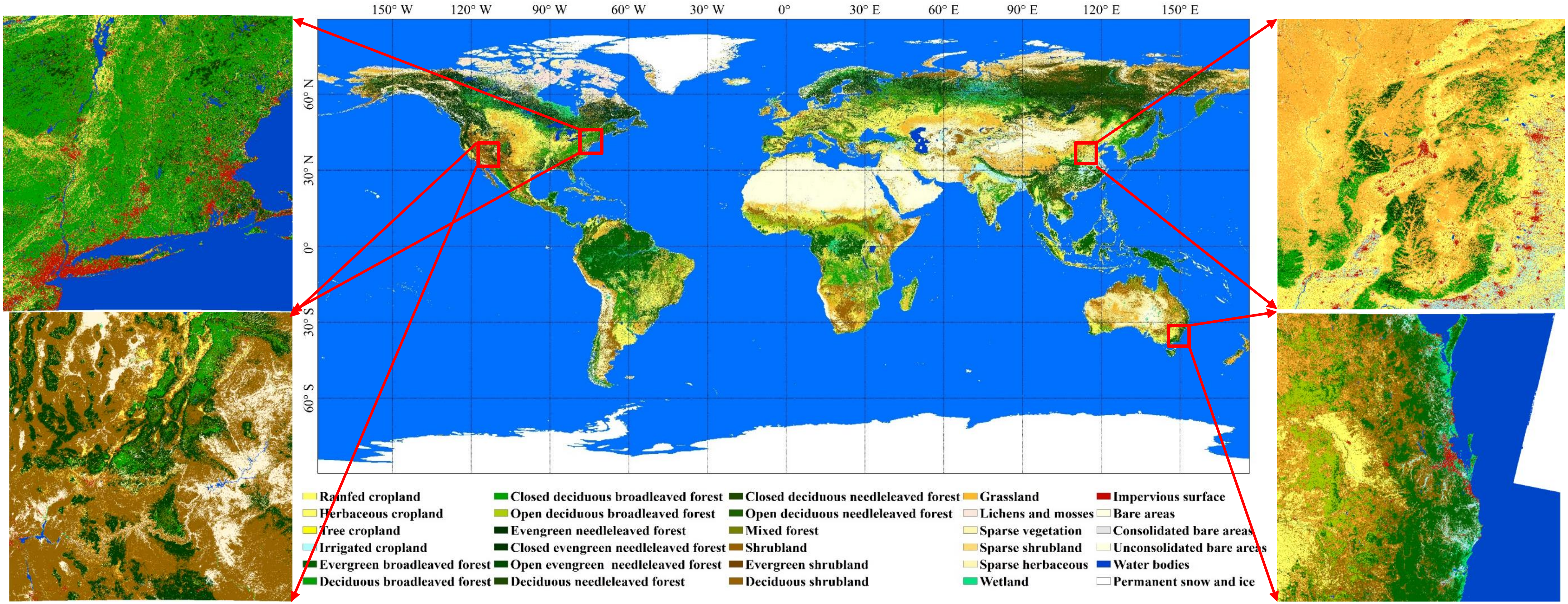

Quantitative accuracy assessment

Using the globally distributed 44503 validation points, which collected from multisourced and high-resolution remote sensing imagery, the GLC_FCS30 is validated to achieve **the overall accuracy of 82.5% and a kappa coefficient of 0.784** at **level-0 classification system**, and **overall accuracy of 71.4% and kappa coefficient of 0.686** at **level-1 classification system.**

	10	20	50	60	70	80	90	120	130	140	150	180	190	200	210	220	Total	P.A.
10	5305	86	32	281	12	1	4	163	146	0	47	10	66	23	5	0	6181	0.858
20	213	481	0	8	0	0	0	0	4	0	0	0	17	0	13	0	736	0.654
50	65	0	2830	152	82	0	28	17	1	0	0	47	0	0	0	0	3222	0.878
60	82	3	325	3010	175	58	189	99	28	0	10	44	1	1	2	0	4027	0.747
70	10	0	12	136	2469	34	133	15	7	1	10	192	1	2	3	0	3025	0.816
80	2	0	0	59	283	545	31	11	2	0	11	29	0	0	0	0	973	0.560
90	31	8	67	840	604	24	783	14	16	0	1	52	0	1	0	0	2441	0.321
120	402	42	64	395	57	39	20	3088	645	21	422	88	17	133	6	2	5441	0.568
130	183	14	9	94	47	7	19	430	3100	311	128	171	14	75	7	0	4609	0.673
140	0	0	0	1	13	12	0	35	39	93	83	5	0	12	0	0	293	0.317
150	47	8	0	75	0	3	0	254	218	147	1540	13	0	692	4	26	3027	0.509
180	64	14	12	12	22	8	2	24	23	12	17	585	15	43	89	4	946	0.618
190	38	14	1	1	4	1	1	9	12	0	5	5	384	7	2	0	484	0.793
200	94	1	0	2	3	0	0	114	163	14	415	72	3	4129	14	2	5026	0.822
210	33	15	3	4	57	17	4	13	7	49	28	32	3	15	1455	1	1736	0.838
220	0	0	2	6	6	0	2	8	66	2	13	2	0	74	47	1648	1876	0.878
Total	6569	686	3357	5076	3834	749	1216	4294	4477	650	2730	1347	521	5207	1647	1683	44043	
U.A.	0.808	0.701	0.843	0.593	0.644	0.728	0.644	0.719	0.692	0.143	0.564	0.434	0.737	0.793	0.883	0.979		
O.A.									0.714									
Kappa									0.686									

The cross-comparisons with several released land-cover products

- Compared with the **CCI_LC and MCD12Q1** (coarse resolution of 300 m and 500 m), our GLC_FCS30 shows great advantages in capturing these spatial details;
- Compared with **FROM_GLC and GlobeLand30**, the GLC_FCS30 outperforms with its greatly diverse over the classification system, it contains exceeding 30 land-cover types.

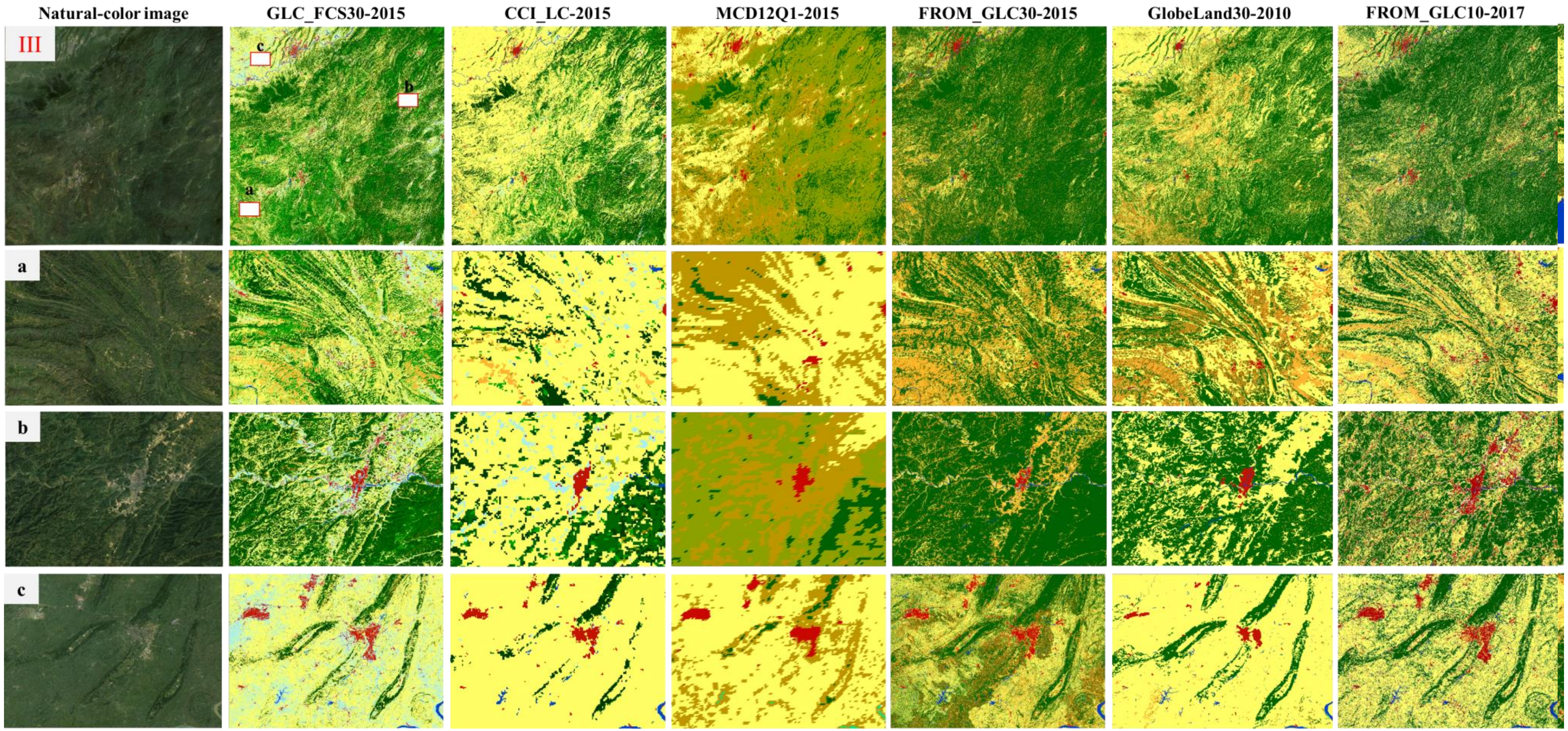

The third-party validation and comparison in the Indonesia

The research of high-precision land cover classification **in tropical rainforest area** is a challenge. **The results** of the **third-party** nationwide inspection in Indonesia show that **GLC_FCS30** not only has a **finer** classification system, but also has a **higher overall classification accuracy** (65.69%), which is better than the **Globeland30 (61.65%)** and **Tsinghua FROM_GLC2015 (57.71%)** of the National Basic Geographic Information Center.

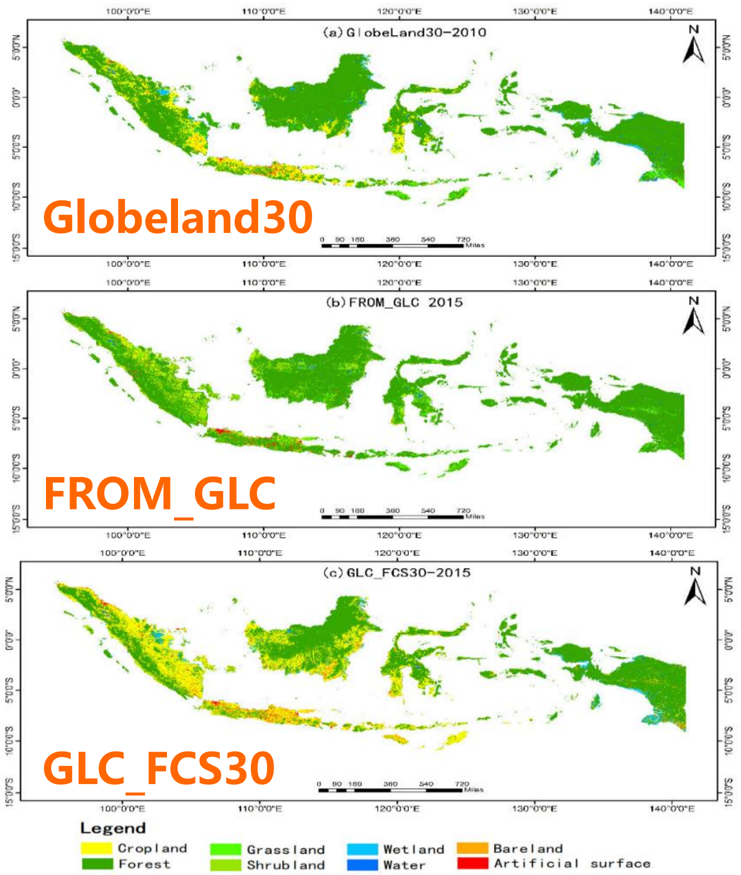

Distribution of Ground Cover Product Inspection Samples in Indonesia

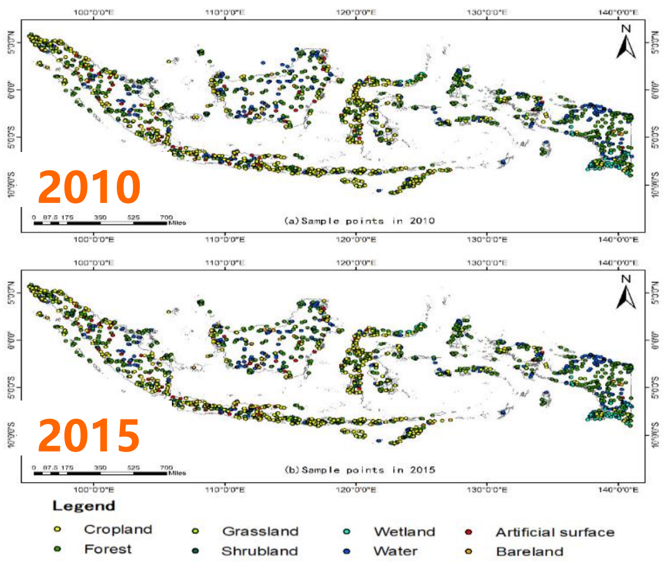

Kang, J. et al. **Consistency Analysis of Remote Sensing Land Cover Products in the Tropical Rainforest Climate Region: A Case Study of Indonesia**. *Remote Sens.* **2020**, *12*, 1410.

The GLC_FCS30 dataset during 1985-2020 with interval of 5-years

A global time-series 30 m land-cover product with a fine classification system (GLC_FCS30) was developed.

Using our GSPECLib-based land-cover classification algorithm and time-series Landsat imagery, which broke through the key technologies of automatic global land-cover mapping and developed a global land-cover product from 1985 to 2020—GLC_FCS30.

GLC_FCS30 product from 1985 to 2020

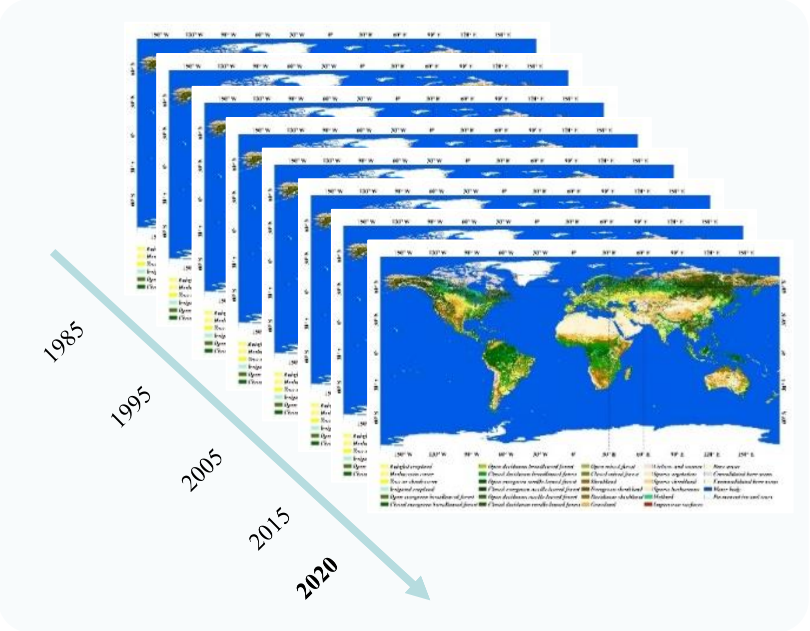

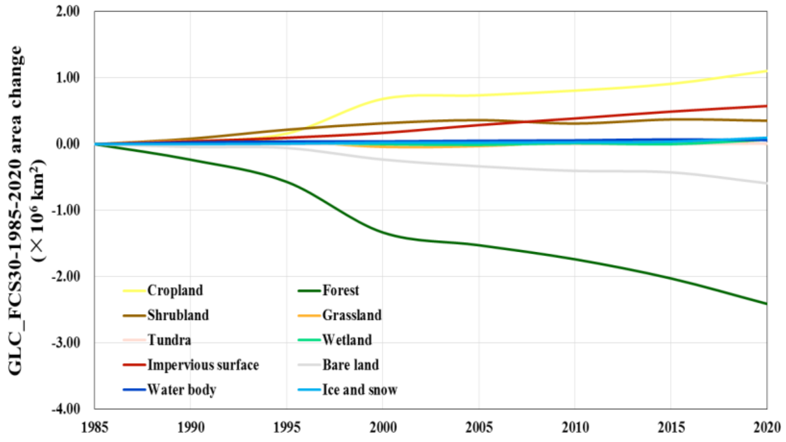

In the past 35 years, the global forest and shrubland area has decreased by 2.06 million km^2, cropland has increased by 1.1 million km^2, and impervious surface has increased by 0.58 million km^2 (an increase of 112.5%).

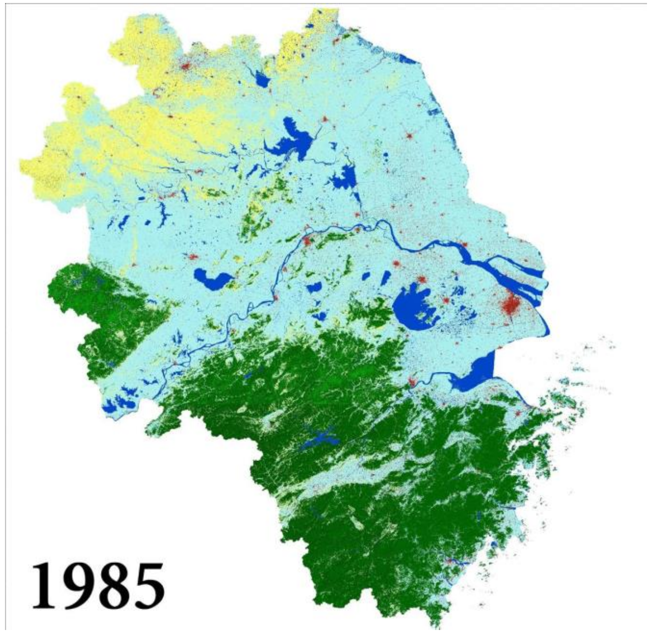

The impervious surface of the Yangtze River Delta increased by 4.8 times.

Contents

5. GLC_FCS30D: Global 30-m land-cover dynamic monitoring product

Most existing global land cover products adopt the strategy of independently classifying time-series products, which will introduce a large number of "**pseudo**" changes in related research on change detection, resulting in low classification accuracy.

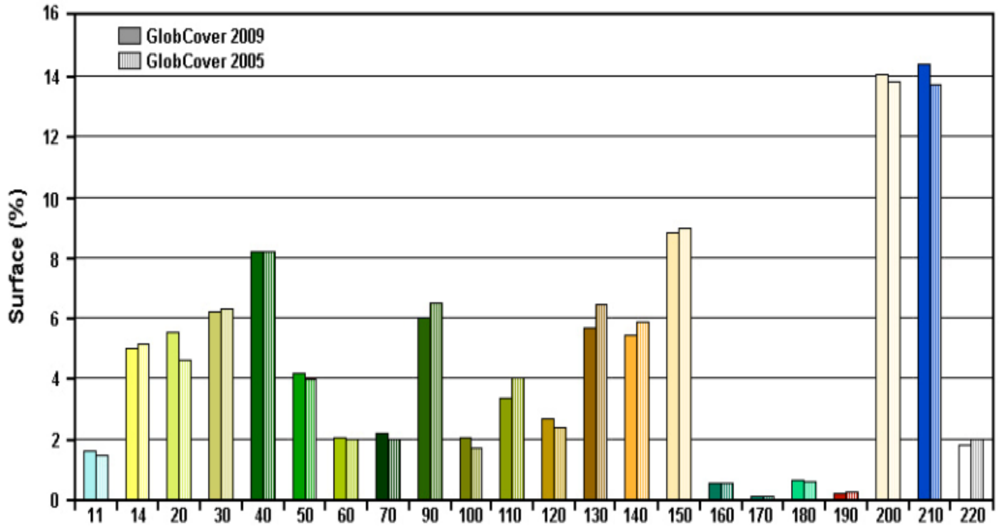

Comparison of classes proportions between GlobCover 2005 and 2009 land cover products

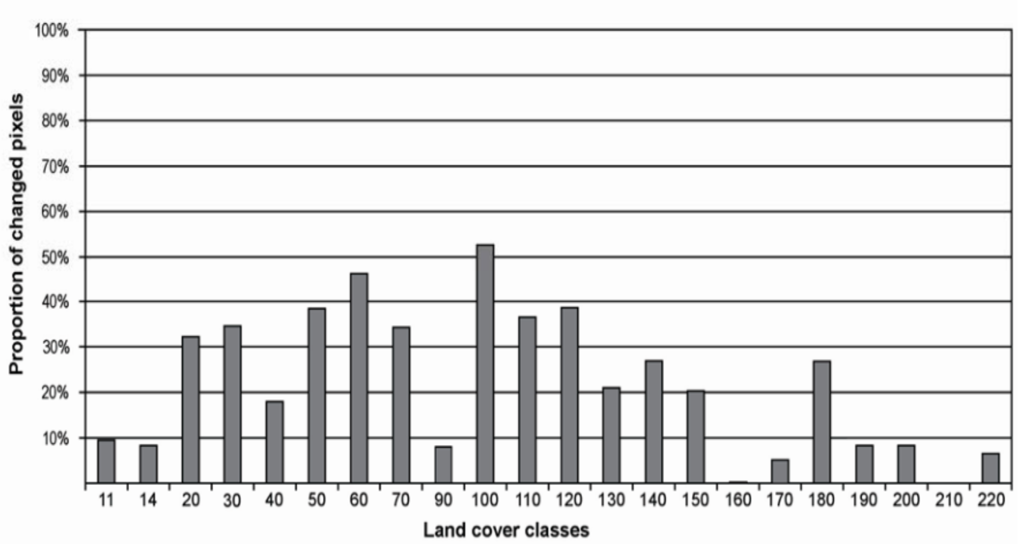

Proportion of pixels are not classified in the same manner between the two GlobCover maps

The proportions of various types in classification results of 2005 and 2009 are relatively consistent. However, **finally detected changed pixels far exceeded the real changes** (Bontemps et al., 2011).

The 2009 GlobCover product "**cannot be used for any change detection application**"–not even for "direct comparison with the previous GlobCover 2005 product"(Bontemps et al., 2011)

5. GLC_FCS30D: Global 30-m land-cover dynamic monitoring product

Existing land-cover products are insufficient to support land-cover change analysis!

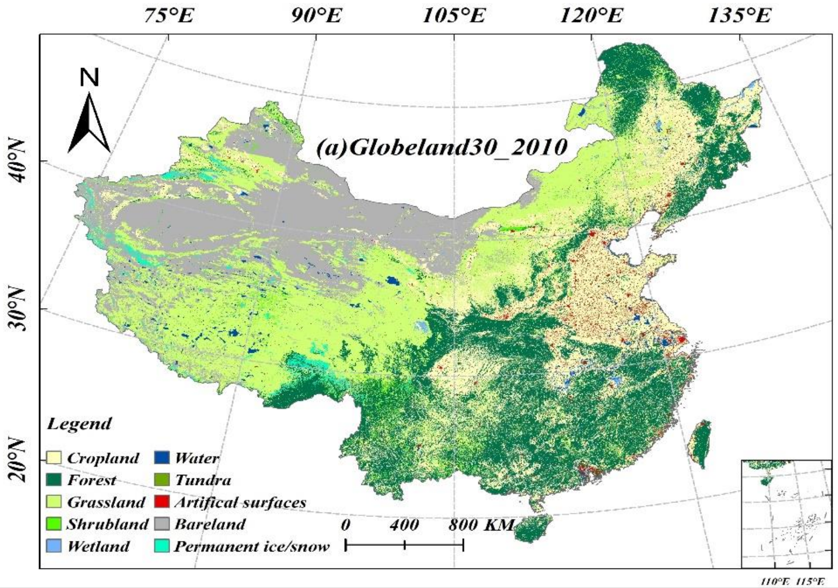

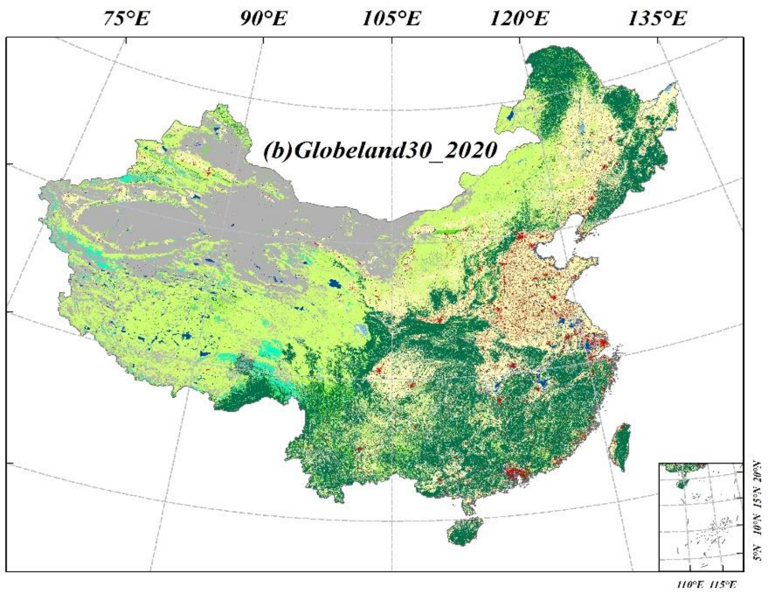

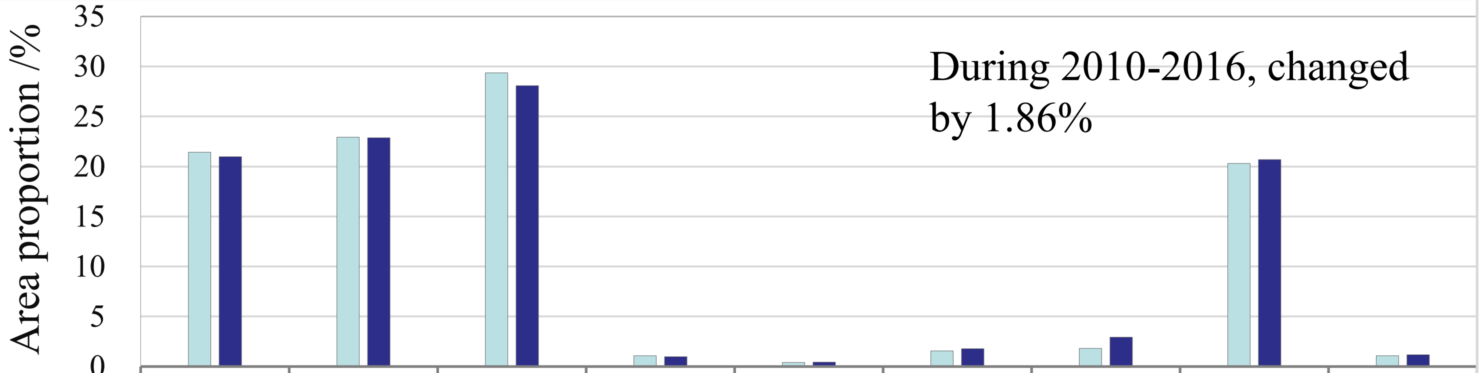

	cropland	forest	grassland	shrubland	wetland	water	Artifical	bareland	permanent
GlobeLand30_2010	21.42	22.94	29.35	1.07	0.42	1.57	1.82	20.31	1.09
GlobeLand30_2020	20.99	22.86	28.09	0.99	0.45	1.8	2.94	20.69	1.19

Land-cover change proportion at different scales:

- national scale: 1.86%;
- provincial scale: 2.77%;
- 1 km scale: 6.95%;
- 30 m scale: 10.6%

Mi, J., Liu, L., Zhang, X., Chen, X., Gao, Y., & Xie, S. (2022). Impact of geometric misregistration in GlobeLand30 on land-cover change analysis, a case study in China. Journal of Applied Remote Sensing, 16(1), 014516.

5. GLC_FCS30D: Global 30-m land-cover dynamic monitoring product

Time-series change detection and dynamic update products are expected to provide precise and accurate understanding of global land cover changes.

	Visual interpretation	Period by period classification	Change detection and dynamic update
Method	**Human-computer interaction + Visual interpretation**	**Multi-period training samples + Supervised classification**	**Time-series change detection +Machine learning**
Fundamental	Use visual interpretation to compare differences between reference data and data to be processed.	Select high-confidence training samples period by period; Classify each epoch independently using a supervised classification model.	Use change detection model to detect and extract changed pixels; Train a classification model using stable pixels to update the changed pixels.
Advantage	Make full use of expert prior knowledge and image features (such as spectral and texture).	High monitoring efficiency; data time consistency isn't considered.	Better temporal continuity; less human intervention; high automation.
Disadvantage	Low efficiency; Larger manpower and material resources needed; high subjectivity	Period-by-period training sample selection requires a large manpower and material resources; the accumulation of period-by-period classification errors leads to greater uncertainty.	Dynamic monitoring has a low efficiency, a huge amount of calculations, a number of input data and a complex quantitative processing.
Datasets	**1:100,000 China land use and cover dataset**	**FROM-GLC GLC_FCS30** →	**GLC_FCS30D**
	GlobeLand30		

5. GLC_FCS30D: Global 30-m land-cover dynamic monitoring product

Time-series land-cover change detection and classification algorithm

$$\hat{\rho}(i,x) = a_{0,i} + \sum_{k=1}^{n}\left(a_{k,i}cos\left(\frac{2k\pi}{T}x\right) + b_{k,i}sin\left(\frac{2k\pi}{T}x\right)\right) + c_{1,i}x$$

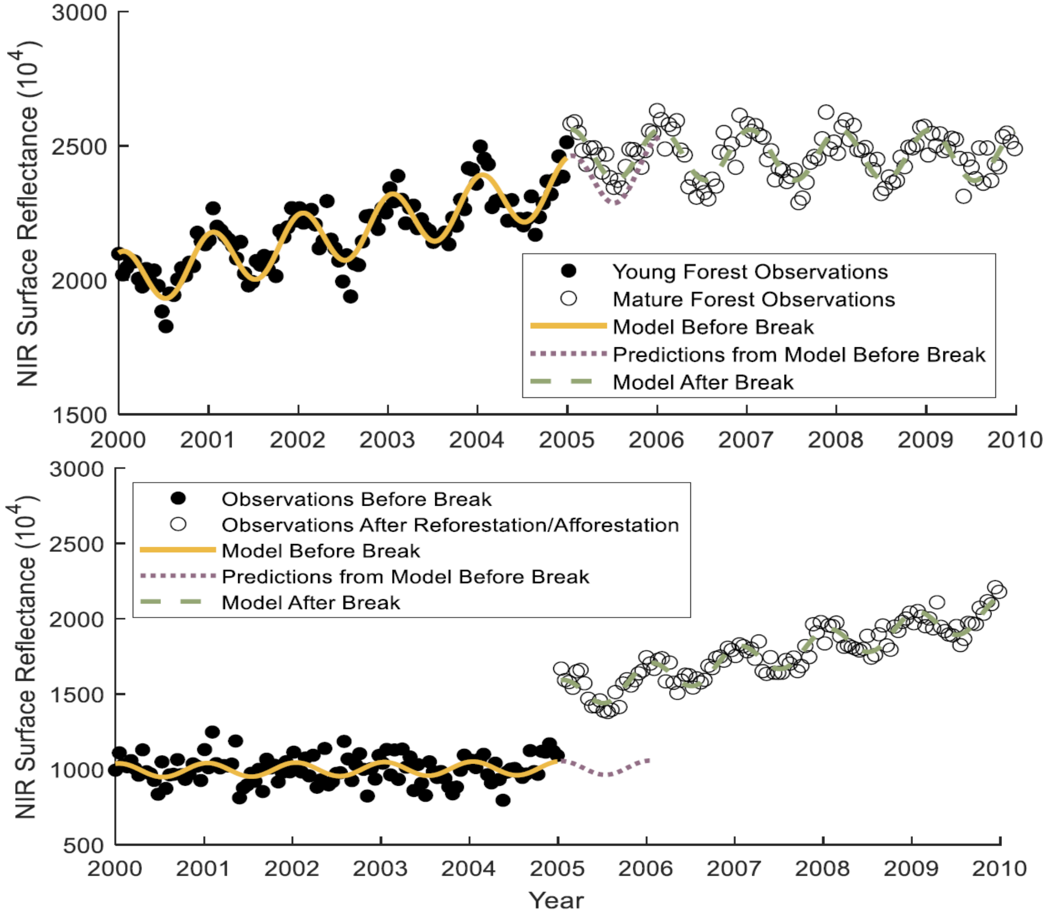

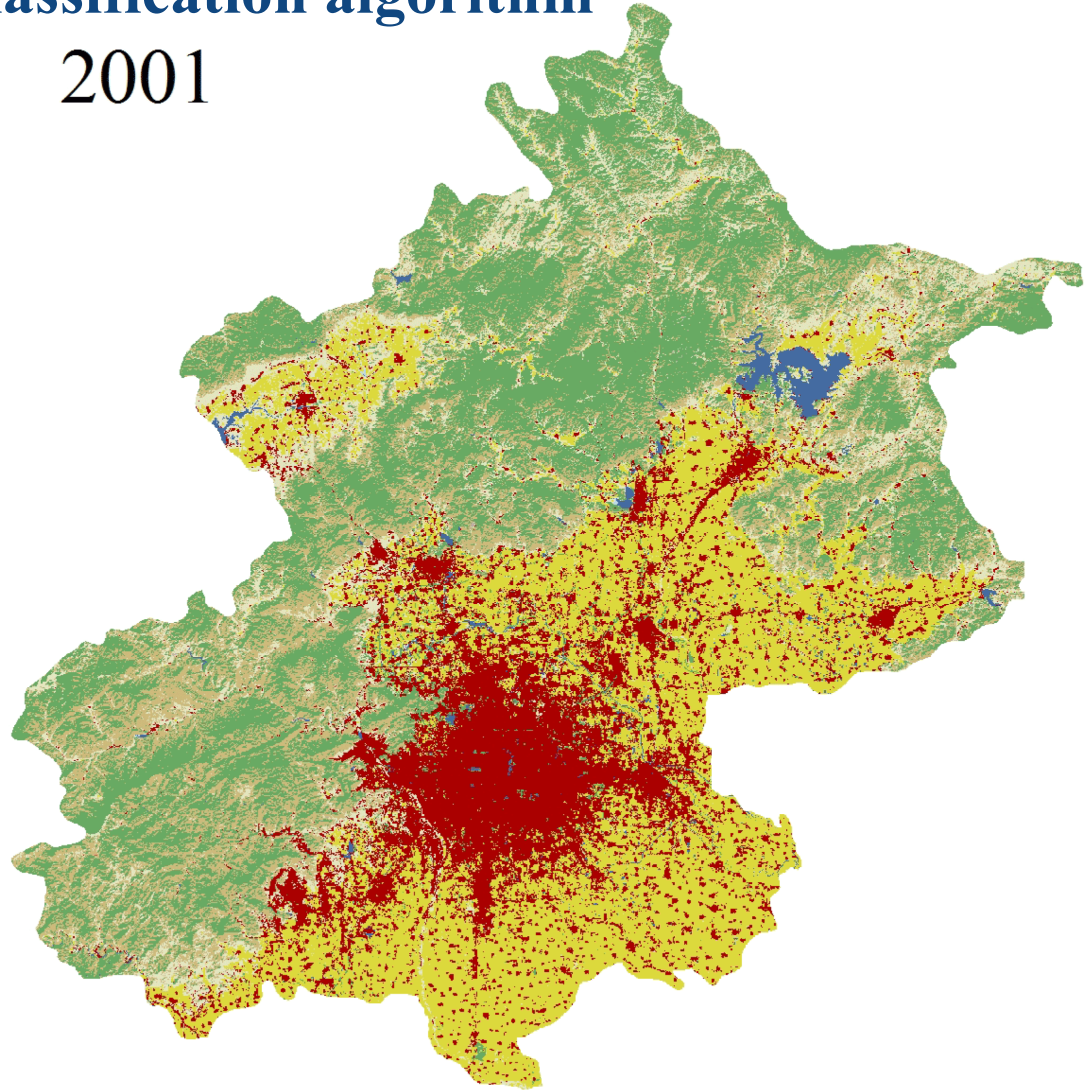

Xie S et al. (2022). Mapping the annual dynamics of land cover in Beijing from 2001 to 2020 using Landsat dense time series stack, ISPRS Journal of Photogrammetry and Remote Sensing, 185, 201-218.

5. GLC_FCS30D: Global 30-m land-cover dynamic monitoring product

- We take advantage of the continuous change-detection model and full time-series Landsat observations to capture 25 the time-points of changed pixels and identify the temporally stable areas;
- We derive high-confidence training samples from temporally stable areas of Global 30m land-cover product in 2020;
- Locally adaptive classification models are used to update the land-cover information for changed pixels;
- Temporal-consistency optimization algorithm is adopted to improve temporal stability and suppress false changes.

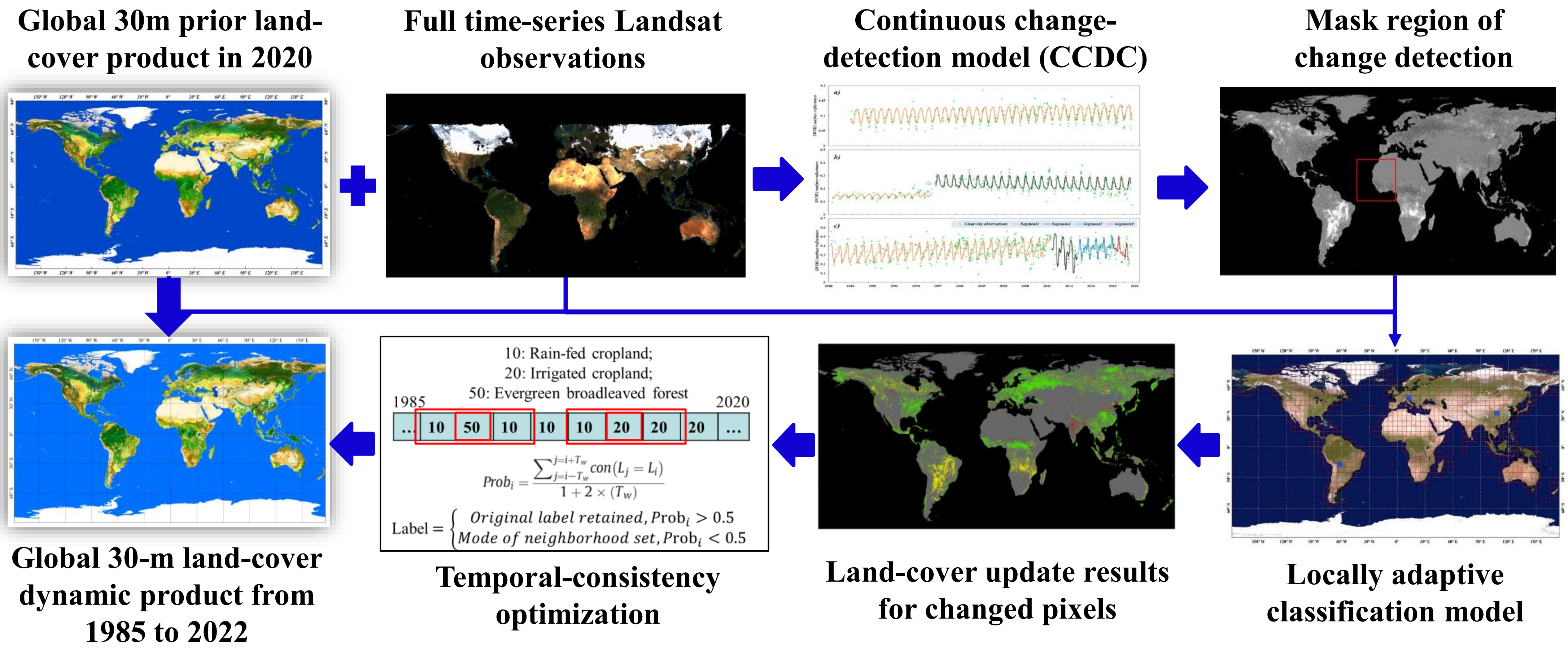

5. GLC_FCS30D: Global 30-m land-cover dynamic monitoring product

□ Global 30 m wetland dynamic mapping

In response to the current uncertainties in wetland monitoring, This study proposes a novel method for wetland mapping by combining an automatic sample extraction method, existing multi-sourced products, satellite time-series images and a stratified classification strategy, based on the complicated temporal dynamics and spectral heterogeneity of wetlands. **Wetlands are divided into 8 fine types.** Overall accuracy is 86.95±0.44%, and kappa coefficient is 0.822.

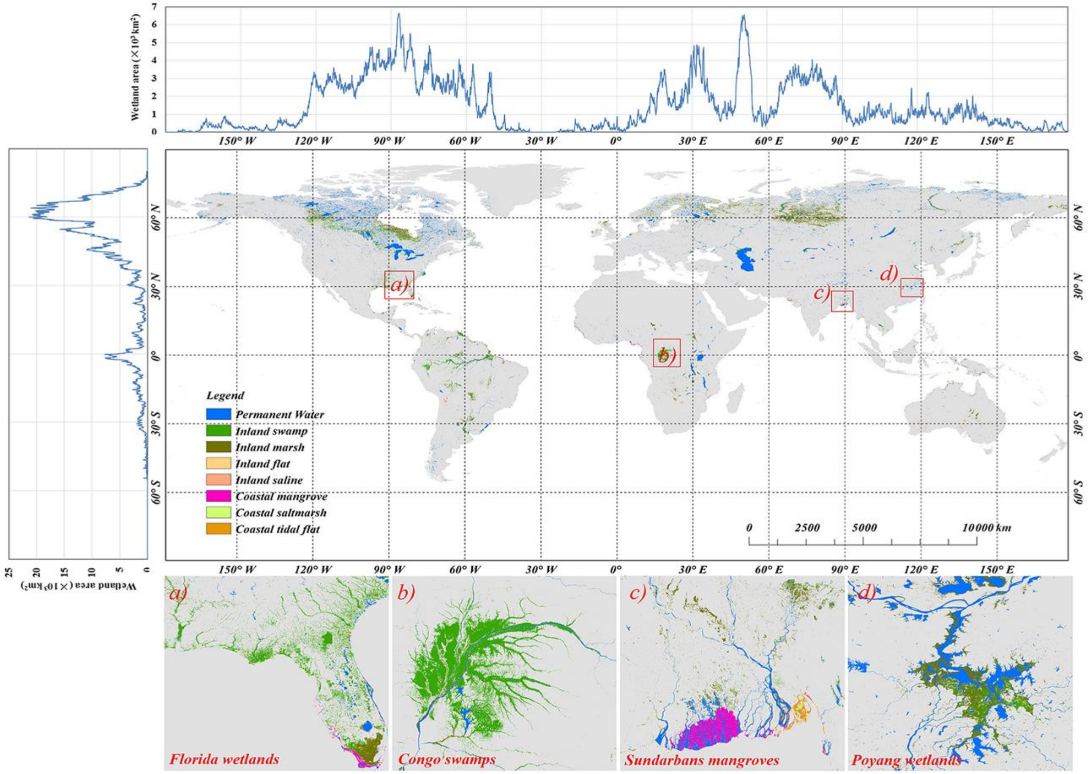

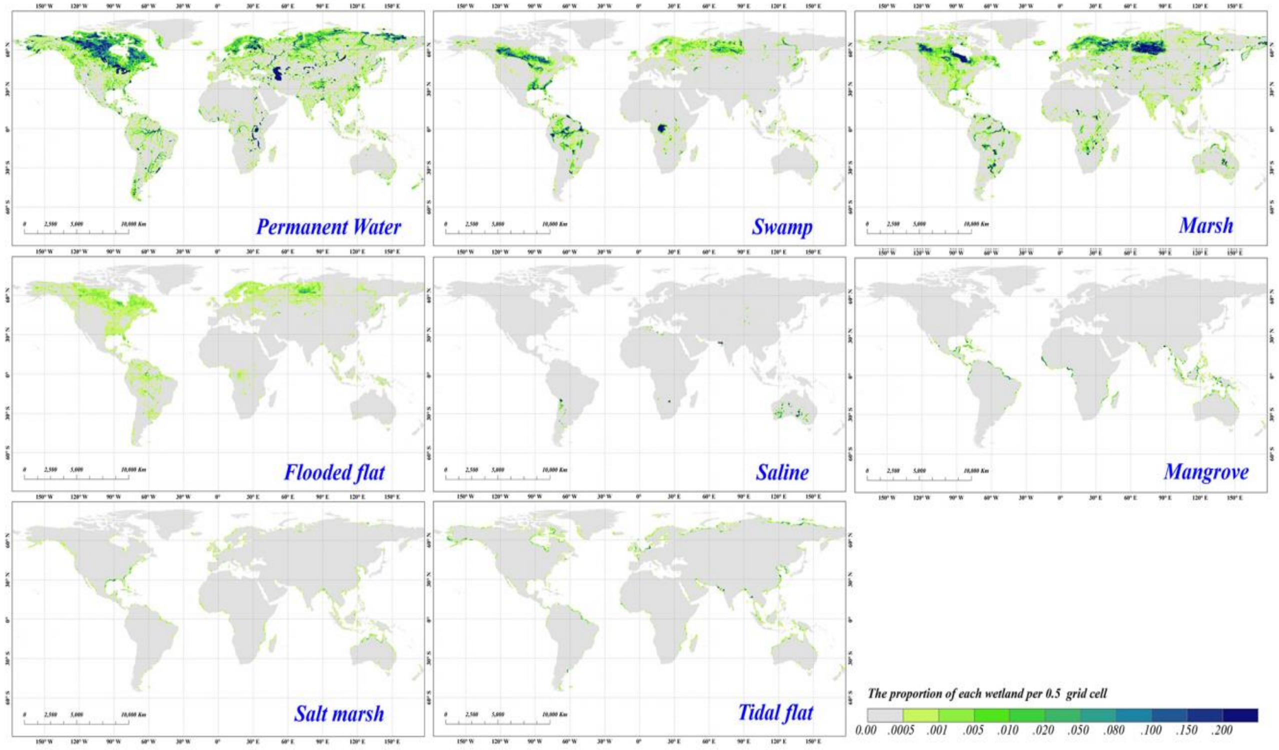

Zhang, et al. (2023). GWL_FCS30: global 30 m wetland map with fine classification system using multi-sourced and time-series remote sensing imagery in 2020. Earth System Science Data, 15(1): 265–293
Zhang, X., Liu, L., Zhao, T., et al. (2024). Global annual wetland dataset at 30 m with a fine classification system from 2000 to 2022. Scientific Data, 11(1), 310.

5. GLC_FCS30D: Global 30-m land-cover dynamic monitoring product

□ Global 30 m impervious-surface dynamic dataset

A novel and automatic method of combining the advantages of **spectral-generalization and automatic-sample-extraction strategies** was proposed, and then an accurate global 30 m impervious-surface dynamic dataset (GISD30) for 1985 to 2020 was produced using time-series Landsat imagery. <u>Overall accuracy is 90.1 % and kappa coefficient is 0.865.</u>

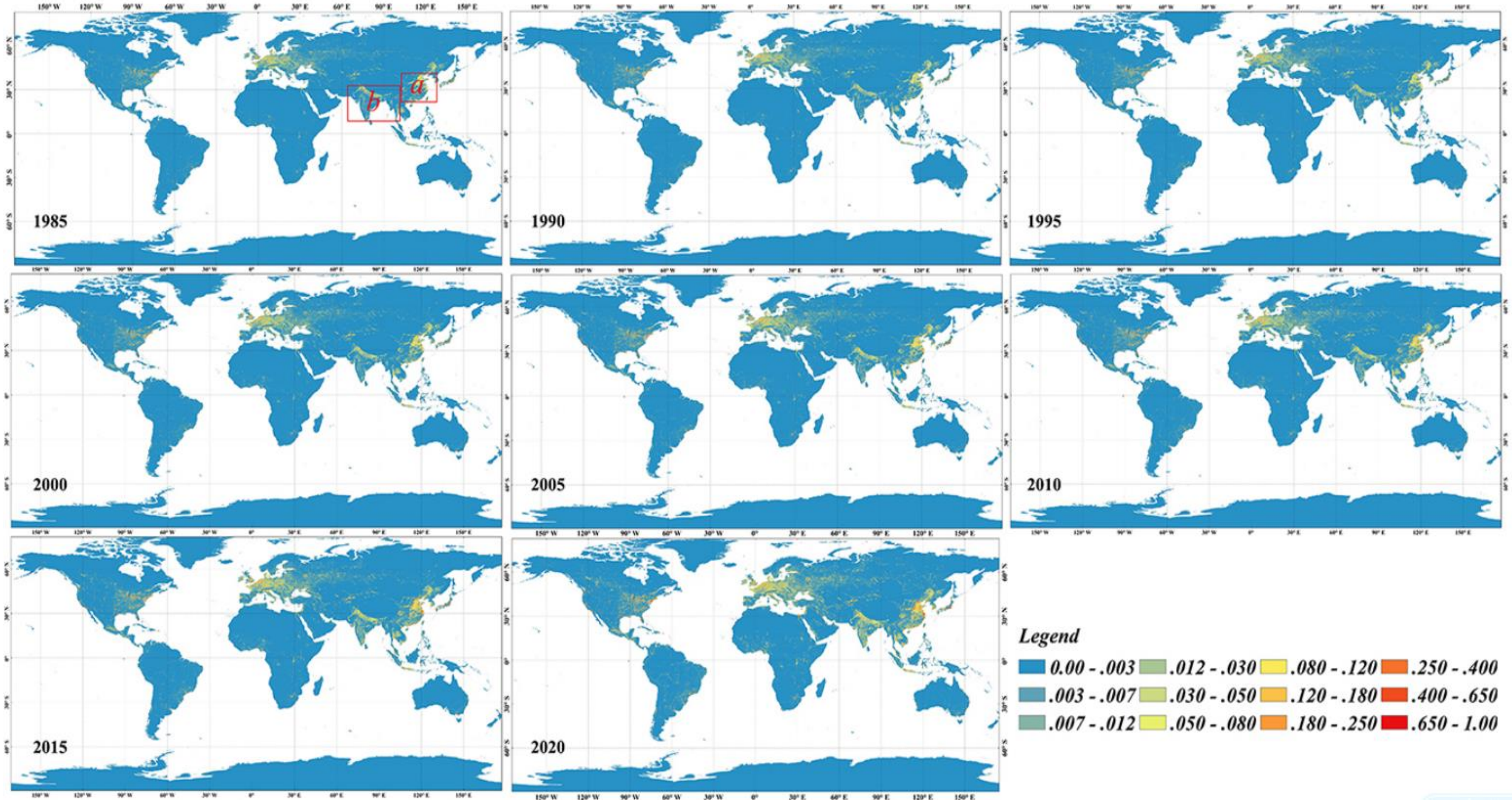

Zhang et al. (2022) GISD30: global 30 m impervious-surface dynamic dataset from 1985 to 2020 using time-series Landsat imagery on the Google Earth Engine platform, Earth Syst. Sci. Data, 14, 1831–1856

5. GLC_FCS30D: Global 30-m land-cover dynamic monitoring product

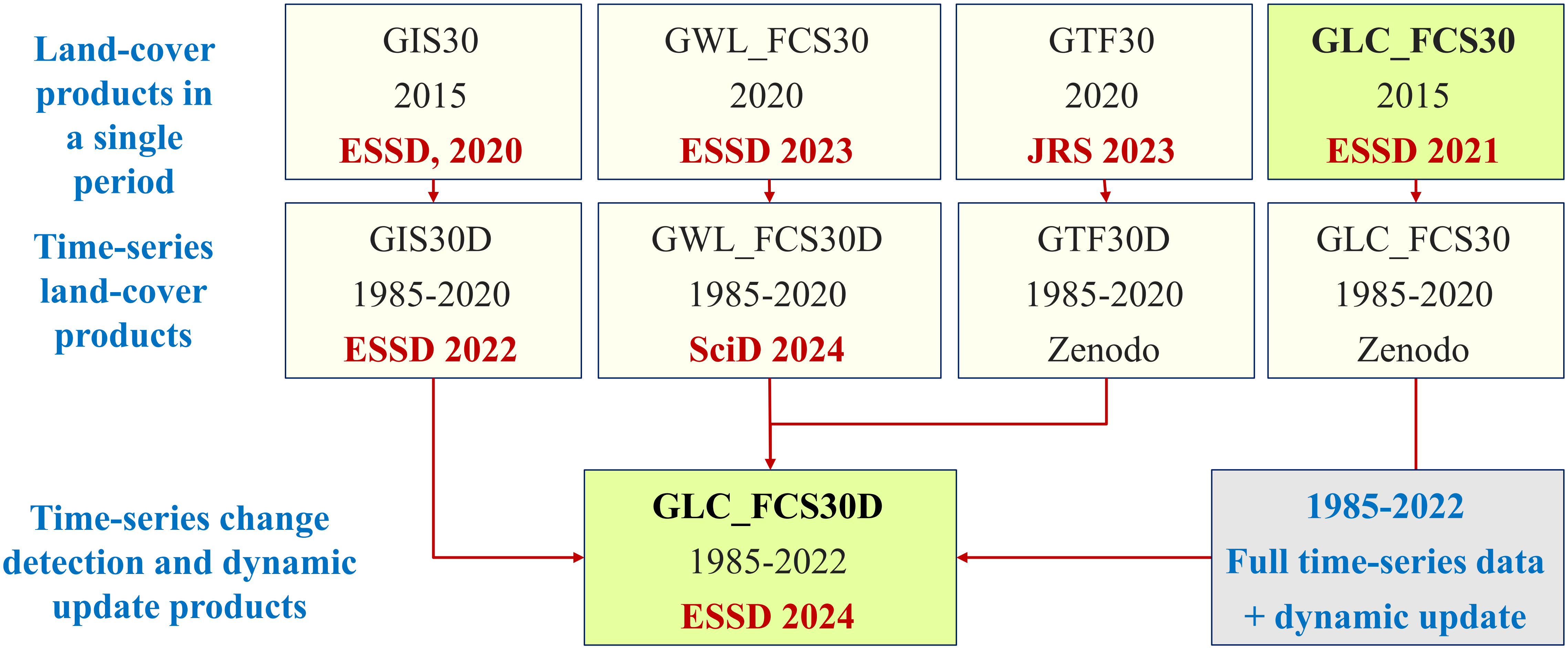

Zhang et al., ESSD 2024, Liu et al., ISPRS Annuals 2024

5. GLC_FCS30D: Global 30-m land-cover dynamic monitoring product

Based on the **continuous change detection algorithm**, training samples from stable areas are used to dynamically update changing areas. This approach has led to the development of a global 30 m land cover dynamic monitoring dataset spanning from 1985 to 2022.

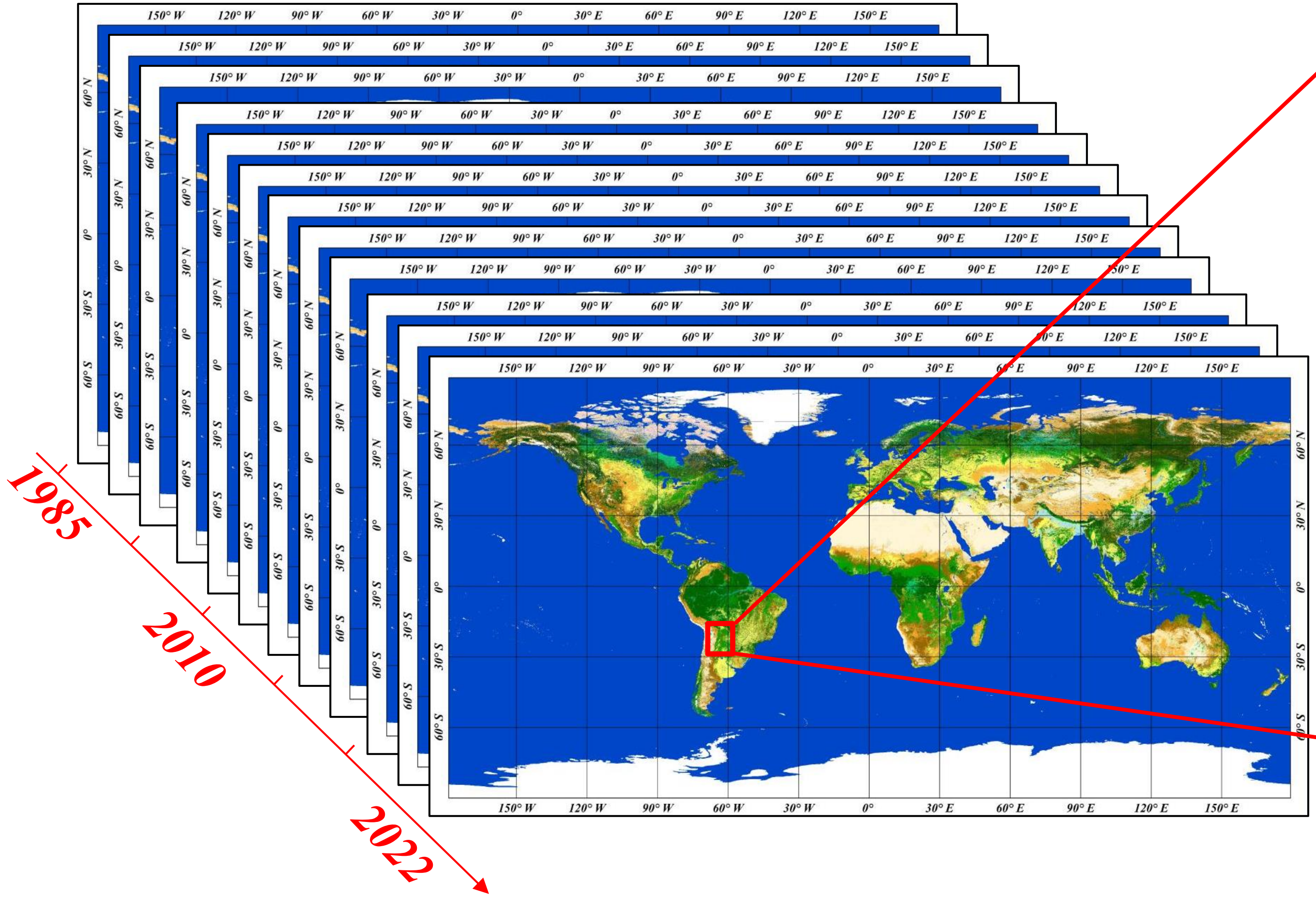

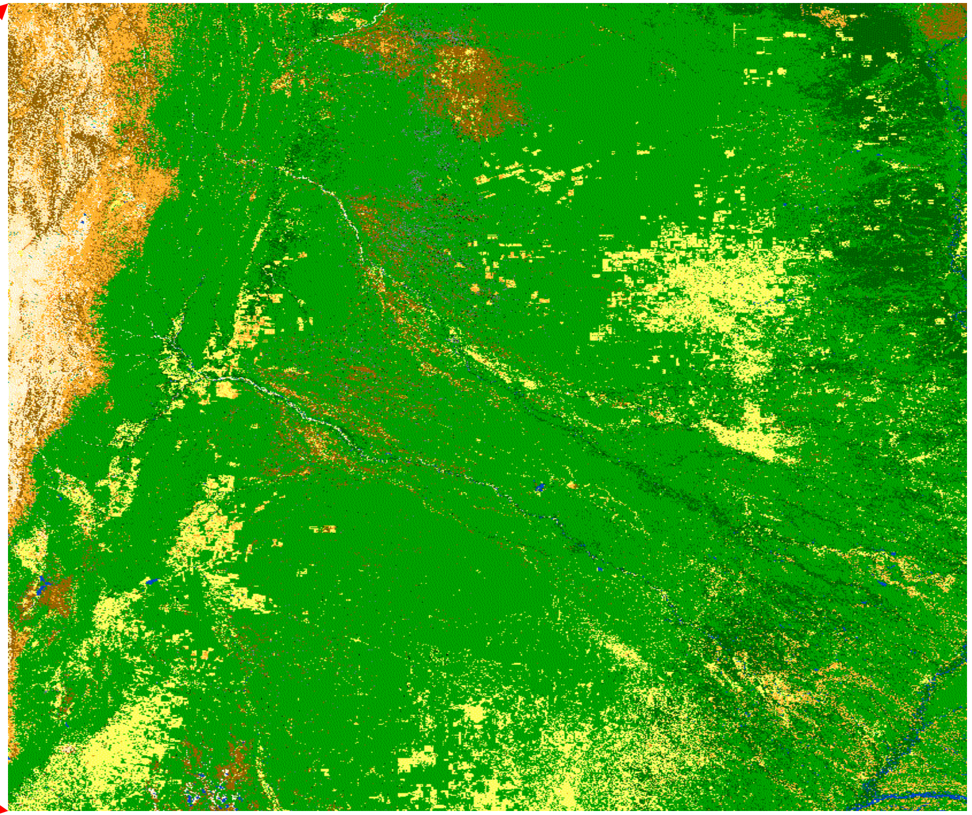

Deforestation and **cropland expansion** in South America accurately captured in GLC_FCS30D

5. GLC_FCS30D: Global 30-m land-cover dynamic monitoring product

☐ The enlargements of GLC_FCS30D

- The deforestation in South America is widely recognized, and GLC_FCS30D clearly reflects this trend. Namely, **the early deforestation showed a grid distribution, and then each grid gradually extended outward and finally connected into patches**.
- In the **Yangtze River Delta**, GLC_FCS30D depicts that the **dominant land-cover change over the enlargement is urbanization**, and **a large quantity of irrigated cropland has been converted to impervious surfaces**. And urban expansion was significantly faster before 2010 than after 2010 according to GLC_FCS30D.

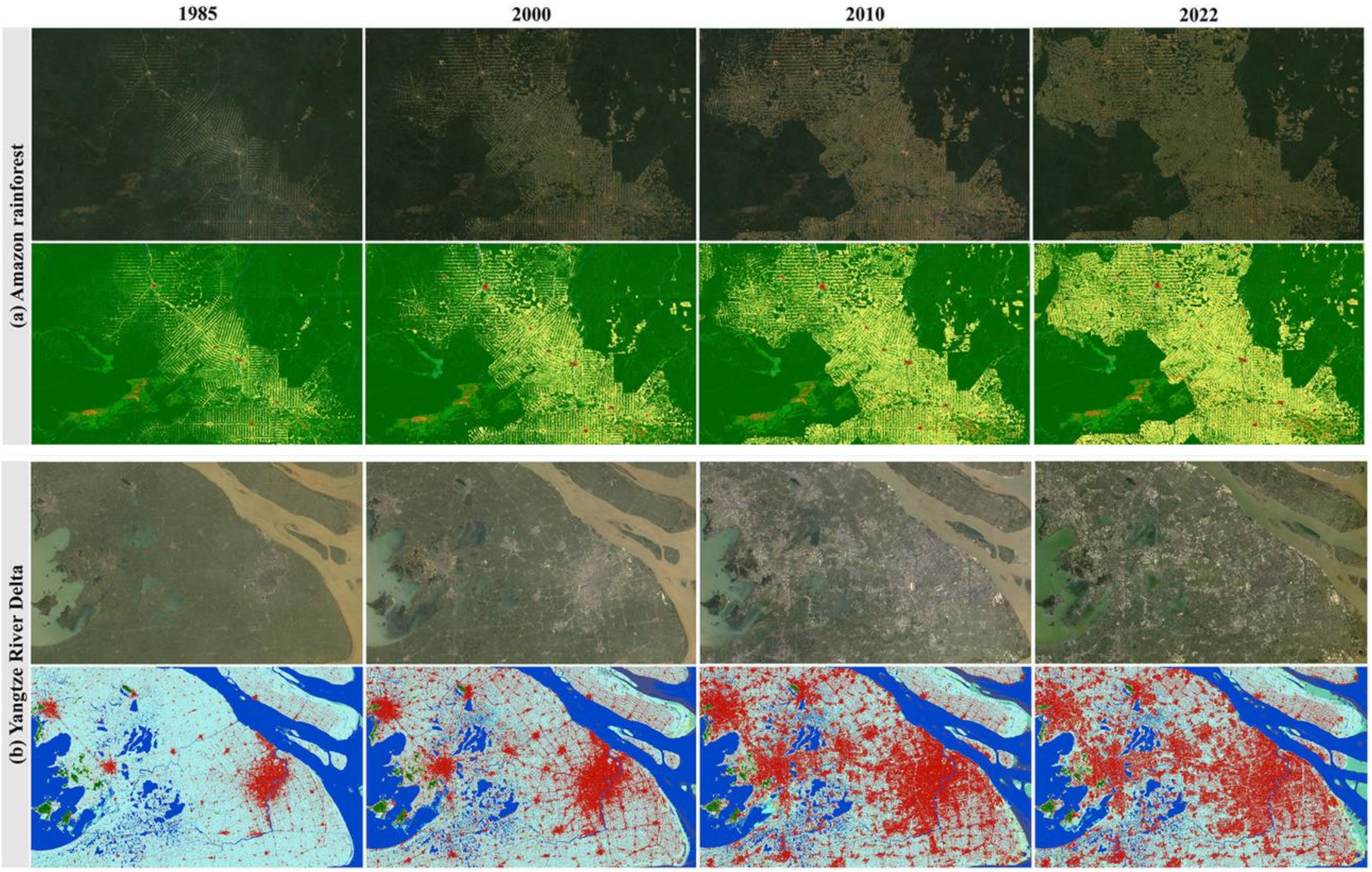

5. GLC_FCS30D: Global 30-m land-cover dynamic monitoring product

A novel stratified random sampling global land-cover validation dataset

- We adopted the stratified equal-area sampling method to allocate 80,000 validation samples.
- A visual interpretation module that integrates spatiotemporal spectrum information was developed using Google Earth high-resolution images and time-series auxiliary data.
- The collection of validation dataset in 2020 has been completed, and that from 1985 to 2020 is being produced.

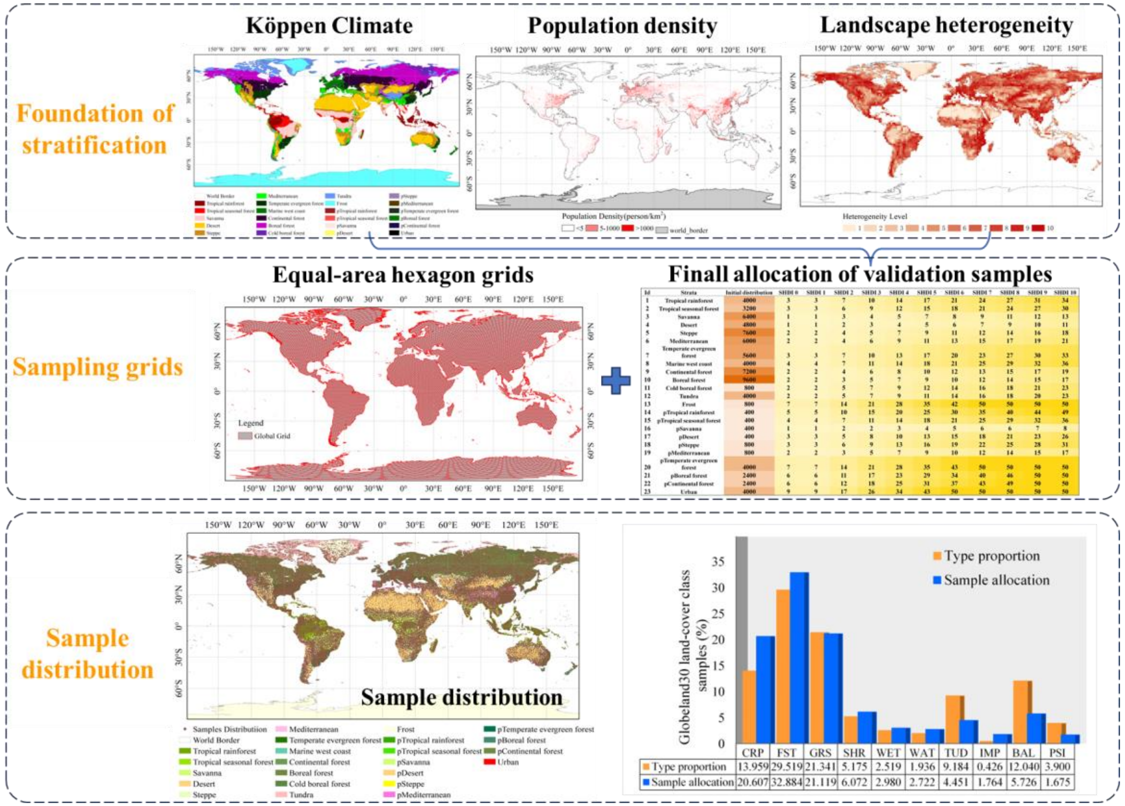

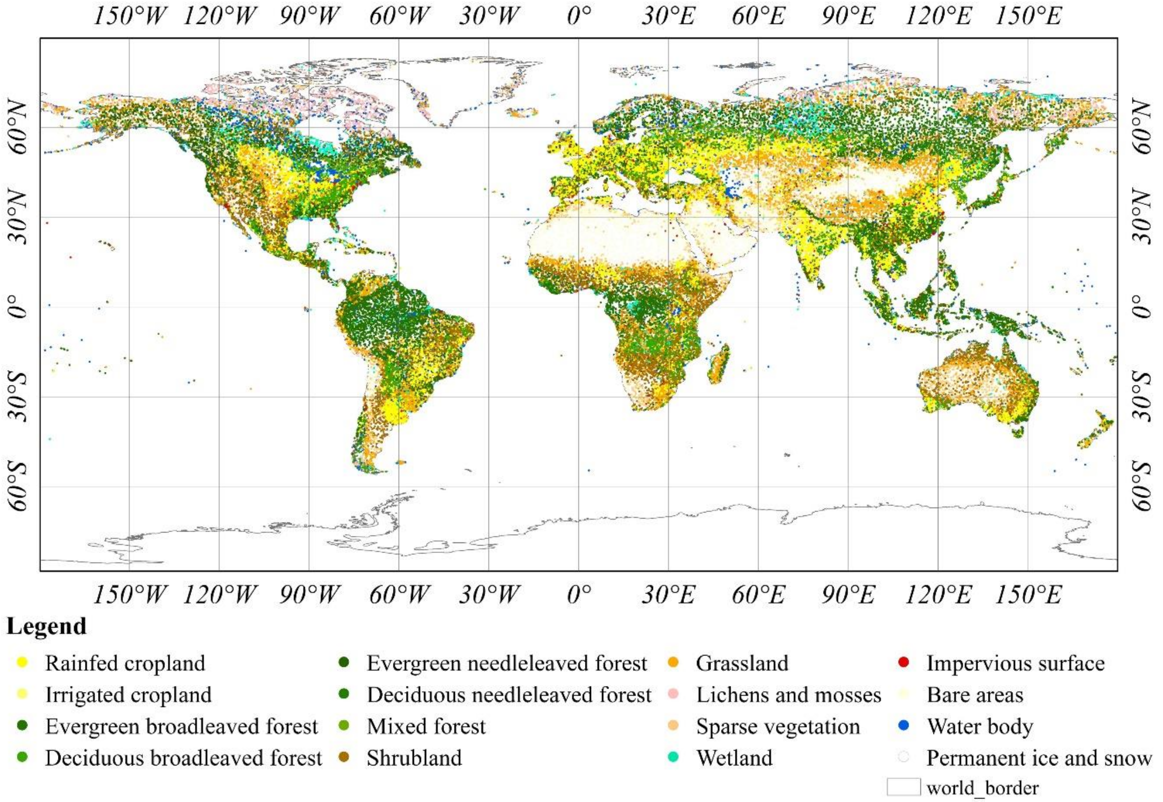

Zhao T et al. Assessing the Accuracy and Consistency of Six Fine-Resolution Global Land Cover Products Using a Novel Stratified Random Sampling Validation Dataset. *Remote Sensing*. 2023; 15(9):2285. https://doi.org/10.3390/rs15092285

5. GLC_FCS30D: Global 30-m land-cover dynamic monitoring product

Using multisourced remote sensing datasets, a novel interpretation tool is designed on the GEE platform

5. GLC_FCS30D: Global 30-m land-cover dynamic monitoring product

Accuracy comparison of global land-cover products based on statistical sampling (2020)

	GlobeLand30		FROM-GLC30		GLC_FCS30		FROM-GLC10		ESA_WC		ESRI_LC	
	P.A.	U.A.	P.A.	U.A.	P.A.	U.A.	P.A.	U.A.	P.A.	U.A.	P.A.	U.A.
CRP	86.39(±1)	76.00(±1)	47.02(±2)	74.36(±1)	83.36(±1)	73.55(±1)	55.03(±1)	77.88(±2)	61.99(±1)	87.61(±2)	65.13(±1)	86.28(±1)
FST	81.16(±1)	82.97(±2)	81.47(±2)	82.80(±1)	87.97(±1)	80.72(±2)	79.56(±2)	87.50(±1)	88.05(±1)	83.13(±1)	84.35(±1)	80.98(±2)
GRS	72.09(±2)	43.52(±2)	69.08(±1)	36.76(±2)	48.14(±2)	61.38(±2)	65.18(±2)	39.82(±2)	72.25(±2)	43.13(±2)	13.54(±2)	54.50(±3)
SHR	28.44(±2)	57.74(±2)	39.12(±4)	52.39(±2)	48.30(±2)	60.22(±2)	47.66(±5)	57.33(±2)	36.04(±4)	63.08(±2)	66.55(±2)	26.59(±2)
WET	63.08(±3)	52.32(±3)	2.20(±1)	43.60(±7)	49.33(±2)	41.37(±2)	4.30(±1)	47.85(±5)	33.90(±2)	50.38(±4)	27.01(±4)	45.36(±2)
WAT	85.27(±2)	86.32(±1)	88.18(±1)	77.48(±2)	81.37(±1)	92.68(±1)	87.07(±1)	89.22(±1)	90.48(±1)	89.72(±1)	87.05(±1)	86.84(±1)
IMP	69.39(±2)	58.20(±2)	48.31(±3)	69.17(±2)	75.33(±2)	75.28(±2)	73.41(±2)	65.70(±3)	82.99(±2)	86.89(±1)	88.42(±2)	43.36(±2)
BAL	73.48(±4)	93.59(±2)	83.17(±3)	86.51(±3)	85.69(±3)	79.76(±5)	89.31(±2)	80.32(±3)	81.00(±3)	82.70(±5)	44.41(±4)	91.11(±3)
SNI	94.21(±5)	95.22(±0)	88.81(±5)	96.45(±3)	93.15(±2)	93.14(±5)	93.50(±2)	83.81(±6)	92.57(±3)	95.65(±3)	95.13(±3)	78.27(±7)
O.A.	**69.96(±9)**		**66.30(±8)**		**72.55(±9)**		**68.95(±8)**		**70.54(±9)**		**58.90(±7)**	
Kappa	**0.6302**		**0.5589**		**0.6589**		**0.6064**		**0.6343**		**0.5394**	

Zhao T et al. Assessing the Accuracy and Consistency of Six Fine-Resolution Global Land Cover Products Using a Novel Stratified Random Sampling Validation Dataset. *Remote Sensing*. 2023; 15(9):2285. https://doi.org/10.3390/rs15092285

5. GLC_FCS30D: Global 30-m land-cover dynamic monitoring product

◆Time-series third-party validation dataset (EU LUCAS dataset) accuracy assessment for GLC_FCS30D

The GLC_FCS30D dataset has a mean overall accuracy of 81.91%(±0.09%) ranging from **81.64% (0.09%) to 82.11% (0.09%)** in EU. Each accuracy indicator shows a good stability in the time dimension.

	2006		2009		2012		2015		2018	
	P.A.(SE)	U.A.(SE)	P.A.(SE)	U.A.(SE)	P.A.(SE)	U.A.(SE)	P.A.(SE)	U.A.(SE)	P.A.(SE)	U.A.(SE)
CRP	85.49(0.11)	93.37(0.08)	85.40(0.11)	93.31(0.08)	85.50(0.11)	93.17(0.08)	85.47(0.11)	93.05(0.08)	85.52(0.11)	92.82(0.08)
FST	95.22(0.08)	76.71(0.15)	94.97(0.08)	76.71(0.15)	94.79(0.09)	76.82(0.15)	94.36(0.09)	76.82(0.15)	93.71(0.09)	76.85(0.15)
GRS	6.13(0.26)	21.31(0.83)	6.10(0.26)	21.13(0.83)	6.05(0.26)	20.98(0.83)	6.08(0.26)	20.71(0.82)	5.99(0.26)	20.74(0.82)
SHR	8.13(0.42)	8.93(0.46)	8.25(0.43)	8.92(0.46)	8.02(0.42)	8.77(0.46)	7.84(0.42)	8.60(0.45)	8.35(0.43)	8.96(0.46)
WET	63.10(0.81)	66.55 (0.81)	61.40(0.81)	65.55(0.82)	61.86(0.81)	66.21(0.82)	62.64(0.81)	66.60(0.81)	62.94(0.81)	65.34 (0.81)
WTR	89.73(0.40)	92.44(0.36)	90.09(0.40)	92.53(0.35)	90.28(0.39)	92.36(0.36)	90.83(0.38)	91.63(0.37)	90.10(0.40)	91.56(0.37)
IMP	58.55(0.56)	72.69(0.56)	59.21(0.55)	72.06(0.56)	59.06(0.55)	71.72(0.56)	58.65(0.55)	70.85(0.56)	59.01(0.55)	70.29(0.56)
BAL	52.77(1.12)	39.62(0.95)	52.90(1.12)	38.44(0.93)	52.19(1.13)	37.70(0.93)	52.07(1.13)	36.16(0.90)	52.33(1.13)	34.69(0.87)
PSI	86.02(5.00)	35.01(4.38)	91.40(4.04)	36.56(4.38)	89.25(4.46)	31.86(4.00)	96.24(2.74)	31.40(3.81)	96.24(2.74)	31.35(3.81)
O.A.(SE)	82.11(0.09)		81.99(0.09)		81.97(0.09)		81.82(0.09)		81.64(0.09)	

5. GLC_FCS30D: Global 30-m land-cover dynamic monitoring product

◆Time-series third-party validation dataset (American LCMAP dataset) accuracy assessment for GLC_FCS30D

The GLC_FCS30D achieves a mean overall accuracy of 79.50% (±0.50%) and varies from a high value of **80.04% (± 0.49%)** in 2015 to a low value of **78.91% (± 0.51%)** in 2000. Both the producer's accuracy and user's accuracy in various types have significant stability in the time dimension.

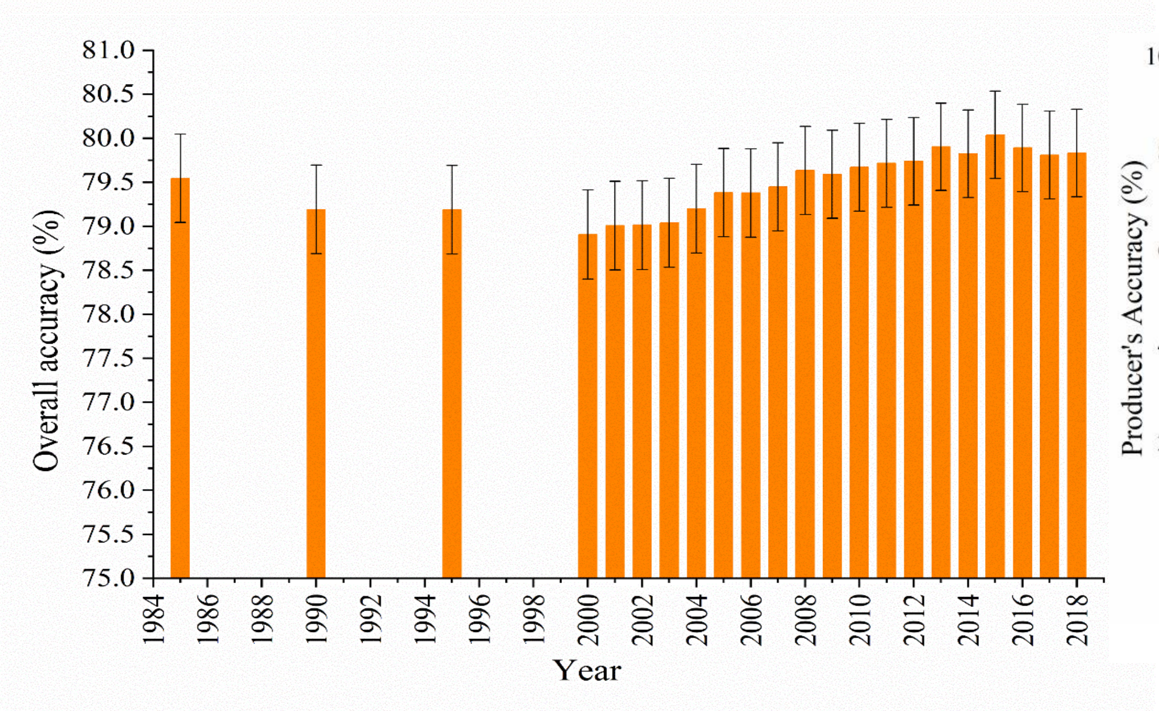

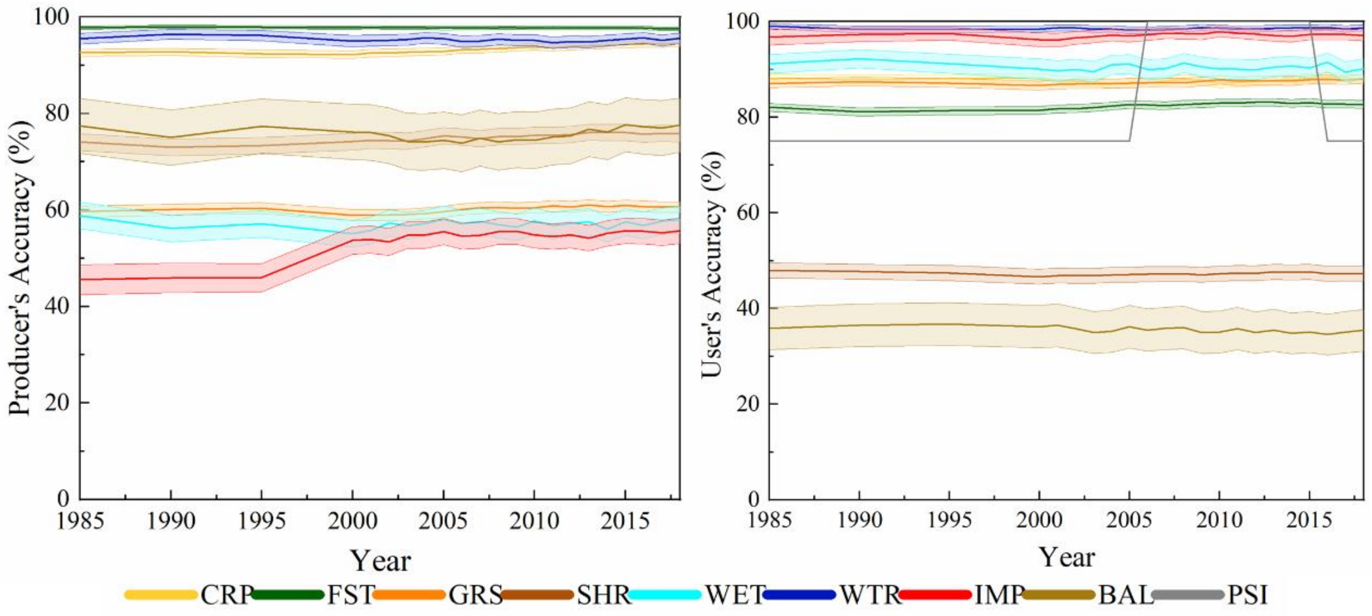

5. GLC_FCS30D: Global 30-m land-cover dynamic monitoring product

◆Comparison with GLanCE products supported by NASA MEASURES project

The GLanCE product will be a 30-meter spatial resolution data record providing high quality representation of **current and past global land cover, land use and land cover change** at annual time steps from 2001 to 2019.

Classification System：

GLC_FCS30D: 35 land-cover types

VS

GLanCE: 7 land-cover types

Time Range：

GLC_FCS30D: 1985-2022

VS

GLanCE: 2001-2019

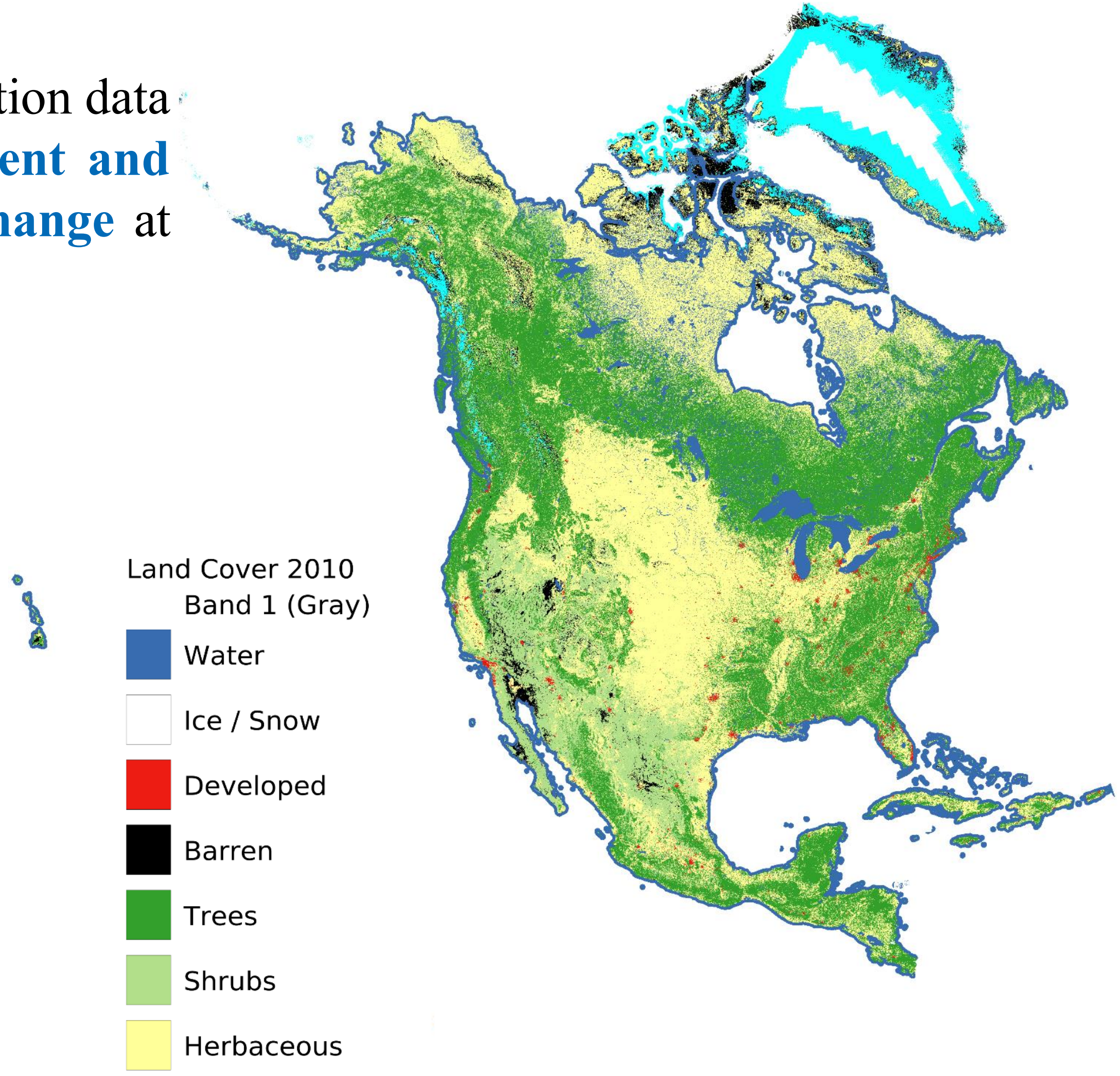

5. GLC_FCS30D: Global 30-m land-cover dynamic monitoring product

Overall status of global land cover changes

During 1985–2020, the net change area of global land cover reached **533.27 Mha**, accounting for 3.63% of the total land area (excluding Antarctica). Among them, **forest changes and impervious surfaces expansion** are the most significant, the net forest loss area was 240.01 Mha, 4.84% decrease compared with 1985. Impervious surfaces area increased 104.43% compared with 1985, with the largest relative increase and an increased area of approximately 55.88 Mha.

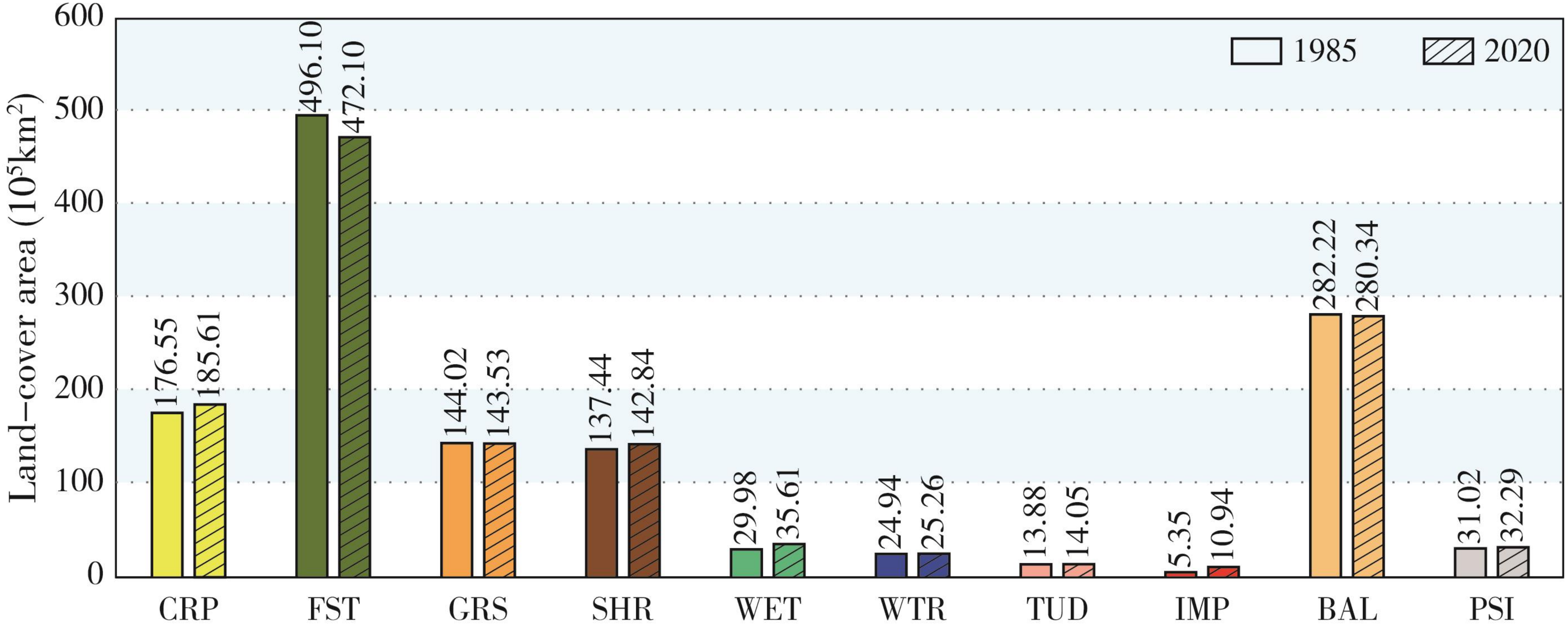

5. GLC_FCS30D: Global 30-m land-cover dynamic monitoring product

Global forest cover changes

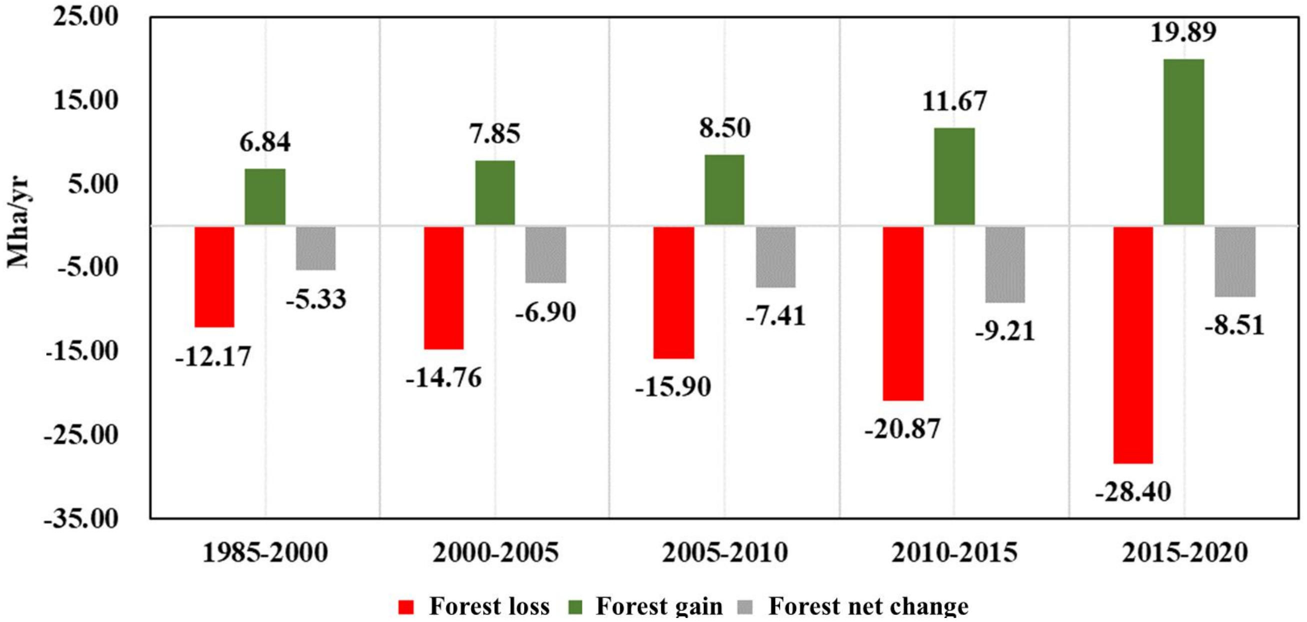

Figure Forest area change rate based on GLC_FCS30D

Time	forest loss area（Mha）	
	GFC	GLC_FCS30D
2001-2005	91.67	73.78
2006-2010	99.08	79.52
2010-2015	123.04	104.36
2016-2019	131.57(4 years)	142.00
∑	445.36(19 years)	399.67

- **Forest loss** and **forest gain** show a significantly accelerating trend (**0.37Mha/yr², P<0.01**; **0.18Mha/yr², P<0.01**);
- Global forest area continues to decline, but the rate of decline has slowed since 2015;
- Global Forest Change is currently the only global 30 m forest change product (Hansen et al., Science, 2013). the total forest damage of GLC_FCS30D from 2000 to 2020 is close to this dataset, but **GLC_FCS30D can better reflect the doubling of the global forest damage rate**.

5. GLC_FCS30D: Global 30-m land-cover dynamic monitoring product

Global wetlands cover changes

The change area of each wetland subtype between 2000 and 2022 were calculated. The results showed that the **wetland area had a slight increasing trend** (most of which occur in wetlands covered by seasonal water bodies) due to the joint influence of **global warming and human activities** (construction of water conservancy facilities).

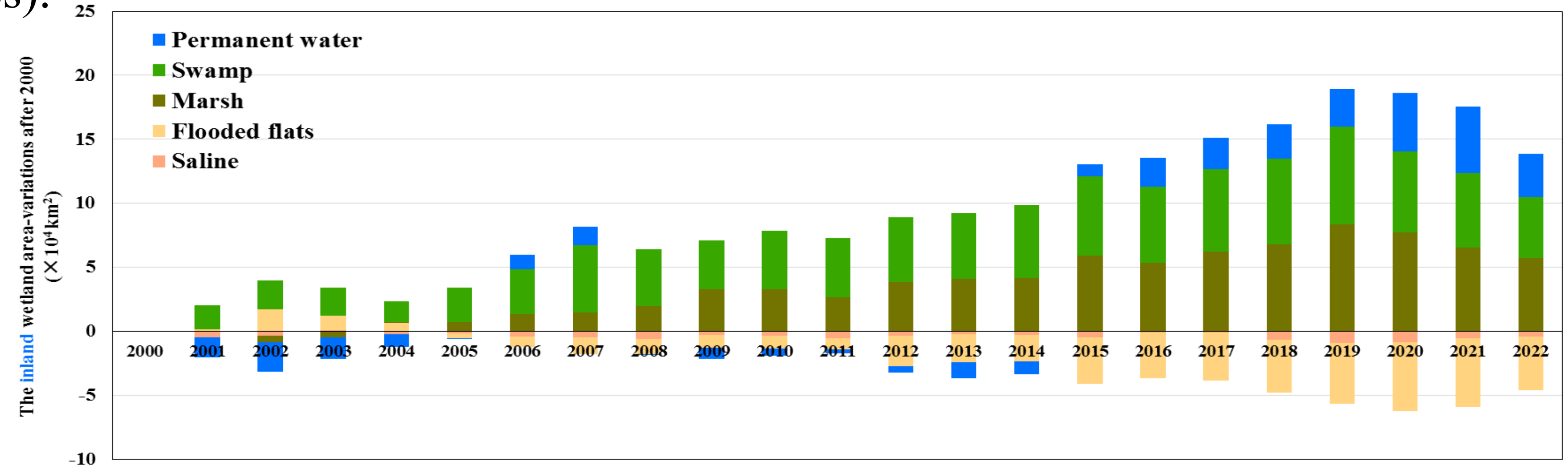

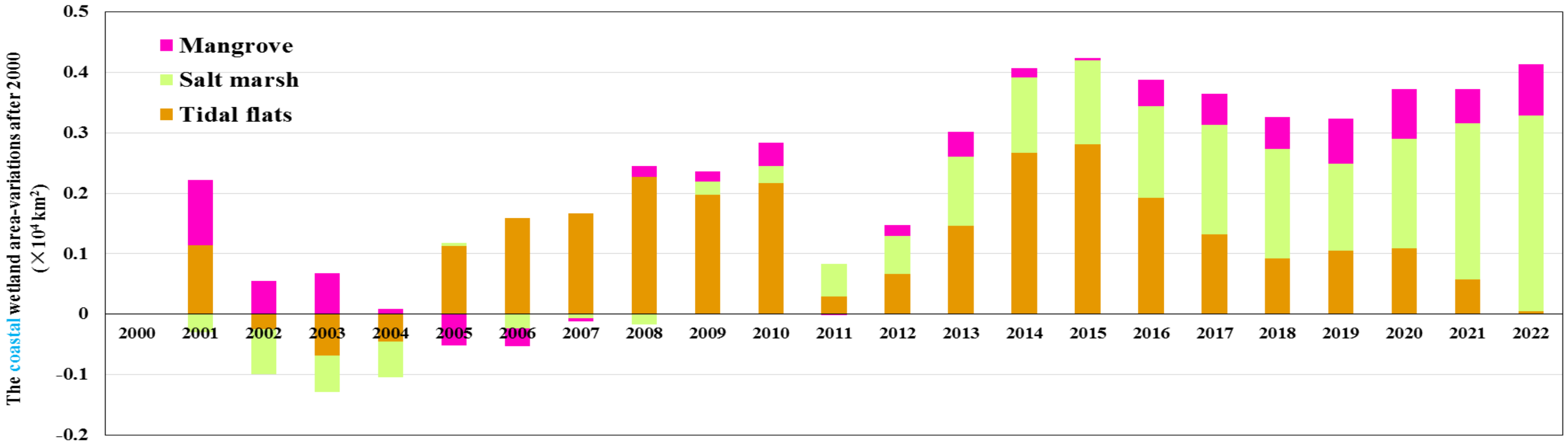

5. GLC_FCS30D: Global 30-m land-cover dynamic monitoring product

Global impervious surface changes

The area of global impervious surfaces has significantly increased from **53.51 Mha in 1985** to **109.39 Mha in 2020**. The proportion of global land area (except for Antarctica) has increased from 0.36% to 0.74%, showing a total growth area of 55.88 Mha and an augmentation of **104.43% compared to 1985** as well as an average growth rate of 1.60 Mha/yr.

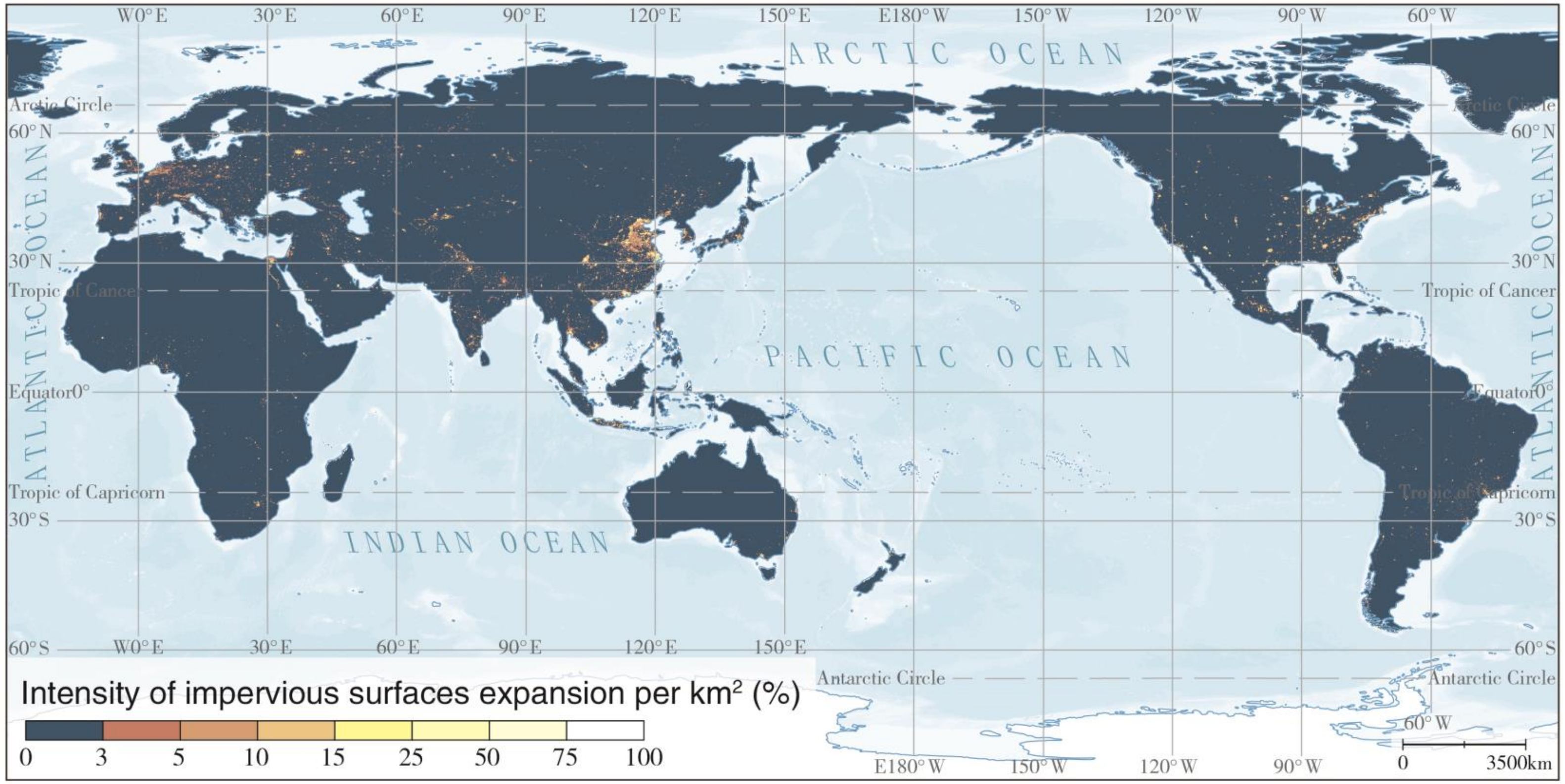

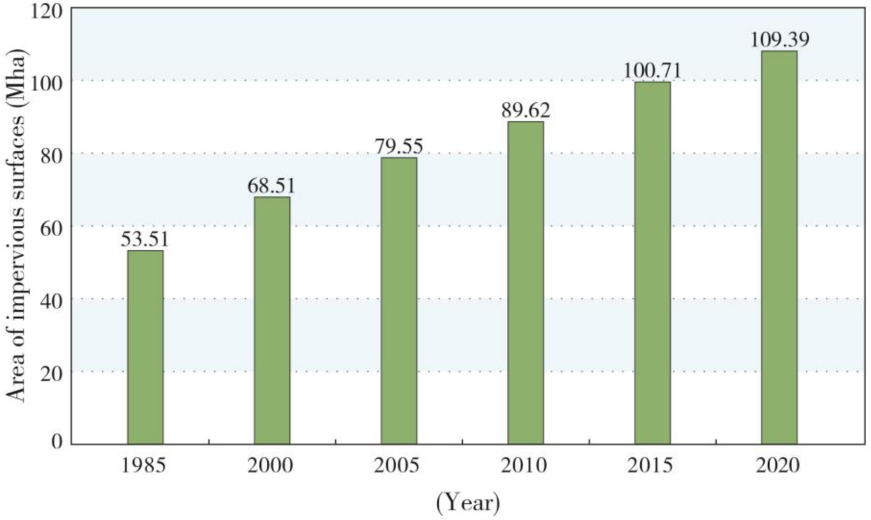

5. GLC_FCS30D: Global 30-m land-cover dynamic monitoring product

□ The comparisons with other LCC products

The comparisons with CCI-LC (ESA) and MCD12Q1 (NASA) indicate that GLC_FCS30D achieves the optimal performance:

1) The CCI-LC dataset **underestimated the forest cover** in 2001, i.e., some forests were wrongly labeled croplands; and **some deforested areas were not captured** during the period 2001–2020;
2) MCD12Q1 also suffered from a forest omission error, and showed various land-cover distributions in wetland areas, which indicated that MCD12Q1 has **lower mapping accuracy and temporal stability for these wetland areas**.

The **GLC_FCS30D** adopted the continuous land-cover change detection strategy, therefore, it achieves **great spatiotemporal stability** and **captures rich spatial details**.

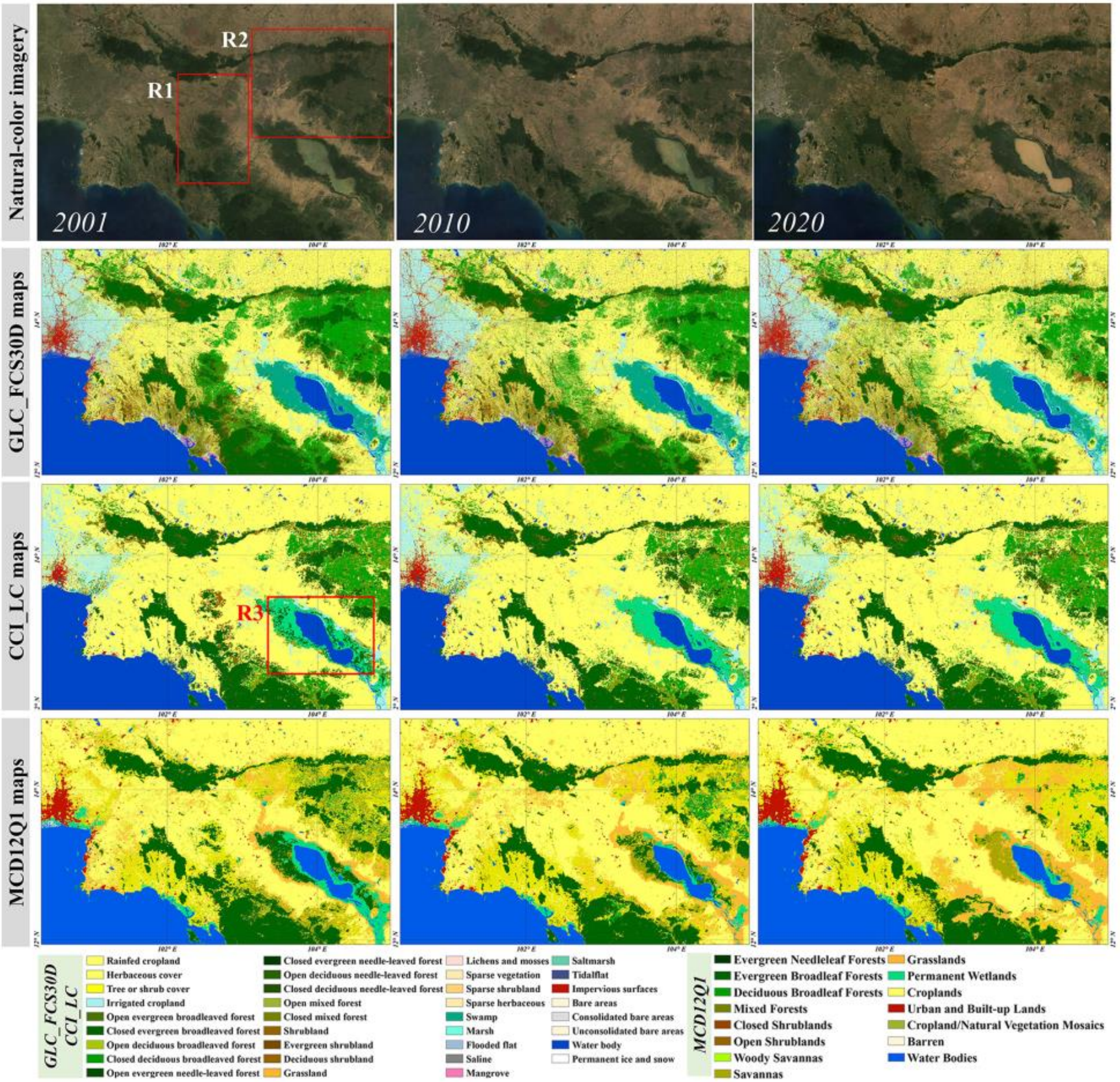

Contents

6-1: The carbon emission from global land-cover changes

The spatiotemporal characteristics of accelerated carbon emissions caused by global land-cover changes from the perspectives of carbon loss and carbon sequestration were revealed.

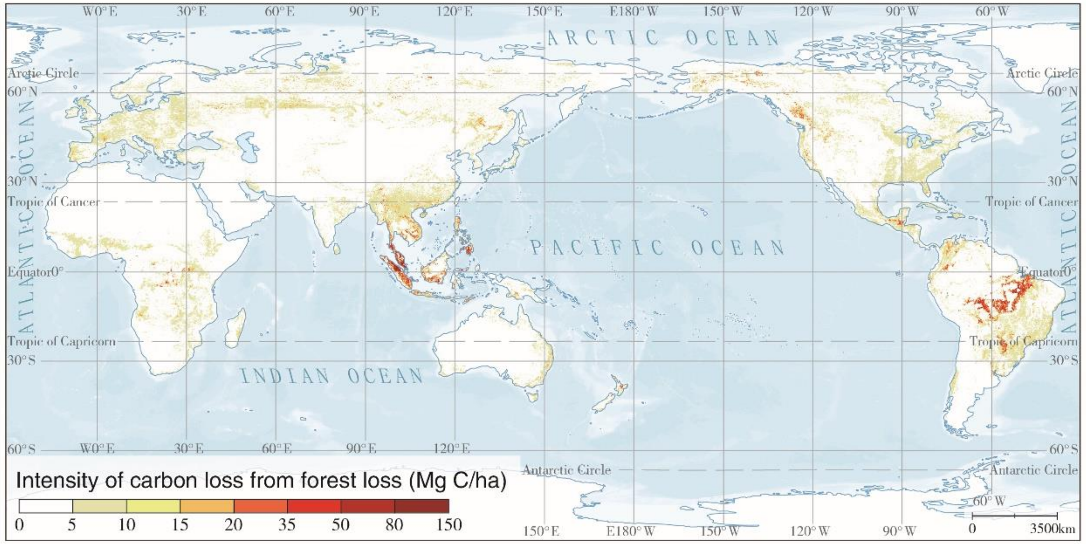

- ✓Carbon loss from global forest loss were **34.22 ± 2.02 PgC** during 1985–2020, with **the loss rate more than doubling**.
- ✓The global carbon loss notably distributed on **rainforests and boreal forests**.

- ◆Carbon sequestration from forest gain (**9.84 ± 0.31 PgC**) offset about **30%** of the carbon loss above and exhibited a similar spatial distribution.
- ◆The **tropics** contributed nearly **3/4** of global carbon sequestration.

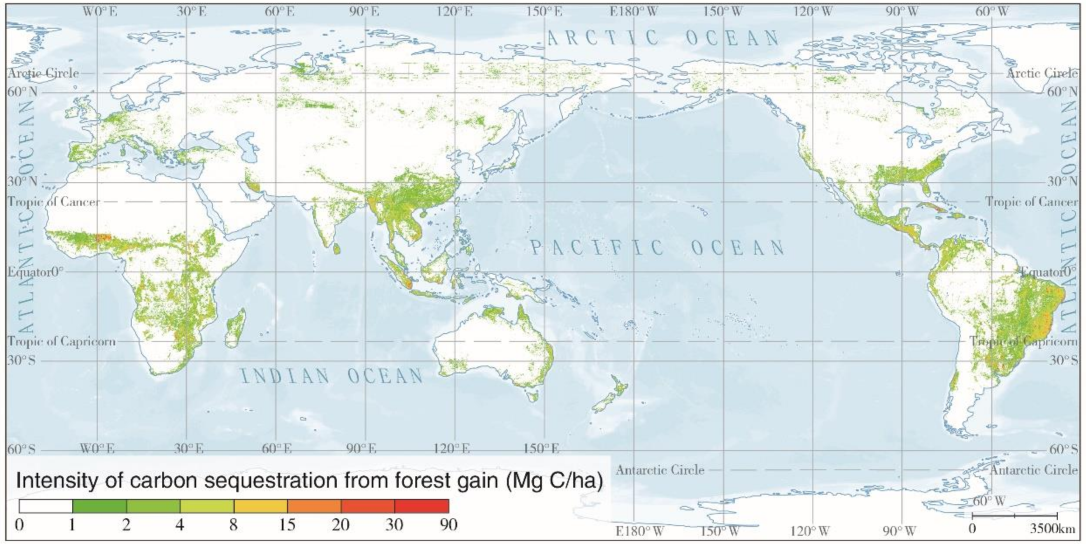

6-2: Global cropland area dynamics and analysis

- Global cropland area has been expanded and lost by **3.703 million km²** and **2.759 million km²**, respectively, and the net gain in cropland area was **0.944 million km²** from 1985 to 2022, equivalent to 5.33% of the 1985 cropland area.
- Cropland area underwent a state of **loss** in the latitude range of 20ºN~40ºN, whereas the **positive net change** of cropland area was primarily concentrated in the range of **30ºS ~ 10ºN (tropics)**.
- The proportions of cropland expansion were relatively **high in Africa and South America**, increasing by 26.33% (**0.547 million km²**) and 32.11% (**0.966 million km²**) from 1985 to 2022

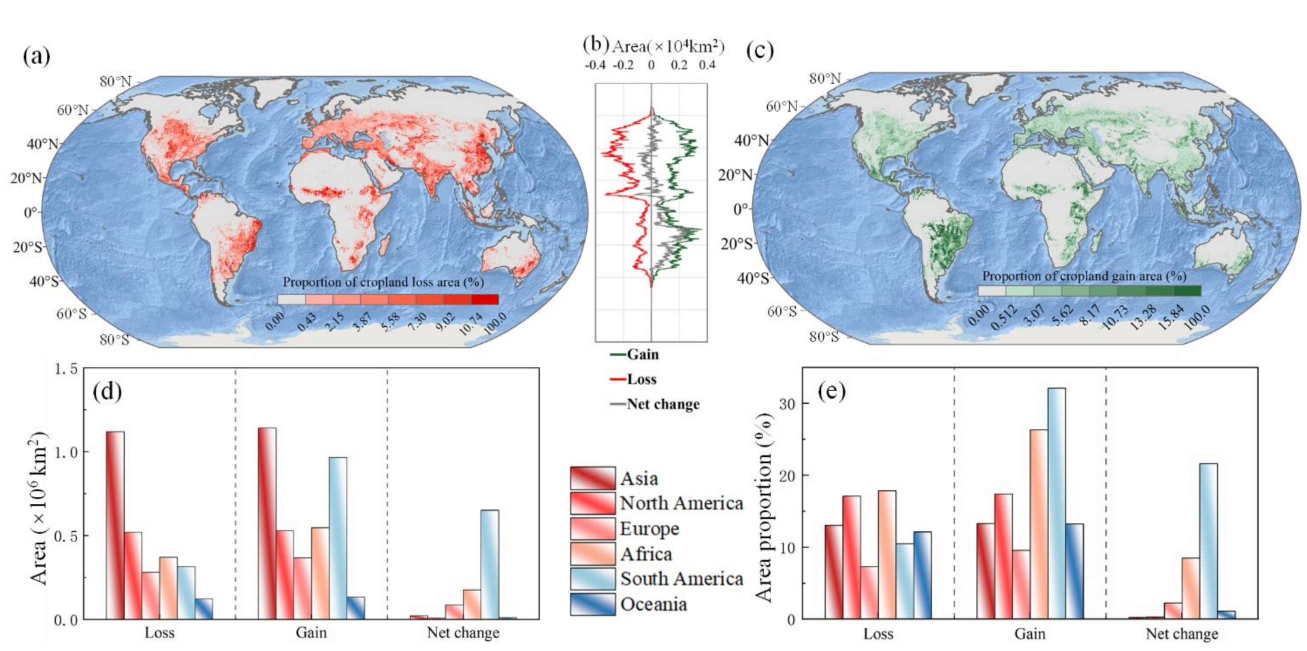

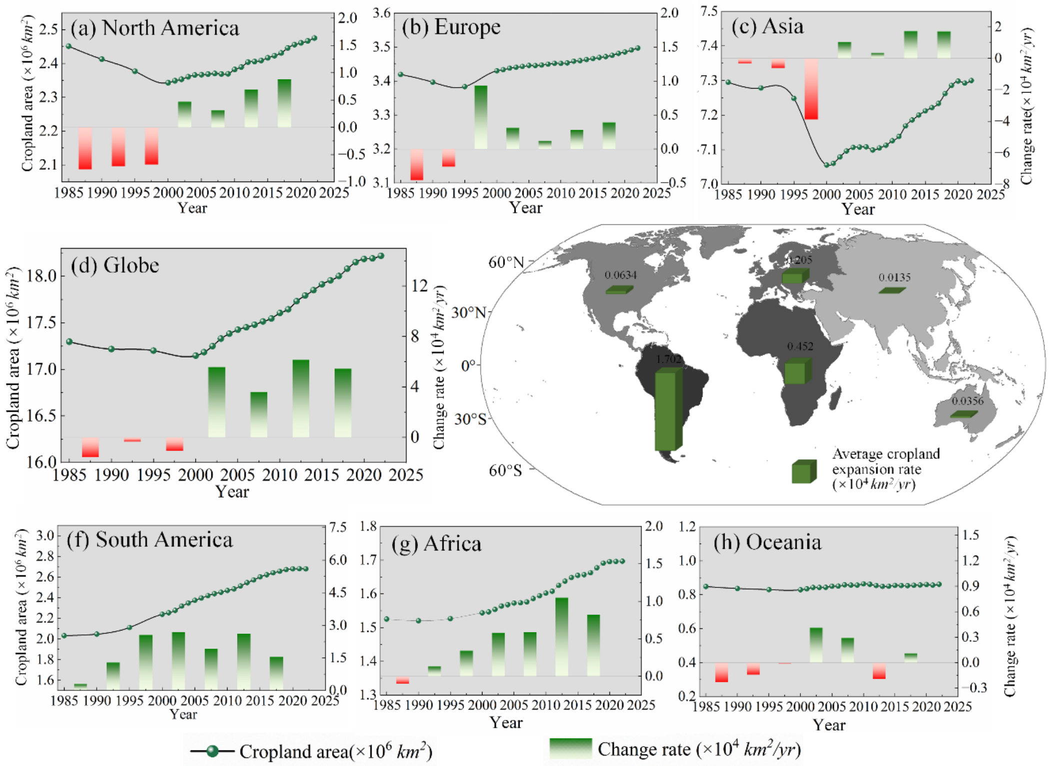

6-2: Global cropland area dynamics and analysis

Global per capita cropland area decreased by 37.5%, from 0.347 ha in 1985 to 0.217 ha in 2022. On an intercontinental scale, there was a declining trend in per capita cropland area across all continents from 1985 to 2022. In particular, **Oceania experienced the largest decline in per capita cropland area**, with a decrease of 1.372 ha, followed by **North America with a decline 0.252 ha**. **Europe experienced the smallest decline in per capita cropland area with a decline of 0.014 ha**.

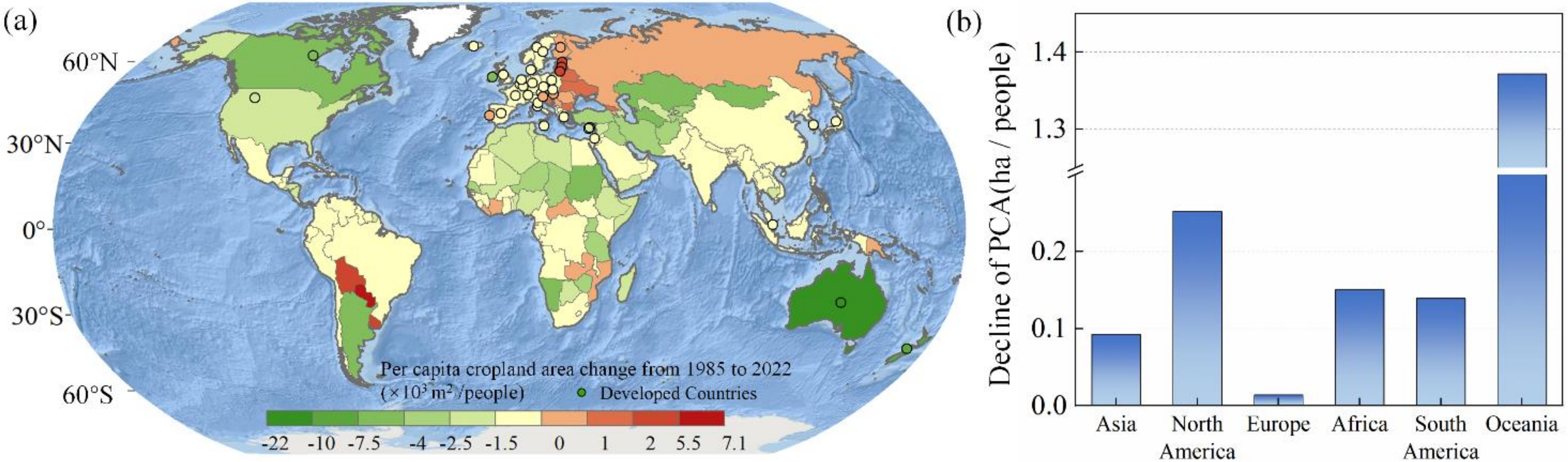

6-3: The drivers of global forest changes

Using multisourced remote sensing products to clarify the specific drivers (**anthropogenic and natural factors**) of global forest loss. The results showed:

- **Anthropogenic drivers** have dominated global forest loss over the past two decades, accounting for about 80%, primarily due to agricultural encroachment (38.0%) and forestry activity (18.2%);
- **Natural drivers** such as persistent drought (8.6%) and wildfires (5.4%) also led to nonnegligible forest loss;
- **All drivers have been accelerating forest loss**, and the increasing trend has yet to be mitigated.

Decision tree model for identifying the drivers of global forest loss

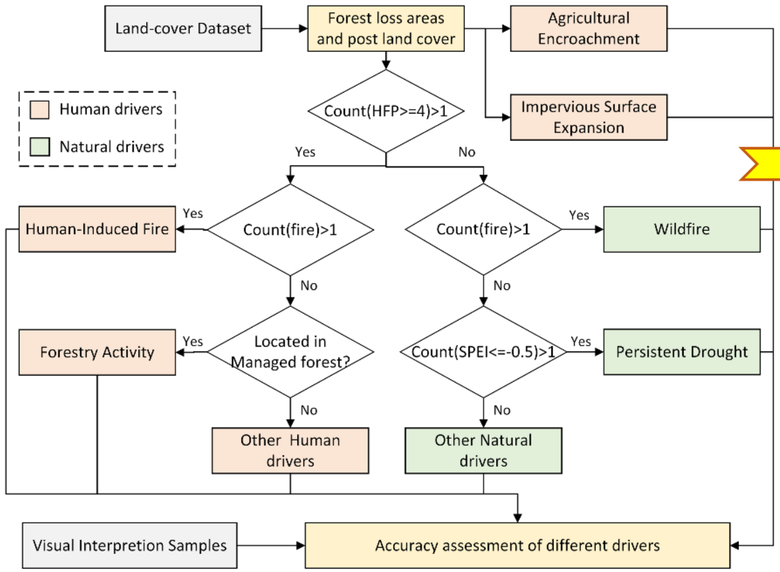

Spatial distribution of the forest loss drivers over 2000–2020

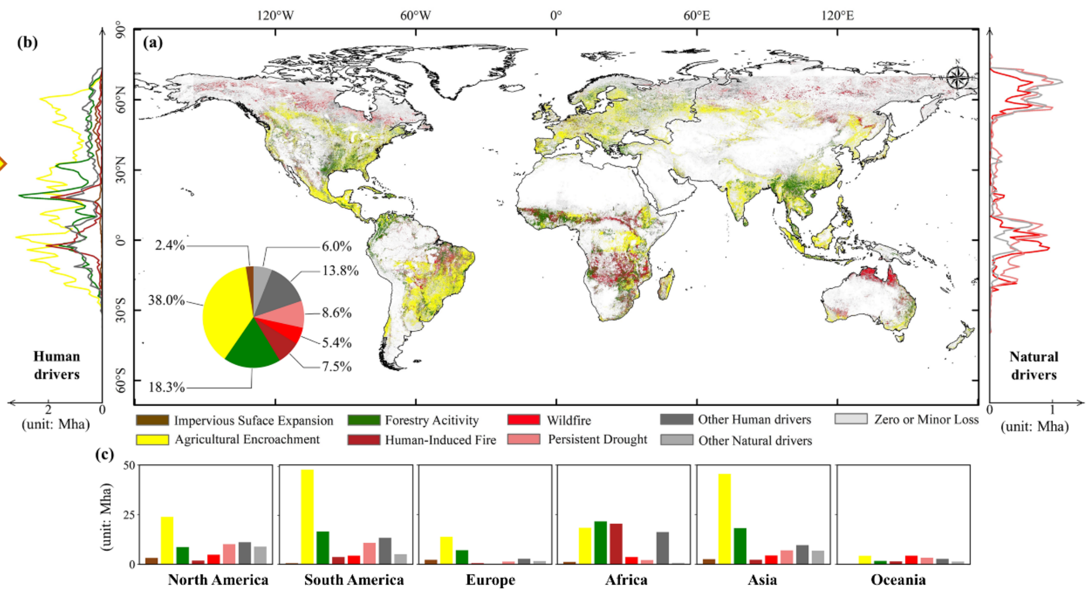

6-4: The land-cover dynamics in typical island countries

The land-cover dynamics in two typical island countries (**Papua New Guinea** and **Suriname**). Overall, the land-covers in these areas **exhibit good stability**, and **the forests are well protected**; detailedly, the **urban expansion** and **coastal changes** (mangrove forests and tidal flats) also can be clearly captured.

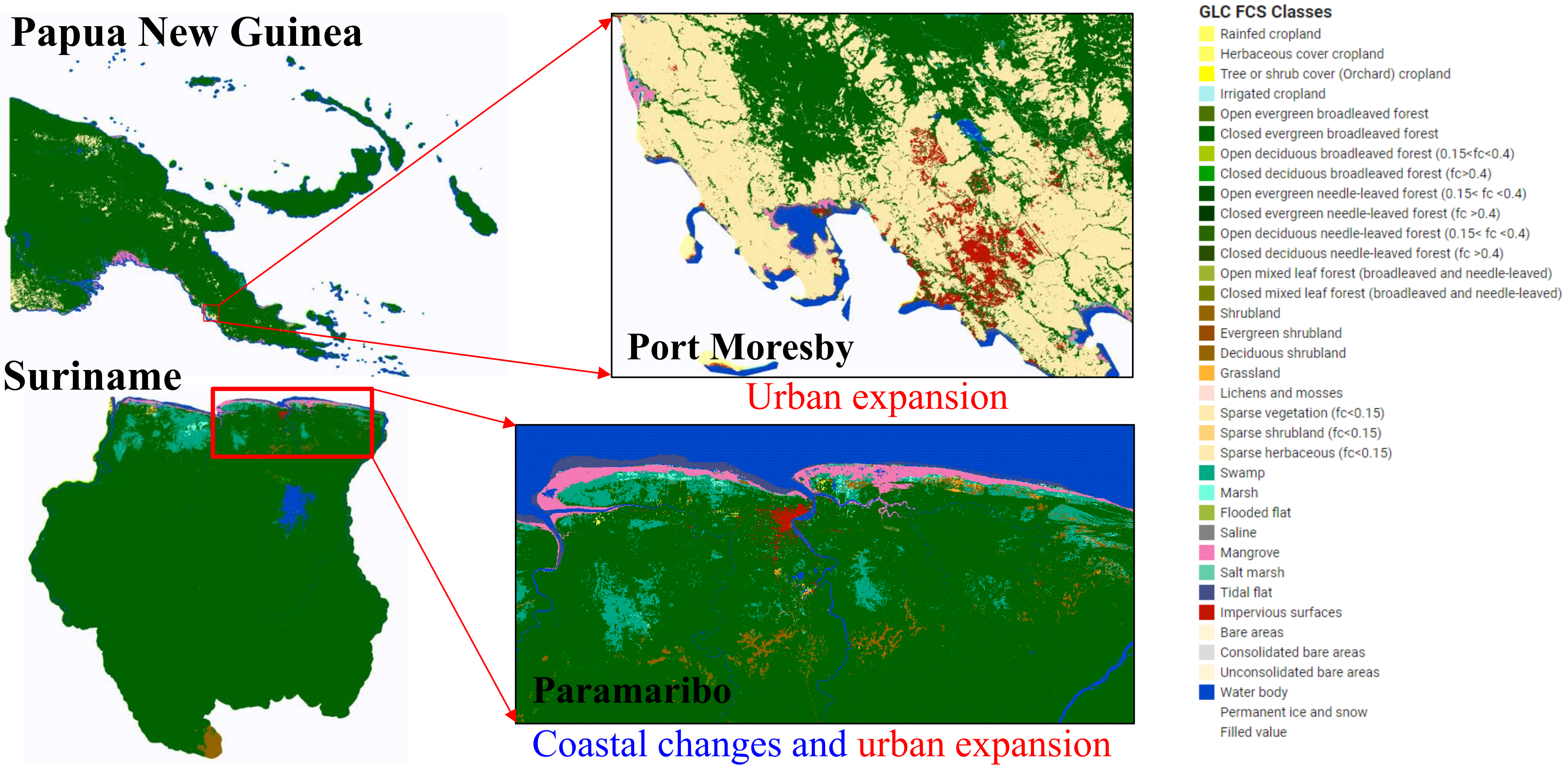

There is a long way to go, but the dawn is ahead

The world's first land-cover change dynamic update product, GLC_FCS30D (1985-2022), has been shared with **over 2 million people**. The dataset has been downloaded **more than 40 million times**, totaling a **download volume of 10 petabytes**, and has had a **widespread impact**.

The only set of long-term GLC products included in GEE has been specially produced with animated videos to demonstrate classification performance.

The dataset ranks first at the Earth Big Data sharing platform and is the most popular data product, with more than 1 million downloads.

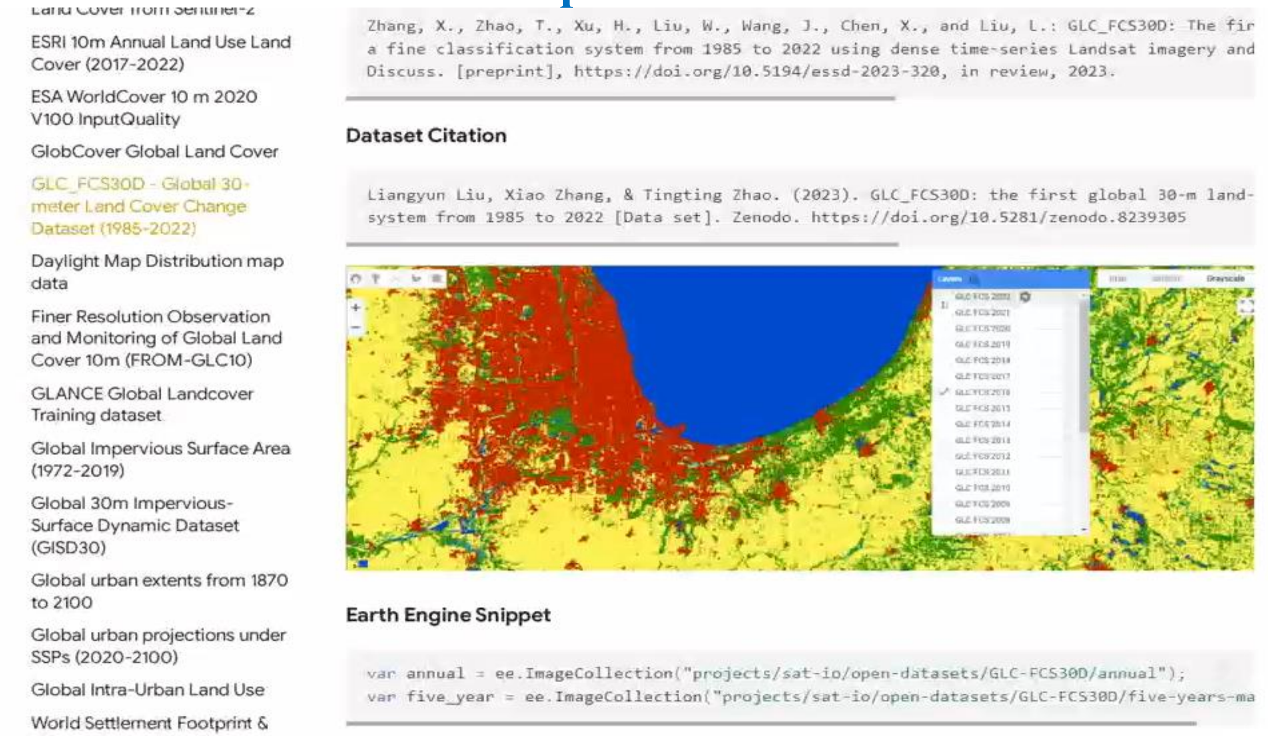

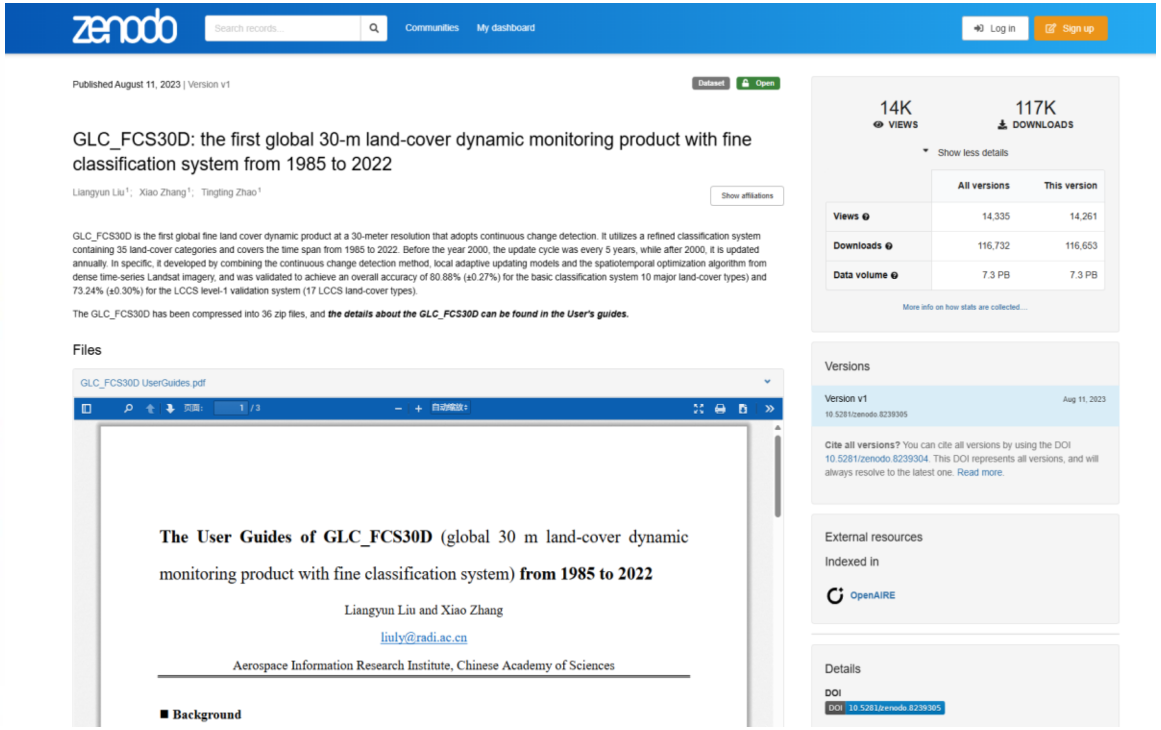

Domestic and Foreign Platforms: The United Nations Species Diversity Database, UN-Habitat's EO Toolkit database, Earth Big Data Scientific Data Sharing Platform, OpenLandMap and Google Earth Engine Community.

Thanks!

     

Aerospace Information Research Institute, Chinese Academy of Sciences

Address： No.9 Dengzhuang South Road, Haidian District, Beijing 100094, China

Tel： 86-10-82178163 Fax： 86-10-82178009

Email： liuly@radi.ac.cn Website： www.aircas.cn

https://data.casearth.cn/thematic/glc_fcs30 https://zenodo.org/records/8239305